Simulating structure formation with N-Body and semi-analytic models

Jie Wang

München Juli 2008

Simulating structure formation with N-Body and semi-analytic models

Jie Wang

Dissertation der Fakultät für Physik
der
Ludwig–Maximilians–Universität München

vorgelegt von Jie Wang
aus Hunan, China

München, den 29 Juli 2008

Erstgutachter: Prof. Dr. Simon D. M. White
Zweitgutachter: Prof. Dr. Gehard Börner
Tag der mündlichen Prüfung: 29 Juli 2008

Contents

Zusammenfassung

In dieser Arbeit untersuche ich die Strukturentstehung gemäß dem aktuellen kosmologischen Standardmodell, wobei zwei unterschiedliche numerischen Methoden verwendet werden: N-body Simulationen und Semi-analytische Galaxienentwicklungsmodelle.

In den Kapiteln 1 & 2 werden Motivation und Zielsetzung dieser Arbeit vorgestellt. Zusätzlich findet sich hier eine kurze allgemeine Einführung zu dem Thema.

Das 3. Kapitel befasst sich mit einem wohl bekannten Problem: Bei *Hot/Warm Dark Matter* (H/WDM) N-body Simulationen, deren anfängliche Teilchenverteilung auf einem regelmäßigen kubischen Gitter angeordnet ist, können artifizielle Strukturen entstehen, die alleine auf die Periodizität der Anfangsbedingungen zurückzuführen sind. Insbesondere kann es geschehen, dass Filamente, typische Erscheinungsformen derartiger Simulationen, in regelmäßige Einheiten auseinanderbrechen, welche die periodische Gitterstruktur widerspiegeln. Unter Verwendung von numerischen Simulationen kann hier nachgewiesen werden, dass ähnliche Effekte sogar dann auftreten, wenn glass-artige Anfangsverteilungen benutzt werden, obwohl Glass-Verteilungen weder bevorzugte Richtunge noch langreichweitige Kohärenzen aufweisen. Eine derartige reguläre Fragmentierung wird auch bei dem Kollaps gleichförmiger Filamente in idealisierten Simulationen beobachtet. Der idealisierte Kollaps zu einer zweidimensionalen Fläche weist jedoch keine artifizielle Fragmentierung auf. Damit muss das Auftreten aller selbst-gebundenen Strukturen in H/WDM Simulationen, welche die *free streaming* Masse substantiell unterschreiten, auf unphysikalische (rein numerische) Fragmentierung der Filamente zurückgeführt werden. Die artifiziellen Fragmente finden sich unterhalb einer charakteristischen Masse, welche durch die folgende Relation festgelegt ist: $M_p^{1/3} k_{peak}^{-2}$. Als unvermeidliche Konsequenz der artifiziellen Fragmentierung nimmt die effektive Massenauflösung in H/WDM N-body Simulationen nur mit der Quadratwurzel der Teilchenzahl zu.

Im 4. Kapitel werden N-body Simulationen mit der analytischen Modellierung von Galaxien kombiniert. Mit dieser Herangehensweise kann der Einfluss verschiedener kosmologischer Parameter auf die Galaxienpopulationen abgeschätzt werden. Von besonderem Interesse hier sind die Parametersätze, die sich aus der 1 und 3-jährigen *Wilkinson Microwave Anisotropy Probe* ableiten ließen (WMAP1 und WMAP3). In einer WMAP3 Kosmologie ist die Strukturentstehung wesentlich verzögert, da für die relevanten Skalen die Amplitude der Dichteschwankungen viel geringer ist. Die geringere Zusammenballungstendenz der dunklen Materie wird allerdings beinahe vollständig durch das anwachsen des

halo bias ausgeglichen. In beiden Kosmologien (WMAP1 & Wmap3) können verschiedene Kombinationen der Modellparameter für die Galaxienenrwicklung eine Übereinstimmung mit den, bei geringen Rotverschiebungen beobachteten, Galaxienpopulationen hervorbringen. So können verschiedene Einstellungen von Sternentstehungsrate, Supernova-Feedback und AGN-Feedback zu sehr ähnlichen Modellpopulationen führen. Die projizierten Zweipunktkorrelationsfunktionen von Modellen, die die beobachteten Leuchtkraftfunktionen reproduzieren, streuen in der Regel zwischen 10 und 20 Prozent auf großen und noch mehr auf kleinen Skalen. Diese Streuung wird sowohl von den unterschiedlichen Kosmologien, wie auch von den Details der Galaxienentstehung hervorgerufen. Messungen der paarweisen Geschwindigkeitsverteilung scheinen eine WMAP1 Kosmologie zu bevorzugen. Bei der Interpretation der Daten müssen jedoch die systematischen Fehlerquellen genau berücksichtigt werden. Modell-intrinsische Ungenauigkeiten erlauben es derzeit nicht endgültig zwischen den WMAP1 und WMAP3 Kosmologien zu unterscheiden, insbesondere da die Modellvorhersagen für geringe Rotverschiebungen, wo eine hinreichende Menge von Beobachtungsdaten vorhanden ist, nicht sonderlich stark voneinander abweichen. Bei hohen Rotverschiebungen, $z > 2$, divergieren die Modellvorhersagen beträchtlich, jedoch existiert für eine Festlegung der Modellparameter derzeit noch nicht ausreichend Beobachtungsmaterial.

In Kapitel 5 wird die Universalität von Haloeigenschaften im Rahmen des monolithischen Strukturbildungszenarios untersucht. In den letzten Jahrzehnten wurden meist *Cold Drak Matter* (CDM) Simulationen herangezogen, um das Verständnis der kosmische Strukturentwicklung zu vertiefen. Dabei kam zum Vorschein, dass Haloeigenschaften, wie Dichteprofile, Formparameter, Spinparameter und spezifische Drehimpulse 'allgemeinen' Gesetzmäßigkeiten gehorchen. Hier werde ich zeigen, dass diese Gesetzmäßigkeiten auch in *Warm Dark Matter* (WDM) Simulationen gefunden werden können, also in Szenarien, wo Halos eher durch stetige Akkretion als durch virulente Verschmelzungsprozesse gebildet werden. Die Dichteprofile von WDM Halos werden, wie auch die ihrer CDM Pendants, sehr gut durch das Navarro et al. (1997) Profil beschrieben. Meinen Ergebnissen zufolge zeigen WDM und CDM Halos zwar unterschiedliche Abhängigkeiten zwischen Konzentration und Masse, aber die Relation zwischen Konzentration und Entstehungszeit stimmt in beiden Kosmologien qualitativ überein: Halos, welche früher entstanden sind, haben eine konzentriertere Masseverteilung als ihre jüngeren Pendants. Die Entstehungsgeschichte von Halos ist nicht wesentlich anders als jene, welche schon von den CDM Simulationen her bekannt ist: einer frühen Phase der schnellen Massenakkretion, begleitet von seltenen Verschmelzungen von Protohalos vergleichbarer Massen, folgt eine Phase der stillen oder kontinuierlichen Akkretion. Für weitere Verteilungen, wie die der Formparameter, der Spinparameter und der spezifischen Drehimpulse findet sich kein maßgeblicher Unterschied zu den entsprechenden Verteilungen von CDM Halos. Diesen Ergebnissen zufolge spielen Verschmelzungsprozesse nur eine untergeordnete Rolle in der Erzeugung oben genannter Haloeigenschaften und stellen somit eine Herausforderung für Modelle dar, welche diese Eigenschaften alleine auf Verschmelzungsprozesse zurückführen wollen.

Summary

In this thesis, I study the formation of structure within the current standard cosmological model using two numerical methods: N-body simulations and semi-analytic models of galaxy formation.

In Chapter 1 & 2, I will explain the motivations and objectives of the analysis presented in this thesis, and give a brief review of the relevant background.

Chapter 3 is focused on the discreteness effects in N-body simulation: Hot/Warm Dark Matter (H/WDM) N-body simulations in which the initial uniform particle load is a cubic lattice, exhibit artefacts related to this lattice. In particular, the filaments which form in these simulations break up into regularly spaced clumps which reflect the initial grid pattern. Using numerical simulations, I demonstrate that a similar artefact is present even when the initial uniform particle load is not a lattice, but rather a glass with no preferred directions and no long-range coherence. My study shows that such regular fragmentation occurs also in simulations of the collapse of idealized, uniform filaments, but not in simulations of the collapse of infinite uniform sheets. In H/WDM simulations, all self-bound non-linear structures with masses much smaller than the free streaming mass appear to originate through spurious fragmentation of filaments. These artificial fragments form below a characteristic mass which scales as $M_p^{1/3} k_{peak}^{-2}$. This has the unfortunate consequence that the effective mass resolution of such simulations improves only as the cube root of the number of particles employed.

In Chapter 4, I combine N-body simulations of structure growth with physical modelling of galaxy evolution to investigate whether the shift in cosmological parameters between the 1-year and 3-year results from the Wilkinson Microwave Anisotropy Probe (WMAP) affects predictions for the galaxy population. Structure formation is significantly delayed in the WMAP3 cosmology, because the initial matter fluctuation amplitude is lower on the relevant scales. The decrease in dark matter clustering strength is, however, almost entirely offset by an increase in halo bias, so predictions for galaxy clustering are barely altered. In both cosmologies, several combinations of physical parameters can reproduce observed, low-redshift galaxy properties; the star formation, supernova feedback, and AGN feedback efficiencies can be played off against each other to give similar results for a variety of combinations. Models which fit observed luminosity functions predict projected 2-point correlation functions which scatter by about 10-20 per cent on large scale and by larger factors on small scale, depending both on cosmology and on details of galaxy formation.

Measurements of the pairwise velocity distribution prefer the WMAP1 cosmology, but careful treatment of the systematics is needed. Given current modelling uncertainties, it is not easy to distinguish the WMAP1 and WMAP3 cosmologies on the basis of low-redshift galaxy properties. Model predictions diverge more dramatically at high redshift. Better observational data at $z > 2$ will better constrain galaxy formation and perhaps also cosmological parameters.

In Chapter 5, I study whether the apparent universality of halo properties in hierarchical clustering cosmologies is a consequence of their growth through mergers.

N-body simulations of Cold Dark Matter (CDM) have shown that, in this hierarchical structure formation model, dark matter halo properties, such as the density profile, the phase-space density profile, the distribution of axial ratio, the distribution of spin parameter, and the distribution of internal specific angular momentum follow 'universal' laws or distributions. Here I study the properties of the first generation of haloes in a Hot Dark Matter (HDM) dominated universe, as an example of halo formation through monolithic collapse. I find all these universalities to be present in this case also. Halo density profiles are very well fit by the Navarro et al (1997) profile over two orders of magnitude in mass. The concentration parameter depends on mass as $c \propto M^{0.2}$, reversing the dependence found in a hierarchical CDM universe. However, the concentration-formation time relation is similar in the two cases: earlier forming haloes tend to be more concentrated than their later forming counterparts. Halo formation histories are also characterized by two phases in the HDM case: an early phase of rapid accretion followed by slower growth. Furthermore, there is no significant difference between the HDM and CDM cases concerning the statistics of other halo properties: the phase-space density profile; the velocity anisotropy profile; the distribution of shape parameters; the distribution of spin parameter, and the distribution of internal specific angular momentum are all similar in the two cases. Only substructure content differs dramatically. These results indicate that mergers do not play a pivotal role in establishing the universalities, thus contradicting models which explain them as consequences of mergers.

Chapter 1

Thesis objectives and framework

Abstract

In this chapter I explain the motivations and objectives of this thesis, and provide an outline of the following chapters.

Over the past decades, a number of observational tests have converged to establish the cold dark matter model with its concordance set of parameters (ΛCDM) as the standard model for structure formation. In our Universe, the total energy density is close to the critical density needed for closure, implying that the geometry of the observed Universe is flat. The two dominant components are of non-baryonic nature: cold dark matter and an unknown form of dark energy. The former is responsible for building up the potential field and inducing perturbations of the baryonic matter to grow into luminous objects; the latter is currently dominating the evolution of the Universe and causing its expansion to accelerate. The mean density of baryonic matter is only approximately 4.5% of the total energy density, and accounts for all visible objects in the Universe. This model is incredibly successful in reproducing a large number of observations in particular on large scales and at various cosmic epochs.

Given the well constrained cosmological model, the focus is beginning to shift away from determining the values of the cosmological parameters towards solving the problems of structure formation at small scales. In the standard ΛCDM model, the formation of dark matter haloes has been well studied by means of direct numerical simulation of collisionless particle systems. A number of properties of dark matter haloes are found to be "universal". For example, the density profile, the phase space density profile, the shape parameter distribution, the spin distribution, and the distribution of internal specific angular momentum. However, the origin of these universalities is not well understood. At sub-galactic scale, the success of the ΛCDM model has not been convincingly demonstrated yet, and a number of issues remain the subject of a lively debate (e.g. the inner density profile, the satellite abundance, the angular momentum problem in disk formation).

Understanding the formation and evolution of luminous objects is much more difficult because of the more complicated and strongly interacting physical processes that are at play. Given the large uncertainties involved, modern models of galaxy formation and evolution are based on a number of assumptions that are sometimes difficult to verify.

However, with the detection of sizable populations of galaxies both in the local Universe and at high redshift, with the increase in available computing power and the development of powerful new techniques, we now have the ability to sample the parameter space of different models, to study structure formation with higher resolution, and advance in this way in our understanding of how cosmic structures formed and evolve.

N-body simulations and semi-analytic (SA) models of galaxy formation represent very useful tools to address these issues. N-body simulations enable us to follow the formation and evolution of dark matter haloes in their full geometrical complexity. Modern SA models take advantage of high resolution N-body simulations to specify the location and assembly histories of galaxies and invoke simple yet physically and observationally motivated prescriptions to model the evolution of the baryonic component.

In this thesis, I will use both tools to address a number of questions related to structure formation. In the following, I will give an outline of the projects that were carried out.

Numerical issues on simulating H/WDM Universe Although the CDM model has become the 'standard' model of structure formation, and measurements of large-scale structure have ruled out the neutrino as a candidate for 'hot' dark matter (White et al. 1983), H/WDM models or some mixed models are not ruled out completely. In particular particle physicists still consider a kind of warm dark matter – the massive sterile neutrino mixed with an ordinary neutrino – as the most popular candidate for the dark matter. Therefore, simulating the H/WDM dominated Universes is necessary to help in distinguishing different dark matter models. Because of free-streaming effects, there is a cutoff at small scales in the power spectrum of H/WDM models. Due to this lack of small-scale power , discreteness effect in N-body systems can dominate structure growth at small scales in H/WDM universes. For example, spurious substructures form in filaments with a regular pattern. Such numerical effects were noticed for the first time more than 20 years ago. In Chapter 3, I study these effects and find a simple fitting expression to describe the characteristic mass scale under which all self-bound non-linear structures appear to originate through spurious fragmentation of filaments caused by discreteness effects.

Galaxy formation and Cosmology model Large scale surveys have confirmed the CDM model as the standard model for structure formation. In recent years, the semi-analytic scheme has developed into one of the most powerful approaches to model galaxy formation and evolution within this standard paradigm. Semi-analytic models have enjoyed many successes and now eventually allow the cosmological parameters to be constrained by comparing simulated galaxy catalogues with real data.

The first-year and third year data from the Wilkinson Microwave Anisotropy Probe (WMAP) did much to reinforce the ΛCDM model as the "standard" model for structure formation, but they also had some significant differences in their conclusions about cosmological parameters. In particular there is a 20 per cent difference in the best-fit normalization parameter of the power spectrum σ_8, which implies a significant shift in galaxy formation time, as well as the significant differences in the abundance and clustering of galaxies. In Chapter 4, I combine N-body simulation and semi-analytic galaxy formation models to investigate whether the shift between the 1-year and 3-year WMAP parame-

ters affects predictions for the galaxy population. Furthermore, by comparing with the real data, I can investigate if simulated galaxy catalogues can provide any constrains on cosmological parameters.

Halo formation history and its internal structure N-body simulations of CDM have been widely used and analyzed in the last decades. It has been shown that in the framework of this structure formation paradigm, halo properties such as the density profile, the shape parameter distribution, the spin distribution, and the distribution of halo internal specific angular momentum follow 'universal' laws or distributions. The origins of these 'universal' distributions are not well understood yet. Most proposed explanations have been based on the hypothesis that mergers are the main driving force to build up these regularities. I test whether this is the case by using controlled simulations in which halo formation occurs, at least initially, through a monolithic collapse. Starting from a good understanding of the numerical effects studied in Chapter 3, I carry out N-body simulations of HDM dominated universe as an example of cosmological model in which the first haloes grow by monolithic collapse. I study whether universal halos properties extend also to such haloes. Results of this study are discussed in Chapter 5.

Finally, I will summarize the most important findings of the work carried out for this thesis, and give my conclusions. Meanwhile, I will point out some future perspectives.

Chapter 2

Introduction

Abstract
In this chapter, I review the background relevant for this thesis. A large number of observational tests have recently converged to establish the ΛCDM model as the "standard" model for structure formation. I briefly summarize the backgroud cosmology and some related issues of structure formation with this thesis in the standard cosmological model. Then I give an overview of the primary tools used in this thesis: N-body simulations and semi-analytic galaxy formation models.

2.1 Background cosmology

2.1.1 The Friedmann models

The current standard cosmological model (ΛCDM) model is based on the "cosmological principle", and is described by the highly symmetric Robertson-Walker metric. The cosmological principle states that, on sufficiently large scales, the Universe is homogeneous and isotropic. Homogeneity is the property of being identical everywhere in space, while isotropy is the property of looking the same in every direction.

The dominant force of nature on large scales is gravity, so the most important part of a physical description of the Universe is a theory of gravity. Einstein's General Theory of Relativity is the best candidate for such a theory currently. This theory considers the gravitation as a property of the space-time whose evolution can be described by the following equations:

$$G_{ik} = R_{ik} - 1/2 g_{ik} R - \Lambda g_{ik} = \frac{8\pi G}{c^4} T_{ik} \tag{2.1}$$

Where the Einstein tensor G_{ik} describes the space-time geometry and the energy-momentum tensor T_{ik} describes the matter/energy distribution.

General relativity is a geometrical theory, and the most general space-time metric describing a homogeneous and isotropic space is the Robertson-Walker metric:

$$ds^2 = (cdt)^2 - a(t)^2 [\frac{dr^2}{1 - Kr^2} + r^2 (d\theta^2 + \sin^2 \theta d\phi^2)] \tag{2.2}$$

where we have used spherical polar coordinates: r, θ and ϕ are comoving coordinates; t is the proper time, and $a(t)$ is a function to be determined which has the dimensions of a length and is called the expansion parameter. A relative quantity named *redshift* is defined as $z = (f_{\rm emitted} - f_{\rm observed}) = 1/a - 1$. The energy of photons emitted by distant sources (frequency $f_{\rm emitter}$) is reduced by the expansion of the Universe and has a lower observed frequency $f_{\rm observed}$. The redshift is often used as a time variable in cosmology. The curvature parameter k is a constant which can be scaled in such a way that it takes only the values 1, 0 or -1 which correspond to a closed, flat or open geometry respectively.

The Einstein equations of general relativity relate the geometrical properties of space-time with the energy-momentum tensor describing the matter content of the Universe. In particular, for a homogeneous and isotropic perfect fluid with rest-mass energy density ρc^2 and pressure p, the Einstein equations can be rewritten in the following form (Friedmann equations):

$$\ddot{a} = -\frac{4\pi G a}{3}(\rho + 3p/c^2) + \frac{1}{3}\Lambda c^2 a \tag{2.3}$$

$$\dot{a}^2 = \frac{8\pi G\rho}{3}a^2 - kc^2 + \frac{1}{3}\Lambda a^2 \tag{2.4}$$

where Λ is the well-known *Cosmological constant* and may be thought of as a repulsive force. Defining a Hubble constant $H = \dot{a}/a$, and a critical density $\rho_{crit} = \frac{3H^2}{8\pi G}$, equation 2.4 can be written as:

$$H^2(t) = H_0^2[\frac{\Omega_r}{a^4(t)} + \frac{\Omega_m}{a^3(t)} - \frac{\Omega_k}{a^2(t)} + \Omega_\Lambda] \tag{2.5}$$

Where $\Omega_r = \frac{3p}{\rho_{crit}c^2}$, $\Omega_m = \frac{\rho_m}{\rho_{crit}}$, $\Omega_k = \frac{Kc^2}{H_0^2}$, and $\Omega_\Lambda = \frac{\Lambda}{3H_0^2}$ are the energy density parameters of a multi-component fluid (radiation: $3p/c^2$; matter: ρ_m; curvature: K, and the cosmological constant: Λ).

Given an equation of state, for example, $3p/c^2 = 0$ for a dust-filled Universe, one can study the dynamics of the whole Universe using the Friedmann equations.

2.1.2 Primordial density field and Transfer function

Currently, the most bound objects in the Universe are thought to grow from tiny initial density fluctuations due to the gravitational collapse. The inflation theory predicts that the initial perturbation spectrum can be represented by a power law: $< \delta_k^2 >= k^n$ and $n = 1$. δ_k is the Fourier transform of the density perturbation $\delta = \frac{\rho - \bar{\rho}}{\bar{\rho}}$ and ρ, $\bar{\rho}$ are the density field at a given location and its average value. The case $n = 1$ corresponds to the case that the perturbation of potential filed will be independent of scale. This corresponds to the Harrison-Zel'dovich *constant curvature* scaling: all fluctuations have approximately the same escape velocity, and the density contrast have the same amplitude on all scales when the perturbations come through the horizon.

Besides the shape of the power spectrum, the normalisation is another important parameter that influences the following structure formation. There are three methods which can be used to normalise the power spectrum at different scales:

1: At large scales, the normalization can be done using the Cosmic Microwave Background (CMB) anisotropies. In a specific cosmology, the CMB temperature fluctuations can be related to matter density perturbations, yielding a characteristic shape of the matter density power spectrum. This method has been used for the COBE (COsmic Background Explorer) and the WMAP (Wilkinson Microwave Anisotropy Probe) satellites (Banday et al. 1997; Spergel et al. 2003, 2007).

2: At intermediate scales of about $\sim$ 10Mpc/h, the power spectrum can be normalized using the local abundance of galaxy clusters (White et al. 1993). The spatial number density of clusters can be used to measure the amplitude of dark matter fluctuations since galaxy clusters are expected to form by gravitational instability from dark matter density perturbations. Requiring the power spectrum to reproduce the observed local number density of clusters, one determines its normalization.

3. Finally, the power spectrum can be normalized by the local variance of galaxy counts (Davis & Peebles 1983). The variance of galaxy numbers at some special scales (normally $\sim$ 8Mpc/h) σ_8 relates to the dark matter fluctuations, and can be used to determine the amplitude of the power spectrum. But in this method, the bias between the galaxies and the underlying dark matter perturbations needs to be assumed *a priori*.

With the combination of redshift galaxy surveys, the first-year CMB observations from the WMAP satellite did much to establish ΛCDM cosmological model. Two further years of WMAP data have significantly refined this model, leading to noticeable shifts in some parameters, especially the amplitude of power spectrum (σ_8) which is decreased by 20 percent. In Chapter 4, I will study the impact of the changes of σ_8 and other parameters between WMAP1 and WMAP3 on predictions from galaxy formation models.

The primordial power spectrum is believed to be modified, during the evolution of the Universe until the end of recombination, by various processes including growth under self-gravitation, the effects of pressure and dissipative processes. The function describing the changes to the input spectrum of primordial perturbations is called the transfer function $T(k)$:

$$T(k) = \frac{\delta_k(z_0)}{\delta_k(z)D(z)} \tag{2.6}$$

which gives the ratio of the later time (z) amplitude of a mode ($\delta_k(z)$) to its value at initial time z_0 ($\delta_k(z_0)$). Here $D(z)$ is the linear growth factor and will be discussed later. The shape of transfer function is affected by the types of dark matter and types of fluctuation modes.

In the case of the Cold Dark Matter(CDM) model, prior to the epoch of equality of matter and radiation energy densities, the mass spectrum preserves its initial form $\Delta = \delta\rho/\rho \propto M^{-(n+3)/6}$ and the perturbations grow as a^2 till they enter their particle horizons. After they enter the horizon, they couple into the dominate mass and oscillate as sound waves before the radiation-dominated era ends. Normally, the scale factor at which a perturbation of mass M enters the horizon is proportional to $M^{1/3}$, and the density perturbation spectrum for a mass less than the horizon mass become $\Delta \propto M^{-(n+3)/6} \times M^{2/3} = M^{-(n-1)/6}$. Therefore, the resulting power spectrum is flatter than the input power spectrum on small mass scales. Analytic expressions for the transfer function in this case are given by Peebles (1982) and Davis et al. (1985).

For the isocurvature perturbation modes, after they enter the particle horizon, they evolve like the cold dark matter described above, but are subject to the additional Meszaros effect. As a result, the amplitude of modes is lower than that of adiabatic modes at smaller mass scales. Efstathiou & Bond (1986) have presented analytic expresions for the transfer function in this case.

If the dominant matter in the Universe is Hot or Warm dark matter, the small-mass scale perturbations are subject to free-streaming damping due to the higher decoupling velocity of the dark matter particles as soon as the perturbations come through the horizon, during the radiation-dominated era. Therefore, there is an exponential cut off at the small mass scales in the power spectrum. The analytic expression for this distortion is given by Bond & Szalay (1983) and Kolb & Turner (1990).

The interaction between baryonic matter and radiation during the plasma epoch and the consequent dissipation due to viscosity and thermal conduction are also important physical phenomena and will leave their impact on the matter power spectrum. One effect of these dissipative processes on an adiabatic perturbation is to decrease its amplitude. Another important feature is the strong oscillations in the baryon version of the transfer function. Waves with different modes have different temporal phases which result in the waves arriving at recombination at different stages of their cycle. At recombination, the restoring force for the oscillations supplied by pressure disappears and the waves become stranded with an amplitude that depends on wavelength. Since dark matter are collisionless, there is no restoring force, and the acoustic oscillations therefore do not occur in the pure dark matter power spectrum.

Accurate calculation of the transfer function requires a solution of the Boltzmann equation with a mixture of different matter and relativistic particles. Currently Many Boltzmann codes are available, for example, CMBFAST (Seljak & Zaldarriaga 1996) and CAMB (Lewis et al. 2000).

In Chapter 3 & 5, I will address two questions related to halo formation in a hot dark matter dominated Universe. The power spectrum for such a Universe is calculated from the formula given by Bond & Szalay (1983), which is found to converge with the numerical results from CMBFAST very well.

2.2 Structure formation

In the following section, I will briefly summerize some issues related to structure formation. These will provide a general introduction to the three projects discussed in the following chapters.

After the epoch of equality of matter and radiation energy densities, the amplitudes of the perturbations will grow linearly during the matter-dominated era as a linear growth factor until they become non-linear when $\Delta \sim 1$. The perturbations with the largest amplitudes attain $\Delta \sim 1$ first and begin to collapse to form bound systems. For the CDM case, the first objects to form are low mass systems that later assemble into larger scale systems in a hierarchical clustering process. In contrast, in the H/WDM case, the first objects to form are massive because smaller mass scale perturbations are smoothed out by the free-streaming effect. Galaxy-size objects then form by successive processes of

fragmentation of these large objects. In the dark-matter-only Universe, the perturbations consist of collisionless particles and dissipative processes are not relevant. Kinetic energy is lost primarily by violent relaxation (Lynden-Bell 1967) to form bound structures satisfying the virial theory. In this process, dark matter particles get rid of half of their kinetic energy and end up in an equilibrium configuration. Subsequently, energy exchange among dark matter particles can take place by dynamical friction, which is a relatively slow process.

2.2.1 Linear theory

For a collisionless fluid in a static background, since gravity is an attractive force, an overdense region is expected to accrete material from its surroundings, thus becoming even more dense. This process will result in an instability which can ultimately cause the collapse of a fluctuation to a gravitationally bound system. Jeans (1902) applied first order perturbation theory to study this instability for a collisional gas in a static background for the first time. His theory can be easily extended to the case of density perturbations in an expanding Universe. In comoving coordinates, positions $\mathbf{x}$ and peculiar velocities $\mathbf{v}$ are defined as $\mathbf{x} = \mathbf{r}/a$ and $\mathbf{v} = a\dot{\mathbf{x}} = \mathbf{u} - \dot{a}\mathbf{x}$ where $\mathbf{r}$ and $\mathbf{u}$ are physical positions and peculiar velocities of the fluid. Density and time can also be replaced by the dimensionless overdensity $\delta = \rho/\bar{\rho} - 1$ and the conformal time $d\tau = dt/a$ ($\bar{\rho}$ is the mean density). Therefore we can describe the evolution of an ideal fluid with three equations: the equation of continuity, Euler's equation and Poisson's equation:

$$\frac{d\delta}{d\tau} + \bigtriangledown \cdot [(1+\delta)\mathbf{v}] = 0; \tag{2.7}$$

$$\frac{d\mathbf{v}}{d\tau} + \frac{\dot{a}}{a}\mathbf{v} + (\mathbf{v} \cdot \bigtriangledown)\mathbf{v} = -\frac{\bigtriangledown p}{\bar{\rho}(1+\delta)} - \bigtriangledown\Phi; \tag{2.8}$$

$$\bigtriangledown^2 \Phi = 4\pi G\bar{\rho}a^2\delta. \tag{2.9}$$

where p is the pressure and Φ is the potential; $\bigtriangledown$ and $d/d\tau$ are derivative with respect to $\mathbf{x}$ and τ respectively.

From the above three equations, assuming that δ, $\mathbf{v}$ and all gradients are small, we obtain:

$$\ddot{\delta} + \frac{\dot{a}}{a}\dot{\delta} = \frac{\bigtriangledown^2 p}{\bar{\rho}(1+\delta)} + 4\pi G\bar{\rho}a^2\delta. \tag{2.10}$$

The solution of this equation is particularly simple for an Einstein-de Sitter Universe in which we have $\bar{\rho} = \rho_{crit} = \frac{8\pi G}{3H^2}$ and $a \propto t^{2/3} \propto \tau^2$. In absence of pressure, we can rewrite the above equation as:

$$\ddot{\delta} + 2\dot{\delta}/\tau - 6\delta/\tau^2 = 0. \tag{2.11}$$

The two solutions for this equation are $\delta \propto \tau^2 \propto t^{2/3} \propto a$ and $\delta \propto \tau^{-3} \propto t^{-1} \propto a^{-3/2}$. The former is the growing mode and the latter is the decaying mode. Normally, only the growing mode is relevant for most applications. When $\delta \ll 1$, the growth of the perturbation at

later time can be written as $\delta(z) = \delta(z_0) * \frac{D(z)}{D(z_0)}$ and the growth factor $D(z)$ can be taken as (Carroll et al. 1992):

$$D(z) \propto H(z) \int_z^\infty dz \frac{1+z}{H^3(z)} \approx \frac{5}{2} \frac{\Omega(z)/(1+z)}{\Omega_m(z)^{4/7} - \Omega_\Lambda(z) + (1 - \Omega_m(z)/2)(1 + \Omega_\Lambda(z)/70)} \quad (2.12)$$

The approximation on the right side of above equation is good to a few percent.

The evolution of peculiar velocities can be derived, knowing the potential gradient, from equation 2.8.

It is also interesting to analyses the growth of the perturbations of the baryonic matter. During the time from equilibrium to recombination, perturbations in the dark matter grow by a factor a_{rec}/a_{eq}. a_{rec} and a_{eq} are the time of the recombination epoch and the equilibrium epoch. At the same time, baryonic fluctuations do not experience any growth because of the tight coupling between baryons and photons. After decoupling, perturbations in the ordinary matter will also start to grow driven by the gravitational potential of the dark matter. The growth will follow $\delta_b = \delta_{DM}(1 - \frac{a_{rec}}{a})$. where δ_b and δ_{DM} are perturbations of baryon and dark matter. We can see that baryonic fluctuations quickly catch up with perturbations in the dark matter component after decoupling.

2.2.2 The Zel'dovich Approximation

As shown above, when $\delta \ll 1$, the growth of perturbations will follow a self-similar evolution: $\delta(z) = \delta(z_0) * \frac{D(z)}{D(z_0)}$. Using this relation in the Poisson equation, we find the same is true for the gravitational acceleration : $\Phi(z) = \frac{D(z)\Phi(z_0)}{aD(z_0)}$ where $\bigtriangledown^2\Phi(z_0) = 4\pi G\bar{\rho}a^3\delta(z_0)$. using these relations in the linearized form of Euler's equation and integrating this equation, we obtain (White 1996):

$$x = x_0 - \frac{D(z)}{4\pi G\bar{\rho}a^3 D(z_0)} \bigtriangledown \Phi(z_0) \quad (2.13)$$

and

$$v = -\frac{\dot{D}(z)}{4\pi G\bar{\rho}a^2 D(z_0)} \bigtriangledown \Phi(z_0). \quad (2.14)$$

These formulae are due to Zel'dovich (1970). They show that the motion of particles can be described using the Lagrangian formalism. Zel'dovich suggested that these formulae could be used to extrapolate the evolution of structure into the regime where the displacements are not small any more. This is the famous Zel'dovich approximation. Once the fluctuations evolve into the non-linear regime ($\Delta \gg 1$), the linear growth theory discussed above breaks down. As a first-order Lagrangian perturbation theory, the Zel'dovich approximation can be used to describe the development of perturbations in the non-linear regime. Rather than working out the development of perturbations in some external Eulerian reference frame, the motion of particle's in a comoving coordinate frame is followed. If the displacement map from $x_0 \rightarrow x$ is small, then, due to the mass conservation, we can get the evolution of the density $\rho(x, z)$ as:

$$\rho(x, z) = \frac{\bar{\rho}}{|J(x, z)|} \quad (2.15)$$

where $\bar{\rho}$ is the mean density in the Universe and $|J(x,z)|$ is the determinant of the Jacobian of the mapping $x_0 \rightarrow x$. The matrix J is symmetric and can therefore be locally diagonalised as:

$$1+\delta = \frac{1}{(1-\lambda_1 D)(1-\lambda_2 D)(1-\lambda_3 D)} \tag{2.16}$$

where $\lambda_1 \geq \lambda_2 \geq \lambda_3$ are the three eigenvalues of the matrix J. Zel'dovich found that the density field will collapse along the main axis of system when $\lambda_1 D = 1$. Therefore, the first nonlinear objects are thus predicted to form at local maxima of λ_1, and Zel'dovich called these objects "pancakes ".

The Zel'dovich approximation can provide us a very good description of the structure formation during the linear and weakly-nonlinear phases of the early Universe. It is commonly used to build up the initial condition for N-body simulations at some starting redshift. I will give more details on this in the section 2.3

2.2.3 The statistics of hierarchical clustering

The clustering of haloes and galaxies within different cosmology models, and at different cosmic times will be discussed in detail in Chapter 4. Some applications of the statistics of hierarchical clustering are also useful for the construction of galaxy formation models. Historically, There have been two approaches to study the spatial clustering of dark matter haloes.

One approach is given by the *'peak formalism'*: The matter which will collapse to form bound objects can be identified as the peaks of perturbations in the initial density field after smoothing with a filter of appropriate scale. Usually, these peaks are expected to form a bound object if they rise above some fixed threshold. This means that the initial growing mode in density field $\delta(\mathbf{x}, t_0)$ can determine completely the distribution of nonlinear lumps at all later times. The detailed mathematical development is set out by Bardeen et al. (1986). This scheme allows the calculation of the abundance and clustering of peaks in the field $\delta(\mathbf{x}, t; R)$ (R is the smoothing scale) as a function of their height and auxiliary properties such as their shape. The theory naturally predicts the properties of objects of a given mass forming at different times. However, with this scheme, it is difficult to predict the distribution in mass of the objects present at a given time. Bond & Myers (1996a,b,c) made considerable progress on this issue by identifying virialized cosmological objects with a point process of "peak patches" in the initial (Lagrangian) space, and then tracing the evolution of the objects forming from those 'patches'.

Another approach is based on the discussion of hierarchical clustering developed by Press & Schechter (1974) (named the *Press-Schechter Theory*). They assume that density perturbations can be considered to form virialized objects when they grow above some critical value δ_c (for example 1.686 as predicted by the top-hat collapse model). If one assumes that the primordial density perturbations follow a Gaussian distribution:

$$p(\delta) = \frac{1}{\sqrt{2}\sigma(M)} \exp[\frac{-\delta^2}{2\sigma^2(M)}] \tag{2.17}$$

where $\sigma^2(M)$ is the variance of the density perturbation $\delta = \delta\rho/\rho$ and is defined as the

mean square density fluctuation in spheres of comoving radius R:

$$\sigma^2(R,t) =< \delta(k)^2 >= \int_0^\infty d^3k|\delta^2(k)| = \frac{1}{2\pi^2}\int_0^\infty k^3 P(k)W(kR)^2\frac{dk}{k}; \tag{2.18}$$

In the above equation, $P(k)$ is the power spectrum of the density contrast and $W(kR) = 3(\sin kR - kR\cos kR)/(kR)^3$ is the Fourier-transform of a spherical top-hat window function with radius R and $R = (3M/4\pi\bar{\rho})^{1/3}$. Then, the fraction of points that exceed δ_c is given by:

$$F(\delta > \delta_c) = \frac{1}{2}[1 - \mathrm{erf}(\frac{\delta_c}{\sqrt{2}\sigma(R)})] \tag{2.19}$$

This quantity is suggested by Press & Schechter to be identified as the fraction of particles which are part of a nonlinear lump (dark halo) with mass greater than M. However, there is an obvious problem: as $M \to 0$, $F \to 0.5$. In other words, only half of the particles are part of lumps of any mass. Press & Schechter solved this, arbitrarily, by multiplying the mass function by a factor 2. Then the mass function of collapsed lumps with mass in the range $M \to M + dM$ at redshift z is :

$$n(M,z)dM = -2\frac{\bar{\rho}}{M}\frac{\partial F}{\partial R}\frac{dR}{dM}dM \tag{2.20}$$

$$= \sqrt{\frac{2}{\pi}}\frac{\bar{\rho}}{M}\frac{\delta_c}{\sigma^2}\frac{d\sigma}{dM}\exp(\frac{-\delta_c^2}{2\sigma^2})dM \tag{2.21}$$

Bond et al. (1991) developed an alternative derivation of the mass function. Instead of smoothing $\delta(\mathbf{x})$ with spherical top hat, $W(\mathbf{x}, R)$, they considered a filter which is top hat in Fourier space.

$$W(\mathbf{k}; k_c) = \begin{cases} 1 & \text{for} \quad |\mathbf{k}| < k_c \\ 0 & \text{for} \quad |\mathbf{k}| > k_c \end{cases} \tag{2.22}$$

The change in δ_s (δ in Fourier space) for the increasing from k_c to $k_c + \Delta k_c$ is a Gaussian random variable with variance

$$< \Delta\delta^2 >=< (\delta_s(\mathbf{x}; k_c + \Delta k_c) - \delta_s(\mathbf{x}; k_c))^2 >= \sigma^2(k_c + \Delta k_c) - \sigma^2(k_c) \tag{2.23}$$

where

$$\sigma^2(k_c, t) = D^2(t)\sigma_0^2(k_c). \tag{2.24}$$

Furthermore, the distribution of $\Delta\delta$ is independent of the value of δ. Therefore, we can use the random walk scheme to trace the evolution of the abundance of bound objects. This is the so called excursion set formalism. Using this approach, one can easily obtain the above Press-Schechter formula, with a natural explanation of the famous factor 2.

An excellent application of the excursion set formalism is the calculation of the mass growth history of a collapsed object by accretion and merger of smaller objects. Consider a spherical region of mass M_2 with linear overdensity $\delta_c/D(t_2)$ that forms a collapsed object at time t_2. We can write out the fraction of material in objects of mass M_2 at time t_2 which was in collapsed objects of mass M_1, at the earlier time t_1 ($t_1 < t_2$) as:

$$f(S_1, D_1|S_2, D_2)dS_1 = \frac{1}{\sqrt{2\pi}}\frac{\delta_1 - \delta_2}{(S_1 - S_2)^{3/2}}\exp(-\frac{(\delta_1 - \delta_2)^2}{2(S_1 - S_2)})dS_1. \tag{2.25}$$

Where $\delta_1 = \delta_c/D(t_1)$, $\delta_2 = \delta_c/D(t_2)$, $S_1 = \sigma^2(M_1)$ and $S_2 = \sigma(M_2)$. The mass distribution of the progenitors of objects of mass M_2 at t_2 is therefore:

$$n(M_1, t_1|M_2, t_2)dM_1 = \frac{M_2}{M_1} f(S_1, D_1|S_2, D_2)\frac{dS_1}{dM_1}dM_1. \tag{2.26}$$

Another important application of the excursion set approach is the construction of dark matter haloes merging trees. If we assume that the merging history depends only on the mass of the clump at the time it is identified and not on what happens to it subsequently, and that environment has no significant effect on the accretion of smaller lumps, then the Markov nature of the random walk process implies that the probability distribution of equation 2.25 must satisfy

$$f(S_1, D_1|S_2, D_2) = \int_{S_2}^{S_1} f(S_1, D_1|S_i, D_i) f(S_i, D_i|S_2, D_2) dS_i \tag{2.27}$$

for any $D_1 < D_i < D_2$ (corresponding to $z_1 > z_i > z_2$). Thus once a procedure has been set up which can select at random a set of progenitors for a clump of given mass, it can be repeated on the progenitors themselves to step progressively back in time, and so to build up a realization of the full merging history of the clump. A number of studies (Kauffmann & White 1993; Cole et al. 1994; Rodrigues & Thomas 1996; Somerville & Kolatt 1999; Parkinson et al. 2008) have provided efficient procedures to construct merging trees based on a Monte Carlo Method. Construction of many realizations produces an ensemble of possible histories which can be fed to semi-analytic galaxy formation models to study the evolution of the population of galaxies within dark matter clumps as a function of their mass. Cole et al. (2008) found that the EPS formalism and its Monte Carlo extension capture the qualitative behaviour of statistics extracted from N-body simulations, but as redshift increases it systematically underestimates the masses of the most massive progenitors.

A third application of the excursion set approach is the modeling of the spatial clustering of dark haloes (Mo & White 1996). As we showed above, the initial density field in the Universe is usually assumed to be Gaussian, and so to be described completely by its power spectrum. The matter power spectrum has been described in section 2.1.2. However, the clustering of galaxies will be different from that of dark matter. It is believed that the galaxies form in the highest peaks of the density distribution (Kaiser 1984; Bardeen et al. 1986). Thus if we require the density perturbation to exceed some value δ_{crit}, in order to form structure, galaxy formation would be biased towards the highest density perturbations over the mean background density. Mo & White (1996) constructed a model for the spatial clustering of dark haloes by extending the Press-Schechter theory. They found that the autocorrelation function for dark matter haloes (ξ_{hh}) of mass M is related to that of the mass (ξ_{mm}):

$$\xi_{hh}(r, M, z) = b^2(\nu, z)\xi_{mm}(r, z). \tag{2.28}$$

where the *bias factor* $b(\nu, z)$ is given by

$$b(\nu, z) = 1 + (\nu^2 - 1)/\delta_c. \tag{2.29}$$

Here δ_c is the critical linear overdensity at collapse, and it depends slightly on cosmology. $\nu = \delta_c/\sigma(M, z)$ is the dimensionless amplitude of fluctuations that produce haloes of mass M at redshift z. This formula is also presented in an earlier paper (Cole & Kaiser 1989). An updated version of the above formula considering the ellipsoidal collapse model can be found in Sheth et al. (2001). In 2005, Using modern high-resolution cosmological simulation, Gao et al. (2005) found that the bias factor also has a strong dependence on halo formation time at large scales, violating one of the fundamental assumptions of the Press-Schechter theory.

It should be noted that both approaches– 'peak formalism' and 'Press-Schechter' (or 'excursion set') – need to assume that the initial density perturbations are Gaussian.

2.3 N-body simulations

In the following two sections, I will give a brief introduction to the two main tools used in this thesis. N-body simulations and semi-analytic galaxy formation models.

The analytic methods described above provide us a physical understanding of the processes involved in structure formation, but the complexity of the physical behaviour of fluctuations in the nonlinear regime makes it impossible to study the details of this evolution using analytic methods. Furthermore, these complications prevent analytic methods from presenting detailed predictions to be tested against observations. For these reasons, one must resort to direct numerical simulations. N-body techniques represent a very useful tool to study such a system. In N-body simulations, dark matter is represented by particles sampling the phase space distribution. These particles are evolved forward in time using Newton's laws written in comoving coordinates (Peebles 1980):

$$\frac{d\mathbf{x}}{dt} = \frac{1}{a}\mathbf{v}, \tag{2.30}$$

$$\frac{d\mathbf{v}}{dt} + H\mathbf{v} = \mathbf{g}, \tag{2.31}$$

$$\bigtriangledown \cdot \mathbf{g} = -4\pi G a[\rho(\mathbf{x}, t) - \bar{\rho}(t)]. \tag{2.32}$$

Here $a(t)$ is the cosmic expansion factor, $H = d\ln a/dt$ is the Hubble parameter, $\mathbf{v}$ is the peculiar velocity, ρ is the mass density, $\bar{\rho}$ is the mean density, and $\bigtriangledown = \partial/\partial\mathbf{x}$ is the gradient in comoving coordinates. Note that the acceleration $\mathbf{g}$ is computed from the positions of all the particles. Various techniques have been developed to solve the above equations. In the following, I discuss how the boundary conditions and initial conditions are set and then discuss techniques for the force resolution and time integration.

2.3.1 Boundary and initial conditions

In cosmological simulations, such as those used in this thesis, only a patch of the whole Universe is simulated in a rectangular box (most often cubic). To avoid any artificial effect at the boundaries, and force the mean density of the simulation to remain at the desired value, periodic boundary condition on opposite faces of simulation boxes is usually

employed. One should remember that the Fourier spectrum of such a periodic Universe is discrete and only wave numbers $\mathbf{k} = \frac{2\pi}{L}(p, q, r)$ (p,q,r are integers and L is the box size) are considered. This difference between the discrete and continue Fourier representations need to be considered in some specific cases.

Setting the initial conditions for simulations of structure formation consists in specifying the background cosmological model and the perturbations imposed on the background. Normally the background model is taken to be a spatially flat or open Robertson-Walker spacetime with specified composition of dark matter, baryons, a possible cosmological constant, etc. The perturbations are assumed to follow a Gaussian distribution and the whole perturbation field can be specified completely by one function, the power spectrum $P(k)$. Once the space-time and composition are fixed, one can get $P(k)$ with analytic fitting formulae or numerical solution of the Boltzmann equation using existing codes (e.g. CMBFAST). Then, the positions and velocities of dark matter particles need to be specified for the linear density fluctuation field. The standard approach is to displace equal-mass particles from a "uniform" distribution using the Zel'dovich approximation using Fourier techniques. An alternative to set up the particle velocities is to apply linear theory either to the displacements or to the accelerations obtained by the Poisson solver.

Usually there have been used two "uniform" pre-initial conditions: Cartesian lattice and *glass*. The former is easy to implement, but it introduces a strong characteristic length scale on small scales (the grid spacing), and this strong signal is particularly noticeable in H/WDM simulations where the real small scale perturbations are suppressed by free-streaming effects. In addition, the regularity of the grid may affect the statistical properties in the low density regions. As an alternative, White (1996) suggested to use a glass-like initial particle load created by carrying out a cosmological simulation from Poisson initial conditions but with the sign of the peculiar gravitational accelerations reversed, so that each particle is repelled by all the others. When such a system reaches quasi-equilibrium, the total force on each particle vanishes, as for a grid, but the system does not have any preferred direction or long-range coherence. The power spectrum on scales much larger than the mean interparticle spacing follows a power-law $P(k) \sim k^n$ with $n = 4$ (Baugh et al. 1995), where $n = 4$ is the minimal large-scale power expected for a discrete stochastic system (Peebles 1980, section 28).

2.3.2 Force resolution

The efficiency of N-body simulations depends mainly on the algorithm used to compute the gravitational force. The desired pair force is an inverse square law representing the force between two finite-size particles, and it is softened in order to prevent the formation of unphysical tight binaries. Evaluating the forces by direct summation over all particle pairs (*Particle-Particle algorithm*) is a very time-consuming task that requires $O(N^2)$ operations for N particles. So this method can be used only for very small number of particles even with the largest parallel supercomputers or with supercomputers which are especially designed to calculate the gravity of pairs (such as GRAPE). Therefore, many different techniques have been developed to circumvent this limitation.

Particle-Mesh (PM) algorithm: The PM method uses a Fast Fourier Transform (FFT) to speed up the solving of the Poisson's equation. It is based on representing the gravitational

potential on a Cartesian grid (with a total of N_{grid} grid points). Therefore, the computational efforts is limited to the calculation of FFT and reduces to $O(N_{grid}\log(N_{grid}))$. Periodic boundary conditions are automatic, making FFT methods able to recover the potential accurately. The simplicity of this method leads to many independent implementations.

Tree algorithm: Another revolution in numerical simulation efficiency come with the use of the hierarchical tree algorithm (Appel 1985; Barnes & Hut 1986). This algorithm divides space recursively into a hierarchy of cells each containing one or more particles. If a cell of size l and distance d (from the point where force needs to be computed) satisfies $d > l/\theta$ (θ is a prescribed accuracy parameter), the particles in this cell are treated as one pseudo-particle located at the center of mass of the cell. Then the computation time reduced by replacing the set of particles by a low-order multiple expansion of the potential. Many groups have developed codes based on this algorithm. e.g. the code Gadget1 (Springel et al. 2001) and PKDGRAVE (Dikaiakos & Stadel 1996).

Particle-Particle/Particle-Mesh (P^3M) algorithm: The primary drawback of the PM method is that its force resolution is limited by the spatial FFT grid size. This limitation can be removed by supplementing the algorithm with a direct sum over pairs at small scales, resulting in the P^3M algorithm. This hybrid algorithm has also been used in many cosmological codes (e.g. Efstathiou et al. 1985; Bertschinger & Gelb 1991; Martel 1991,HYDRA).

TreePM algorithm: The P^3M method readily achieves high accuracy forces at small scales. However, when clustering becomes strong (and this occurs inevitably on small scales in realistic, high-resolution cosmological simulations), the cost of direct summation dominates and severely degrades the performance of P^3M. One solution is to replace the direct summation by a tree code. This is the TreePM method which are also used in many codes (e.g. Xu 1995; Springel 2005).

Other Gravity solvers: Various other methods have been proposed and used for computing the gravitational force. For example, adaptive P^3M algorithms are developed to overcome the large computational cost in the PP part of P^3M by using a combination of finer meshes and pair summation in the dense regions; Refinement (AMR) algorithms place hierarchical meshes where required and solve the Poisson equation on multiple grid; The adaptivity and high dynamic range of these methods make them be widely used in cosmological codes (e.g. Villumsen 1989; Kravtsov et al. 1997; Norman & Bryan 1999; Knebe et al. 2001).

In this thesis, all simulations are performed using a lean version of TreePM code Gadget2 (Springel 2005), with the SPH part excluded and with memory requirements minimized. The code was originally written in order to carry out the *Millennium Simulation* (Springel et al. 2005).

2.3.3 Time integration

The accuracy obtained when evolving N-body systems depends not only on the Poisson solver, but also on the size of the time step and on the integrator scheme used. Nowadays adaptive time-steps are commonly employed in cosmological simulations. The time-step can normally be determined by the particle's acceleration, velocity and softening (more

details can be found in Power et al. (2003)). The time integration of particle trajectories is generally performed using a second-order accurate leapfrog integration scheme requiring only one force evaluation per timestep. The KDK (kick-drift-kick) version of the leapfrog can also obtain high accuracy for individual time steps (more details can be found in Springel (2005)).

2.3.4 Properties of Dark matter halo

Using N-body simulations, we can trace the formation and evolution of dark matter haloes to non-linear phase. High resolution N-body simulations have been widely used in the past decades to study the properties of dark matter haloes. Navarro et al. (1996, 1997) found that, regardless of the detailed initial conditions, in high resolution simulations the radial mass distribution of dark haloes follows a "universal" profile:

$$\rho(r) = \frac{\rho_s}{(r/r_s)(1 + r/r_s)^2} \tag{2.33}$$

where r_s is a characteristic inner radius at which the logarithmic density slope is -2, and $\rho_s/4$ is the density at r_s. The above equation implies that $\rho \propto r^{-1}$ in the inner regions and $\rho \propto r^{-3}$ in the outskirts. High resolution simulations have also shown that the internal structure of haloes is tightly related to its growth history. All haloes experience two different growth stages: a fast-accretion phase during which the inner part of the halo is build up with a $\rho \propto r^{-1}$ profile; and a slow-accretion phase during which most of the mass in the outer parts is accumulated.

Other "universal" halo properties have also been found in hierarchical universes. The phase-space density profile has a pure power-law distribution (Taylor & Navarro 2001; Barnes et al. 2006). The shape parameter (e.g. axis ratio) distribution is regular and has a weak dependence on mass and redshift (Bullock 2002; Kasun & Evrard 2005; Allgood et al. 2006; Bett et al. 2007). The spin parameter (Peebles 1969) was found to vary weakly with halo mass, and its distribution is well described by a log-normal function (Barnes & Efstathiou 1987; Warren et al. 1992; Cole & Lacey 1996; Bullock et al. 2002; Bett et al. 2007). Bullock et al. (2001) also found that the cumulative mass distribution of specific angular momentum j is well fitted by a universal function.

In the standard CDM structure formation scenario, the structures form in a hierarchical fashion: small-scale structures are the first to collapse as virialised objects. Subsequently they merge with each other to form larger systems. The cores of haloes accreted onto larger systems survive for some time as individual entities called "substructures". The increase in resolution and development of a number of substructure finding algorithms, now allowed a study of their properties to be carried out. Numerical results indicate that the total mass in substructures is less than ten per cent of the mass of parent halo. The differential mass function of substructures follows a universal power law with index $\alpha \sim -1.8$.

In Chapter 5. I will focus on the origin of the halo's properties discussed above.

2.4 Semi-analytic galaxy formation models

Another numerical tool that will be used in this thesis (specifically in Chapter 4) is semi-analytic galaxy formation models. In subsection 2.2, I have outlined the theoretical framework for structure formation. So far, however, I have only focused on the purely gravitational aspects of structure formation. In reality, what we observe is light and the properties of luminous objects are not determined by the background gravitational potential alone. Other physical processes introduce a bias between the distribution of luminous objects and the background matter distribution. In this section, I will briefly describe several physical processes which play key roles in galaxy formation. I will then provide a simple outline of semi-analytic techniques.

2.4.1 Models of galaxy formation

In the current standard cosmological model, the dark matter is the dominant type of matter. As discussed above, the perturbations of dark matter grow up first. The perturbations of baryons will catch up those of dark matter soon after they decouple from the photon see. The evolution of the baryonic component is however much more complicated than that of the dark matter. The reason for that is that whole dark matter evolution is only governed by gravity, baryons are subject to a number of complex physical processes for which we have only a limited understanding. In the following, I briefly comment on some of these processes.

Gas cooling: Normally there are four channels to cool down the intergalactic gas:

i) Inverse Compton scattering of CMB photons by electrons. This process is only important in the very early universe (Rees & Ostriker 1977).

ii) The excitation of rotational or vibrational energy levels in molecular hydrogen through collisions. This channels is important in haloes with virial temperatures $T < 10^4 K$ (Barkana & Loeb 2001).

iii) Emission of photons during the transitions between energy levels. This process is important for haloes with $10^4 K < T < 10^6 K$.

iv) Bremsstrahlung radiation is the dominant emission mechanism in massive clusters ($T > 10^6 K$).

The later two channels are usually considered the most relevant for the galaxy formation. The cooling time of a gas is conventionally taken by dividing the thermal energy density of the gas by the cooling rate per unit volume:

$$t_{cool}(r) = (\frac{3\rho_{gas} k T_{\rm vir}}{2\mu m_{\rm H}})/(\rho_{gas}^2 \Lambda(T_{vir}, Z_{gas})) \tag{2.34}$$

Here $\mu m_{\rm H}$ is the mean particle mass, k is the Boltzmann constant, $\rho_{gas}(r)$ is the hot gas density. $\Lambda(T_{gas}, Z_{gas})$ is the cooling function which depends on both gas metallicity Z_{gas} and gas temperature T_{gas}.

The cooling rate given above can be affected by many feedback processes in either low or high mass haloes: the presence of a background of photo-ionizing radiation will suppress the cooling rate in low mass haloes (Couchman & Rees 1986; Gnedin 2000). This mechanism

works in two ways: the radiation heats the gas to a higher temperature, which increases the pressure of the baryons and reduces the following baryon gas infall and cooling. In addition, the radiation increases the ionization of the intergalactic medium, which removes some possible channels for cooling following the excitation of atoms and ions in collisions. A self-consistent model on this mechanism is presented in Benson et al. (2002). The cooling rate in massive haloes can be regulated or reduced by different mechanisms of heating of halo gas: the energy released by supernova explosions can reheat part of the cold gas up to the halo virial temperature (Bower et al. 2001; De Lucia et al. 2004); the thermal conduction transfer energy from the outer parts to the inner parts of the hot gas halo (Benson et al. 2003); the halo gas is heated by the energy released from the accretion of material onto a central black hole (Croton & et. al 2006; Bower et al. 2006).

Star formation: We do not have a complete theory of the star formation yet. Many complicated processes are involved and prevent us from predicting in a accurate way: 1) the conditions for star formation in different environments; 2) the star formation efficiency; 3) the distribution of stellar masses produced as quantified by the stellar initial mass function(IMF). For this reason, modellers have been forced to take a more pragmatic approach. If stars form in a top-down scenario where large gas cloud fragment and sub-clouds collapse to form stars, a simple estimate of the global rate of star formation can be given by:

$$\dot{M}_\star = \alpha_{\rm SF} \frac{M_{\rm cold} - M_{\rm crit}}{\tau} \tag{2.35}$$

where $M_{\rm cold}$ and τ are the cold gas mass and the dynamical time of the galaxy, defined as the ratio between the disk radius and the virial velocity, $M_{\rm crit}$ corresponds to a critical value for the gas surface density, and $\alpha_{\rm SF}$ controls the efficiency of the transformation of cold gas into stars when the gas surface density is above the critical value. This equation can be rewritten in the form of the Schmidt law which links the star formation rate per unit area of galaxy $\dot{\Sigma}_\star$ to the surface density of the cold gas Σ_{gas}: $\dot{\Sigma}_{star} \propto \Sigma_{gas}^n$ (Schmidt 1959). This power law form was later verified by Kennicutt (Kennicutt 1998) using a large sample of spiral and starburst galaxies. The exponent n was found to be ~ 1.4.

Feedback processes: Feedback is found to be necessary to modulate the star formation history. This was realized since early attempts to reproduce the observed luminosity functions (White & Rees 1978). Broadly speaking, two forms of feedback are usually considered in galaxy formation models: cold gas can be heated and removed from a galactic disc; the rate at which gas cools from the hot halo can be suppressed. Both processes diminish the reservoir of cold gas available to be turned into the stars. The second form is summarised in above item *gas cooling*.

The most common forms of feedback used in hierarchical models are reionization model, supernovae wind model and AGN model. Reionization model is used to suppress the gas cooling at high redshift. This feedback is important for the abundance of small galaxy and helps to adjust the theoretical predicted number of satellites to the observed value. Supernovae feedback is not only useful to suppress the cooling rate as discussed above, but also to eject the cold gas. The ejected material can be blown out into the hot gas halo, from which it may subsequently recool ('*retention*' model), or it may even be ejected from the

halo and left unable to cool until it is reincorporated at some later time ('*ejection*' model). The supernovae feedback is known to play key role in reproducing the flat faint end in the observed luminosity function. Many modern models assume that the the energy produced during accretion process onto existing black holes can balance the cooling radiation. This process is thought to be efficient in the massive haloes where the cooling time is longer than the Hubble time. This suppression at massive halo scale is expected to adjust the theoretical prediction to reproduce the break at the bright end of luminosity function. Different feedback models need to be played off against each other to reproduce the observed luminosity function which has a "Schechter" form.

Besides the feedback processes discussed above, some physical mechanisms are potentially playing some roles. For example, the consequences of dark matter self-annihilation for galaxy formation is considered by Natarajan et al. (2007). The combination of the thermal conduction and dynamical friction can possibly offset the radiative cooling to some extent(Naab et al. 2007).

Galaxy mergers: During hierarchical clustering dark haloes merge continuously. Thus collisions and mergers of galaxies are expected to be frequent. The accretion of satellite galaxies onto larger systems can be delayed significantly relative to the merging of the two haloes due to dynamical friction (Navarro et al. 1994). Nowadays, the haloes (and the galaxies within them) are followed even after they are accreted onto larger systems. The dynamic of a satellite subhalo can be followed explicitly by the N-body simulation until tidal stripping cause the subhalo mass to fall below the resolution limit of the simulation. When this happens, modeller assume a survival time to determine the accurate time when the galaxy is assumed to merge onto the central galaxy of its present halo. This survival time can be computed using the classical dynamical friction formulae.

Galaxy mergers provide an important channel to increase the mass and luminosity of the central galaxy. They are also assumed to have dramatic consequences on the galaxy morphology. The importance of a galaxy merge is usually related to the mass ratio of the accreted satellite galaxy to the mass of the central galaxy. In a violent or major merger (the mass ratio is close to unity), the disc of the central galaxy is assumed to be destroyed and all the stars involved in the merger event form a spheroidal remnant. An the same time, the cold gas involved in the merger event triggers a burst of star formation. In a minor merger (the mass ratio is small), the star and cold gas are normally stripped and added on to the bulge of the central galaxy.

2.4.2 Semi-analytic method

Above, I have given an overview of the formation of dark matter haloes and of the most of important physical processes in galaxy formation. We can now try to build a model for the formation and evolution of galaxies within the current standard cosmological paradigm.

The first semi-analytical models are presented in White & Frenk (1991) in which most of the ingredients of current models are presented. The first models to deal with the formation and evolution of galaxies within the evolving dark matter haloes came a few years later (Kauffmann et al. 1993; Cole et al. 1994). In the following, I give a simple introduction

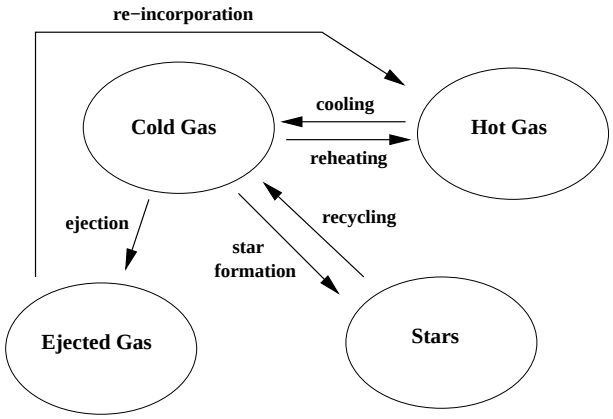

Figure 2.1: A schematic representation of how mass is exchanged between the different phases considered in semi-analytic models in the absence of accretion from outside. Coutesy of De Lucia et al. (2004)

to this method and its basic ingredients. More details can be found in a recent excellent review of semi-analytical models by Baugh (2006).

Modern semi-analytic models use the information on the formation and evolution of dark haloes discussed above. This information is usually organized in a tree structure that describes the accretion history of any given halo. There are two ways to construct these merging trees: one is based on Monte Carlo realizations of the merging paths of dark haloes based on the excursion sets theory (Kauffmann & White 1993). We have introduced this method in sec 2.2.3. Alternatively, one can build the merging trees from the direct N-body simulations (Springel et al. 2001). Following the galaxy formation scenario proposed by White & Rees (1978), when a dark matter halo forms, gas relaxes to a distribution that parallels that of dark halo and is shock heated to very high temperature. The gas can later cool and condense onto central galaxy at the center of the halo. Star formation and feedback processes take place according to the equations given in the previous section. At later time, the halo merges with a number of other systems, forming a new halo of larger mass. All gas that has not cooled is assumed to be heated to the virial temperature of the new halo. The cold gas and formed stars will stay at their own host substructures until dynamical friction erodes their orbits. Within an isolated galaxy, the different baryonic components will exchange matter by various physical processes. Fig. 2.1 gives a schematic representation of these exchanges. Each arrow is accompanied by a name indicating the physical process driving the corresponding mass exchange. In addition to the several main physical processes presented in last section, more physical models are at play, such as: the formation of black holes; the metal enrichment; dust model and stellar population synthesis models. Because so many complicated physical processes are involved, the models has a number of 'free' parameters. An "acceptable" galaxy formation model can be obtained by adjusting these free parameters to make the model galaxies match the observational data. This is also a major advantage of semi-analytical model: the effects of parameter variations within this model (or indeed alternative assumptions for some of the processes) can be

explored at relatively little computational expense since the model operates on the stored data base of merger trees; the simulation itself and the earlier stages of post-processing do not need to be repeated.

2.5 Observational tools

In the above sections, I summarized a number of issues related to structure formation in the standard cosmological models, and the two main methods used in this thesis. The question of how to test these theories and models using the observations now arises. Here I give a brief overview of this subject.

In general, the observed photons can be considered as a form of "fossil" information that tell us not only information about the radiation source, but also information about the space geometry, and the matter distribution along the photons' pathways that were disturbed by interactions with the medium matter.

The well-understood physics of these radiation source will help us a lot to understand the environments where the radiation source stay. One excellent example is the cosmic microwave background (CMB). The CMB average temperature tells us about the density of radiation field (Ω_r). The position of the acoustic features in the angular power spectrum of CMB temperature fluctuations provides a direct measurement of the angular size of sound horizon at recombination. The ratio of acoustic peak heights strongly depends on the baryon-to-photon ratio in the universe. The height of the third acoustic peak in the CMB power spectrum relates to the matter density. Another example of such a ridiation source is the forthcoming observations of high-z 21cm signals which will help us know more about what happened in the *dark age*.

Furthermore, the spectrum extracted from a population of photons can provide us more information about the radiation source. In fact the spectrum analysis is very important for studies of galaxies. One can read out most of the galaxy's physical properties from the spectrum, such as: mass and luminosity of different components, metallicity, temperature et al. All these observations can be used to test the galaxy formation models.

Well-understood radiation sources not only give us information about the radiation source, but also can be used to study the Universe. It is well known that some radiation sources can be used as standard candles or standard rulers to estimate the space geometry. Therefore, we can use the dependence of the obtained luminosity distance or angular distance on the cosmological parameters to constrain our cosmological models. Some often used standard candles or rules are:

Standard candles: Cepheids, high-redshift type Ia Supernovae; Tully-Fisher relation; luminous elliptical galaxy; (RR Lyrae variables and eclipsing binaries are also standard candles used to determine the matter distribution in the local universe) et al.

Standard rulers: position of peaks in CMB anisotropic power spectrum; baryon wiggles in the power spectrum of galaxies.

The spatial distribution of these radiation sources can also give us important information. For example, the shape of the matter power spectrum measured from galaxy redshift surveys such as SDSS or 2dF can tell us the matter density since the horizon scale at matter-radiation equality is embedded in the primordial power spectrum; The number density of

clusters can help us to determine the amplitude of the power spectrum. The distortion of power spectrum due to the peculiar velocities of galaxies can tell us the matter density. The growth factor measured from the surveys can also be used to constrain a range of cosmological parameters. The gas in clusters of galaxies is a main contributor to the baryon density and then can help us to determine the total matter density.

Interaction between the photons and the medium it passed through can give us more information about the medium. Two excellent examples are gravitational lensing and absorption systems of high redshift QuasiStellar Objects (QSOs). When a photon passes through a deep gravitational potential, it will be bent obeying the general theory of relativity. This distortion is called gravitational lensing. Because gravitational interaction has nothing to do with the type of lens, lensing is a very useful tool to detect the total matter distribution (including baryons and dark matter). For example, in the strong lensing case, the reconstruction of matter distribution of lens and the lens probability statistics could give us information on the density profile of dark matter in haloes. In the weak lensing case, the statistics of light distortions in a large area can provide information on the mass distribution on these scales. The absorption systems of QSOs are a very useful tool to gain information about the inter-galactic medium. The measure of the transmitted flux emitted from QSOs reflects directly the baryon density. The power spectrum of the flux $P_F(k)$ and the power spectrum of the matter distribution $P_m(k)$ can be related by $P_m(k) = b^2(k)P_F(k)$ if the bias function $b(k)$ is considered. The CMB photons also suffer different scattering process when they travel to us. For example, integrated Sachs-Wolfe effect due to the changes of gravitational potential; Sunyaev-Zel'dovich effect due to the inverse Compton scattering with high energy electrons, and the polarization effect due to the Thomson scattering with free electrons. Therefore, they also give us more information about the media it interacted. For example, the polarization signal in CMB photons is a powerful probe of the optical depth to the reionization epoch and can give some strong constrains on the cosmological reionization history.

In conclusion, the large number of observational tests, and of confirmations of the ΛCDM model, has turned cosmology into a "mature" science. The parameters of the big bang model are now known with great accuracy. Inflation has not been falsified, and its main predictions are strikingly consistent with observations. Structure formation and evolution are continuously tested with new observational data. It is believed that the pace of experimental and theoretical progress, however, does not seem to be close to a halt.

Chapter 3

Discreteness Effects in Simulations of Hot/Warm Dark Matter

Abstract

In Hot or Warm Dark Matter universes the density fluctuations at early times contain very little power below a characteristic wavelength related inversely to the particle mass. We study how discreteness noise influences the growth of nonlinear structures smaller than this coherence scale in N-body simulations of cosmic structure formation. It has been known for 20 years that HDM simulations in which the initial uniform particle load is a cubic lattice exhibit artifacts related to this lattice. In particular, the filaments which form in such simulations break up into regularly spaced clumps which reflect the initial grid pattern. We demonstrate that a similar artifact is present even when the initial uniform particle load is not a lattice, but rather a glass with no preferred directions and no long-range coherence. Such regular fragmentation also occurs in simulations of the collapse of idealised, uniform filaments, although not in simulations of the collapse of infinite uniform sheets. In HDM or WDM simulations all self-bound nonlinear structures with masses much smaller than the free streaming mass appear to originate through spurious fragmentation of filaments. These artificial fragments form below a characteristic mass which scales as $m_p^{1/3} k_{peak}^{-2}$, where m_p is the N-body particle mass and k_{peak} is the wavenumber at the maximum of $k^3 P(k)$ ($P(k)$ is the power spectrum). This has the unfortunate consequence that the effective mass resolution of such simulations improves only as the cube root of the number of particles employed.

3.1 Introduction

In the absence of a full analytic understanding of nonlinear structure growth, numerical simulations provide a critical link between the weak density fluctuations measured in the cosmic microwave background and the strong inhomogeneities observed on all but the very largest scales in the present Universe. Indeed, numerical simulations played a decisive role in excluding massive neutrinos as a dark matter candidate (White et al. 1983) and in establishing the ΛCDM model as the leading and now standard paradigm for the formation of all structure (Davis et al. 1985; White et al. 1987; Cen et al. 1994; Navarro et al. 1996).

With the development of more powerful computer hardware, of more accurate numerical algorithms, and of methods to follow additional physical processes, the importance of simulations as a tool to interpret observations of observed structure continues to increase dramatically. In this paper we are concerned with one aspect of the simplest kind of cosmological structure formation simulation, namely how discreteness effects can drive the growth of spurious small-scale structure in N-body simulations of evolution from initial conditions containing no such structure.

To create initial conditions for a cosmological simulation, a uniform particle distribution is needed. This can be perturbed by a random realisation of the linear fluctuation field associated with the specific structure formation model to be simulated (e.g. ΛCDM). A uniform Poisson distribution of particle positions is not suitable for this purpose, because stochastic "root-N" fluctuations can exceed the density fluctuations predicted by the desired model over a wide range of scales. To avoid this problem, most early simulations chose a regular cubic lattice as the initial uniform load. Symmetry then assures that there can be no growth of structure in the absence of imposed perturbations (Efstathiou et al. 1985). The preferred directions and the large-scale coherence of the lattice may, however, be a disadvantage, since they can give rise to numerical artifacts. As an alternative, White (1996) suggested using a glass-like initial particle load created by carrying out a cosmological simulation from Poisson initial conditions but with the sign of the peculiar gravitational accelerations reversed, so that each particle is repelled by all the others. When such a system reaches quasi-equilibrium, the total force on each particle vanishes, as for a grid, but there are no preferred directions and no long-range order. The power spectrum on scales much larger than the mean interparticle spacing approaches a power-law $P(k) \sim k^n$ with $n = 4$ (Baugh et al. 1995), where $n = 4$ is the minimal large-scale power expected for a discrete stochastic system (Peebles 1980,section 28).

Normally, grid and glass initial loads are considered equivalent. Nevertheless, artifacts due the initial lattice are obvious in early images of the sheets, filaments and "voids" formed in Hot Dark Matter (HDM) simulations (e.g. Centrella & Melott 1983; Frenk et al. 1984; Efstathiou et al. 1985; Centrella et al. 1988). Baugh et al. (1995) and White (1996) showed that low density regions appear very different in simulations with a grid initial load than in simulations started from a glass, although Baugh et al. found that this does not show up as a difference in their power spectra. Nevertheless, the regularly spaced clumps seen along filaments in HDM simulations are clearly related to the initial particle grid, and so seem unlikely to reflect a true physical instability. Despite this, Bode et al. (2001) and Knebe et al. (2003) interpreted analogous structures in their Warm Dark Matter (WDM) simulations (which were set up using a grid initial load) as the result of the physical fragmentation of filaments. The nonlinear formation of such small-scale structure could have important consequences in models like HDM or WDM where power on small scales is strongly suppressed in the linear initial conditions. It is thus important to establish which simulated structures are real and which are artifacts, as well as to understand whether the simulations can be improved by, for example, choosing a glass initial load in place of a grid.

Götz & Sommer-Larsen (2002, 2003) carried out WDM simulations using both grid and glass initial loads and reported significant differences. With a grid they found spurious low-mass halos evenly spaced along filaments, exactly as in earlier HDM experiments. The spacing is simply that of the initial grid, stretched or compressed by the large-scale

distortion field. They emphasised, however, that such unphysical halos were less evident in their simulations starting from a glass. This conclusion disagrees with our own work below, where we find spurious halos also in simulations from glass initial conditions and with a frequency very similar to that found in the grid case. Curiously, in the glass case also we find the spurious halos to be regularly spaced along filaments even though the initial condition is *not* regular over the relevant scales.

In this paper, we wish clarify this issue by isolating the numerical artifact, by exhibiting it in idealised filament formation simulations, by exploring its dependence on the nature of the uniform particle load, and by establishing the dependence of its characteristic scale on the discreteness scale of the simulation and the coherence scale of the WDM/HDM initial conditions. We carry out cosmological simulations of an HDM universe at a wide range of resolutions and with both grid and glass initial loads. In addition, we simulate the collapse of an infinite straight uniform density filament from glass initial conditions, showing that it fragments into regularly spaced clumps. To gain additional insight, we also consider the collapse of a glass to a uniform sheet, and the growth of structure in a uniform, space-filling, but anisotropically compressed glass. Rapid fragmentation on small scales occurs only in the filament case. Our tests also demonstrate that considerable care is needed to produce an initial glass load for which the growth of small-scale structure in filaments is optimally suppressed. We propose a randomisation technique which successfully washes out most code-dependent periodic signals in the initial load.

The remainder of our paper is organised as follows. In §3.2 we first discuss the aspects of our simulation code which are relevant to the problem at hand, in particular, how it estimates gravitational accelerations and how it is modified in order to create a uniform glass distribution. We then describe the way in which initial conditions are created for the simulations presented in the rest of the paper. §3.3 presents results from our Hot Dark Matter simulations, showing that all small-scale collapsed structures appear to form initially as regularly spaced clumps along filaments, and that these are similar for grid and for glass initial loads. Results for our studies of idealised structure formation from anisotropically compressed glasses are presented in §3.4. Rapid fragmentation on small scales occurs only in the filament case. §3.5 examines this filament fragmentation in more detail, showing that its characteristic scale is related to the interparticle separation for a well-constructed glass, but that scales related to the Poisson-solver of the glass-construction code can play an important role if their influence is not carefully controlled. Finally, §3.6 summarises the implications of our results for simulations of structure formation. In particular, we show that for nonlinear structures the effective mass resolution of simulations of HDM or WDM universes improves only as the cube root of the number of simulation particles employed. This is much more pessimistic than the direct proportionality to N which might naively have been expected.

3.2 Simulation methods and initial conditions

All simulations in this paper were performed using the massively parallel N-body code L-Gadget2. This is a lean version of Gadget2 (Springel 2005) with the SPH part excluded and with the memory requirements minimised. It was originally written in order to carry

out the *Millennium Simulation* (Springel et al. 2005).

The computation of gravitational forces is the most critical and time-consuming element of any cosmological N-body code. Gadget2 uses a hybrid tree-PM method where the long-range force is calculated at low resolution using a particle-mesh scheme, and is supplemented by a high-resolution but short-range correction calculated using a tree algorithm. The short-range correction is assembled in real space by collecting contributions from all neighbouring particles. The long-range force is calculated by assigning the particles to a regular cubic mesh, by using Fourier methods to obtain the corresponding potential, and by numerically differencing the result. For a single particle this scheme introduces a maximum force error of 1-2 percent near the split scale. Choosing a suitable split scale (typically several times the mean interparticle separation) results in force errors for smooth distributions of particles which are almost everywhere far below 1 percent. Gadget2 uses a space-filling fractal, the Peano-Hilbert curve, to control the domain decomposition associated with parallelisation. Because there is a good correspondence between the spatial decomposition obtained from this self-similar curve and the hierarchical tree used to compute forces, it is possible to ensure that the tree decomposition used by the code is independent of the platform, in particular of the number of processors on which it is run. In addition, the "round-off" errors in the forces induced when summing contributions from all processors are explicitly considered. As a result, the forces are independent of the number of processors and the domain cuts that are made. We believe that all code-related numerical effects relating to the calculation of gravitational accelerations are well under control in Gadget2.

Glass construction is embedded in Gadget2 by using some compile options. A preset number of particles is initially distributed at random within the cubic computational volume and the standard scheme is used to obtain the gravitational acceleration on every particle. After reversing the signs of the accelerations, all particles are advanced for a suitably chosen timestep. The velocities are then reset to zero and the whole procedure is repeated. After about a hundred steps the acceleration of each particle approaches zero. Notice that this is the acceleration as obtained by the code, including the effects of force anisotropy, domain decomposition, etc. Because the glass is made in a periodic cube, we can get a large glass file cheaply by tiling a big box with many replications of the original glass. However, the accelerations calculated by the code may no longer vanish exactly for this larger glass because the force anisotropies and inaccuracies now occur on a different scale than when the glass was created.

The FFT calculation and the Barnes & Hut tree used in Gadget2 are both based on static grids. This *spatially fixed* decomposition introduces weak periodic signals in the force calculation, and these are reflected in the particle distribution at the end of the glass-making procedure. We will see below that that this can introduce measurable spikes in the 1-D power spectrum of the final glass. To reduce such effects we randomly offset the particle distribution in all three coordinates with respect to the computational box before carrying out each force computation during glass-making. This suppresses the induced signals quite effectively but does not fully eliminate them. A glass constructed in this fashion is referred to as a "good" glass in the following, while a glass constructed without the random offset technique and showing significant high spikes is referred to as a "poor" glass. In the rest of this paper, we use "good" glasses for our initial conditions except where explicitly noted. These issues are further discussed in section 3.5.

Table 3.1: HDM simulations

name	$pre-IC$	$L[h^{-1}\mathrm{Mpc}]$	$m_p[h^{-1}M_\odot]$	$\epsilon(h^{-1}\mathrm{Mpc})$	n_p
glass64	glass	100	1.06×10^{12}	0.08	64^3
glass128	glass	100	1.32×10^{11}	0.04	128^3
glass256	glass	100	1.65×10^{10}	0.02	256^3
glass256-2	glass	200	1.32×10^{11}	0.04	256^3
glass512	glass	100	2.07×10^{9}	0.01	512^3
grid128	grid	100	1.32×10^{11}	0.04	128^3
qset134	Q-set	100	1.32×10^{11}	0.04	$\sim 134^3$

Below we consider grid initial loads in addition to glasses in order to compare their performance and to check the results of previous work (Bode et al. 2001; Götz & Sommer-Larsen 2002, 2003). A third quasi-uniform particle distribution, the Quaquaversal distribution, has recently been suggested by Hansen et al. (2007) as a non-periodic uniform initial load, a possible alternative to a glass. We have created such a Quaquaversal load with 2×8^7 particles using the code provided by Hansen et al at their web site, and we compare its performance to our grid and glass initial loads in an Appendix. It produces significantly worse discreteness artifacts than either grids or glasses.

Two types of simulation are considered below. The first is a series of cosmological simulations of evolution from Hot Dark Matter (HDM) initial conditions. Most of these are for a single realisation of the HDM density field within a $100h^{-1}$Mpc cube, but with different kinds of initial load and with varying mass resolution. One considers a $200h^{-1}$Mpc cube in order to better constrain the abundance of large objects. For these simulations, we choose an Einstein-de Sitter universe dominated by a single massive neutrino. We take $H_0 = 76.5\mathrm{kms}^{-1}\mathrm{Mpc}^{-1}$ which implies a neutrino mass of ~ 55eV and a corresponding free-streaming scale $\lambda = 22.2$ Mpc (Bond & Szalay 1983) below which initial fluctuations are exponentially suppressed relative to an assumed $P(k) \propto k$ primordial power spectrum. The power spectrum we actually use to impose fluctuations on our initial loads is based on the theoretical predictions of Bardeen et al. (1986) and agrees with numerical estimates from the Boltzmann solver CMBFAST (Seljak & Zaldarriaga 1996). Since the same realisation is used for all our $100h^{-1}$Mpc simulations, they should all produce identical structures. We start integrating at redshift $z = 20$ and evolve structure to a formal present-day amplitude of $\sigma_8 = 2$. This corresponds to the collapse of the first nonlinear structure in the simulation at $z \sim 6$. As a check of our starting redshift we reran one simulation glass128 starting from $z = 100$. At $z = 15$ the power spectrum of this simulation differed from that of the original run by few percent or less on all scales.

Our simulations are listed with their parameters in Table 3.1: pre-IC, L, m_p, ϵ,and n_p denote the initial load, the box size, the particle mass, the softening length, and the particle number respectively.

Our second type of simulation is designed specifically to study the discreteness artifacts which show up in the filamentary structures within our HDM simulations. These simu-

lations follow evolution from a variety of highly idealised initial conditions, all based on uniformly but anisotropically compressed glasses. We consider three different cases:

Anisotropic glass: The glass initial load is compressed by a factor of 2 along one axis, by a factor of 3 along a second axis, and is unaltered along the third axis. Six replications of this configuration are then used to tile the computational cube to produce an initial condition which is uniform and glass-like on large scales but where the forces are no longer balanced on the scale of the interparticle separation.

Sheet: The glass initial load is compressed along one dimension by a factor of 2, so that it fills half of the computational volume. The other half remains empty. This configuration collapses to form an infinite uniform sheet.

Filament: Our glass initial load is compressed by a factor of 2 along two of its periodic directions while the third remains unchanged. The particles then fill a quarter of the computational volume, the rest remaining empty. This configuration collapses to form a uniform straight filament.

All the simulations carried out from these initial conditions assume an Einstein-de Sitter background universe. We define the expansion factor a to be unity at the initial time.

We identify collapsed "halos" in our HDM simulations using a Friends-of-Friends (FOF) algorithm with linking length 0.2 times the mean interparticle spacing (Davis et al 1985). In the following we will only consider FOF halos with 32 or more particles. Subhalos within these halos were identified using the SUBFIND algorithm (Springel et al. 2001) with parameters set to retain all overdense self-bound regions with at least 20 particles. Based on these subhalo catalogues we use the techniques of Springel et al. (2005) to construct merging trees which allow us to follow the formation and evolution of all halos and subhalos.

3.3 Filament Fragmentation in HDM Simulations

The original motivation for this paper came from an unexpected phenomenon in our HDM simulations. Even when we use a glass initial load, we find that the filaments in these simulations break up into regularly spaced clumps, just as in early simulations based on grid initial loads. We illustrate this in Fig. 3.1 which shows a slice through simulation glass128. All FOF haloes with $32 \leq N_{fof} < 300$ are indicated by red points. It is obvious that many of these low-mass haloes lie in the filaments, and that they are surprisingly regularly spaced along them.

We find similar behaviour in all our HDM simulations, independent of the initial load and the mass resolution. In Fig. 3.2 we focus on a small cubic subregion containing a filament. (This region is indicated by a blue square in Fig. 3.1). In all four simulations, small clumps are visible at regularly spaced positions along the filament. Their spacing is very similar in the two 128^3 simulations, even though one started from a glass and the other from a grid. The spacing is reduced by about a factor of two in the 256^3 simulation and by about another factor of two in the 512^3 simulation. The clumps are difficult to see in this last case, but this is merely a consequence of the resolution of the image (compare Fig. 3.3 below). There are strong indications that these clumps are a numerical artifact, not least because in the grid128 case they line up with the distorted but still recognisable pattern

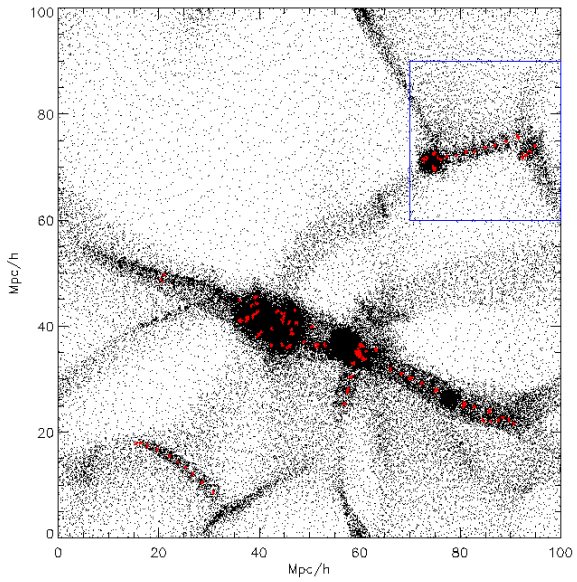

Figure 3.1: A slice of thickness $10h^{-1}$Mpc through the HDM simulation glass128 at $z = 0$. Small black points indicate individual simulation particles, while the larger red points show FOF halos with $32 \leq N_{fof} < 300$.

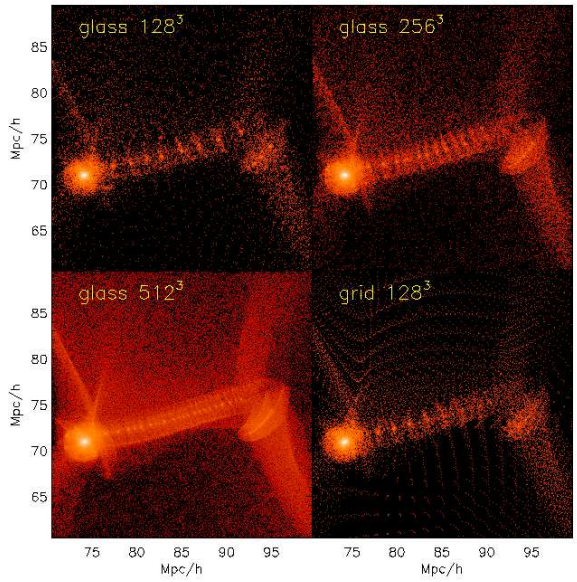

Figure 3.2: A subregion containing a filament at $z = 0$ in four of our $100h^{-1}$Mpc HDM simulations based on differing initial loads and differing mass resolution. The first three panels are taken from glass128, glass256 and glass512 respectively, while the last one (bottom right) is taken from grid128. The region shown here corresponds to that surrounded by a blue square in Fig. 3.1.

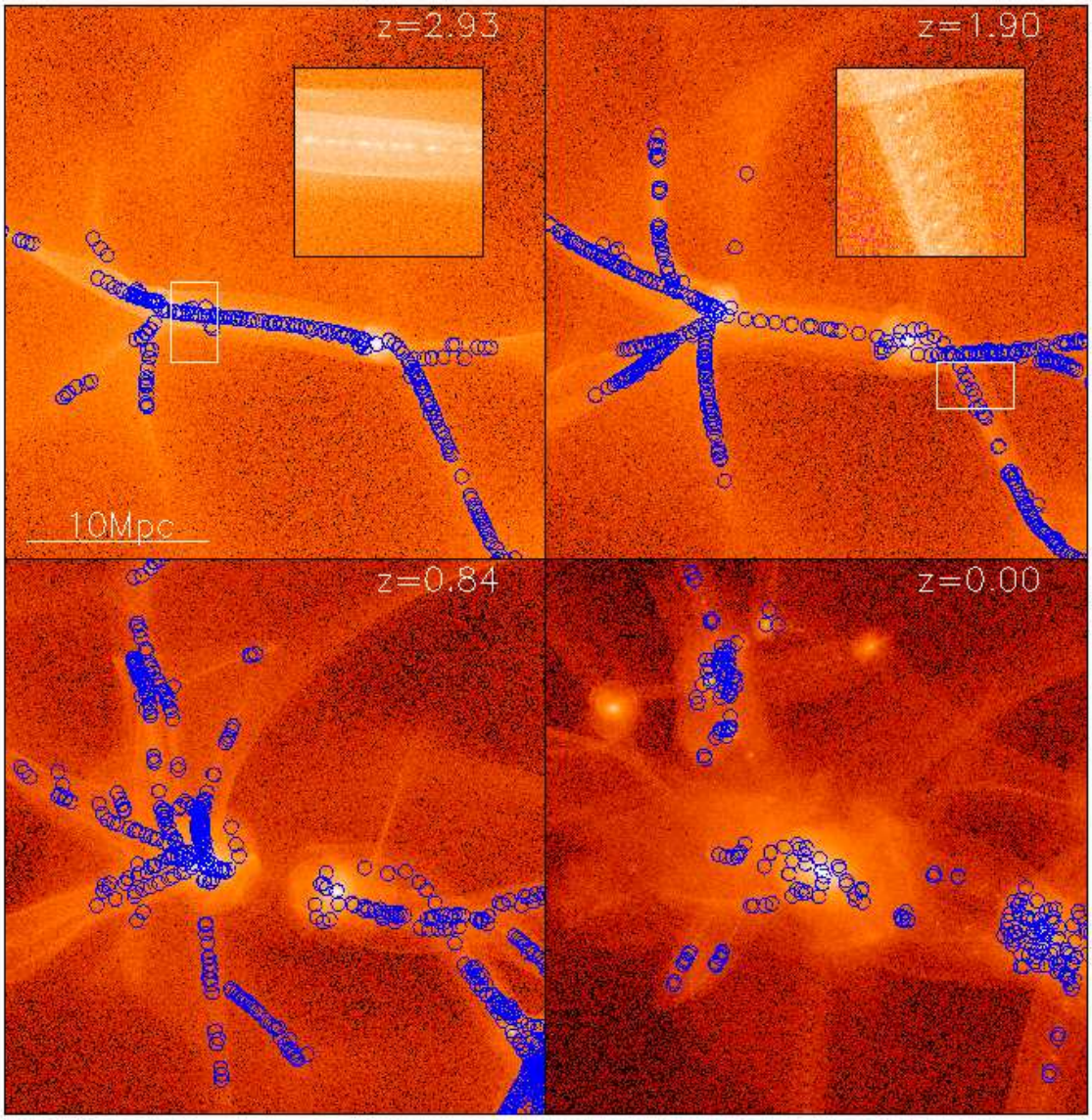

Figure 3.3: The bottom right panel shows a subregion of glass512 at $z = 0$ containing the largest FOF halo. The blue circles indicate all subhaloes with more than 20 particles within this object. The other three panels show the same subregion at earlier times ($z = 0.84; 1.90; 2.93$) with the blue circles now indicating the main progenitors of all the subhaloes identified at $z = 0$. It is striking that almost all these progenitors lie in 1-D structures — filaments — at the earlier times. The two smaller plots in the upper panels are stretched and magnified images of the filaments indicated by white rectangles in the main panels.

of the initial grid, just as in early HDM simulations (e.g. Centrella & Melott 1983) or in the WDM simulations of Götz & Sommer-Larsen (2003). Götz & Sommer-Larsen (2003) reported that the effect is absent when starting from a glass, although their Fig. 1 appears to show it in the filament at the lower right corner of their image. Bode et al. (2001) also noticed that many low-mass haloes formed in the filaments of their WDM simulation, but they interpreted this as a result of physical pancake fragmentation. The tight relation between clump scale and mass resolution manifest in Fig. 2 makes it clear, however, that this is actually a reflection of N-body discreteness effects. Its surprising aspect is that the regular clump spacing persists in the glass case where the initial load has no large-scale coherence. We consider this issue further below.

Another consequence of this artifact is illustrated in Fig. 3.3. It appears that almost all the subhaloes within the massive objects present at $z = 0$ actually originated through spurious filament fragmentation. Fig. 3.3 focusses on a small subregion of the glass512 simulation which contains the largest FOF halo, an object with several linked density centres at $z = 0$. The lower right panel shows the final mass distribution in this cubic region. All subhaloes with SUBFIND particle count greater than 20 are indicated by blue circles. The other three panels use our merging trees to trace the main progenitors of these subhaloes back to earlier times. All of them appear to form initially as evenly spaced "beads" strung along filaments. They later fall into the large halo where they are seen at $z = 0$. The artificial regularity of their formation is illustrated by the two zooms in the upper panels. We conclude that the first generations of haloes in pure HDM or WDM universes should contain no dark matter subhaloes of smaller mass scale.

3.4 Structure Growth in Idealised Glass Collapses

In our HDM simulations there is very little power in the imposed HDM power spectrum below the free-streaming scale. The regular fragmentation of the filaments is clearly related to the mesh for a grid initial load, but the origin of the equally regular fragmentation in the glass case is less obvious. In Fig. 3.4 we analyse the structure of a "good" 160^3 particle glass to search for signs of unexpected periodic behaviour. The irregular blue line in this figure is the dimensionless 3-D power per unit $\ln k$, $\Delta^2(k) = k^3 P_3(k)$ where $P_3(k)$ is the 3-D power spectrum. For comparison, the straight blue line gives the expectation for a Poisson distribution with the same number of particles ($P(k) = 1/N$). On large scales the power in the glass is far below this white noise level, with $\Delta^2(k) \propto k^7$ rather than $\Delta^2(k) \propto k^3$. For a relatively narrow frequency band near $k = 160$, however, the power is noticeably above the Poisson expectation. This corresponds approximately to the separation of the clumps which form on the filaments so there may be some connection to this artifact in our HDM simulations.

Fig. 3.4 also shows the power per unit $\ln k$ in 2-D and 1-D projections of this same glass, $\Delta^2(k) = k^2 P_2(k)$ and $\Delta^2(k) = k P_1(k)$ respectively. Again the measured results are compared to the expectation for a Poisson distribution with the same number of particles. Both cases show features directly analogous to those seen in the 3-D power spectrum. On large scales (small k) the power is strongly suppressed relative to the white noise level, with a spectrum which is steeper than white noise by four powers of k. Near $k = 160$ there is

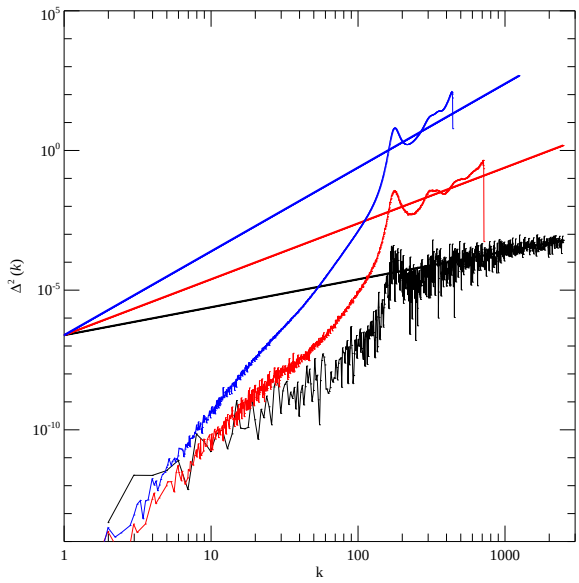

Figure 3.4: The 1-D (black), 2-D (red) and 3-D (blue) dimensionless power per unit $\ln k$ for a glass with 160^3 particles. The straight lines are the corresponding expectations for a Poisson distribution of 160^3 particles. The wavenumber k is given in natural units so that k=1 corresponds to the fundamental mode of the computational cube. The glass used here is a "good" glass, where random position offsets at each timestep were used to suppress artifacts due to anisotropies in the Gadget2 Poisson solver (see section 3.5).

a narrow range of wavenumbers where the power rises significantly above the white noise level. Again this feature could be related to the break up of sheets or filaments into clumps spaced regularly at about the mean interparticle separation.

Whether these features can indeed explain the unexpected fragmentation of filaments in our HDM simulations depends, of course, on how they are amplified as the particle distribution evolves. For the first structures to collapse in an HDM universe, this evolution can be idealised as a succession of three phases (Zel'dovich 1970). During early nonlinear growth, the tidal field causes a locally anisotropic flow which first reverses along a single preferred direction while continuing to expand (although at different rates) along the two orthogonal directions. In the second phase, collapse along the preferred axis gives rise to a quasi-two-dimensional sheet-like structure, a "pancake". Collapse along one of the other two axes then produces a filament. Finally, material flows along filaments to produce dark matter haloes at their intersections. These features are all clearly visible in Fig. 3.1, although in practice the different phases overlap and interact significantly. In Fig. 3.5 we show the results from a set of idealised simulations of anisotropic collapse designed to explore how discreteness noise grows for a glass initial load during these various phases.

To illustrate structure growth in the first of the above phases, the top panel of Fig. 3.5 shows the evolution of the total 3-D power per $\ln k$ for evolution from an anisotropically compressed, but space-filling and otherwise unperturbed glass. (It is easier for us to sim-

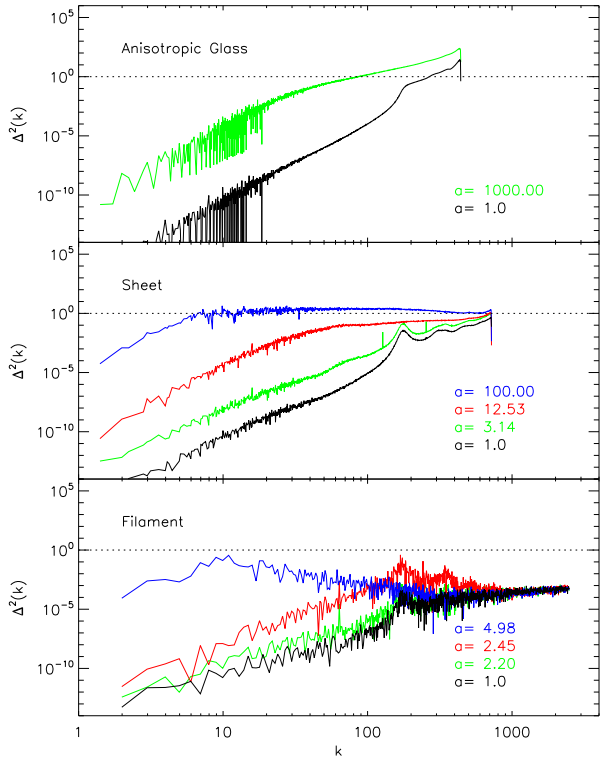

Figure 3.5: The evolution of the power per unit $\ln k$ in three idealised simulations. Top: the 3-D power at the initial time and after expansion by a factor of 1000 for an anisotropically compressed but space-filling glass. Centre: the 2-D power at the initial time and after expansion by factors of 3.1, 12.5 and 100 for the 1-D collapse of a compressed glass to a sheet. First collapse occurs at $a = 3.1$. Bottom: the 1-D power at the initial time and after expansion by a factors of 2.2, 2.4 and 5 for the 2-D collapse of a compressed glass to a filament. Here first collapse occurs at $a = 2.2$.

ulate the isotropic expansion of an anisotropically distorted glass than the anisotropic expansion of an initially isotropic glass.) The 160^3 "good" glass of Fig. 3.4 was here compressed by a factor of 2 along the x-axis and a factor of 3 along the y-axis, then replicated 6 times in order to tile the full simulation cube. The exact periodicities introduced by this procedure are responsible for the regular gaps in power visible at low k in the initial power histogram (the black curve in Fig. 3.5). It is interesting that the "bump" in power at the discreteness scale is broader than in Fig. 3.4 and now stretchess from near $k = 160$, the interparticle separation of the *original* glass past $k \sim 300$, the interparticle separation of the compressed glass. Clumping during expansion from this initial condition is extremely slow. The green curve shows the power distribution after expansion by a factor of 1000. By this time the matter has aggregated into small dense knots which typically contain 50 particles, but on larger scales the distribution remains almost uniform. At long wavelengths the power has grown by about six orders of magnitude, just as predicted by linear

theory. Thus the characteristic mass of the clumps grows as $M_* \propto a^{6/7}$. The amplification of discreteness noise is very weak during the first phase of anisotropic evolution from glass initial conditions.

The second panel of Fig. 3.5 studies the growth of discrete noise during and after collapse to a sheet. We compress our 160^3 glass by a factor of 2 along one axis, leaving the other half of the simulation cube empty. This initial condition collapses to a thin uniform sheet and thereafter remains thin with the particles oscillating about the symmetry plane. The figure shows the total 2-D power per $\ln k$ in the projection of particle distribution onto this plane at four different times: the initial time, the moment when the mass first collapses to a thin configuration ($a = 3.1$), the moment the sheet reaches minimum thickness for the second time ($a = 12.5$) and a substantially later time ($a = 100$). In this case the power on large scales grows much faster than in the previous case with Δ^2 increasing approximately as a^6 rather than as a^2. At the time of first collapse, the power in the discreteness peak has grown rather little, even though the power on larger scales has already amplified substantially. By the time of second collapse many nonlinear clumps are already evident in the projected mass distribution and the feature at the scale of the initial interparticle separation is no longer visible in the power spectrum. The characteristic nonlinear scale is determined by the point where the amplified long wavelength $\Delta^2 \propto k^6$ tail crosses $\Delta^2 \sim 1$. This scale increases rapidly with time, approximately as $M_* \propto a^3$. Structure in a pancake thus grows by an accelerated version of the standard hierarchical aggregation mechanism illustrated in a more familiar context in the top panel of Fig. 3.5. Discreteness effects do not appear to play a role other than by setting the initial amplitude of the long wavelength tail of $\Delta^2(k)$.

The lowest panel of Fig. 3.5 shows similar data for an idealised simulation of collapse to a filament. We compress our 160^3 glass by a factor of 2 along two orthogonal axes, leaving the remaining three quarters of the simulation cube empty. This bar-like initial condition collapses to a thin, straight filament. The figure shows the 1-D power per $\ln k$ for the projection of the particle distribution onto the axis of the filament at four different times: the initial time, the time of first collapse ($a = 2.2$), a time shortly thereafter ($a = 2.4$) and a significantly later time ($a = 5$). The power spectra here are considerably noisier here than in the top two panels because there are far fewer modes per bin in $\ln k$. By first collapse the large-scale power has grown substantially but there is rather little amplification near the discreteness peak at $k \sim 160$. This is similar to the sheet case. Shortly after first collapse, however, the power in the discreteness peak has grown by a large factor, reaching nonlinear levels. This shows up as regular clumping along the filament with a periodicity close to $k = 160$. It differs from the behaviour in the sheet case and is apparently analogous to the filament fragmentation we saw in our HDM simulations. We investigate it further in the next section. After the filament collapses the large-scale tail of the power distribution amplifies extremely rapidly, roughly as $\Delta^2 \propto a^{20}$. At the last time plotted this growth is again setting the nonlinear scale, as in the upper two panels, and there is no obvious feature near $k = 160$.

In all three of these tests the scale of nonlinearity at late times reflects the amplified small-k tail of the initial power spectrum of the glass. This tail grows much more rapidly in a sheet than in a uniform 3-D distribution and much more rapidly in a filament than in a sheet. The initial glass, if well made, does exhibit the theoretical minimum power on large scales $P(k) \propto k^4$ (Zel'dovich 1965; Peebles 1980), so that no better suppression

of discreteness effects can be hoped for. In the filament case, however, the *first* nonlinear structures are clearly different in nature and are related to the interparticle separation scale of the *uncompressed* glass. We now consider this instability more closely.

3.5 Fragmentation of filaments

In Fig. 3.6 we illustrate the evolution of the collapsing filament discussed in the last section. The first and second columns show projections perpendicular to and along the filament, while the third shows its 1-dimensional projected density. Only a tenth of the full length of the filament is plotted in order to make its structure more visible. Shortly after $a = 2$ the filament collapses to minimum thickness and at almost the same time it breaks up into regularly spaced clumps. The clump spacing is very nearly equal to the mean interparticle separation in the unperturbed glass; we find ~ 160 clumps along the full length of the filament. The number of clumps is independent of the FFT grid used. For 128^3, 243^3, 400^3 FFT grids, we find the total number of lumps to be always around ~ 160. Furthermore, we have repeated this fragmentation experiment with different compression factors in the initial condition. This changes the time of first collapse but it changes neither the fact that the filament breaks up just after first collapse, nor the spacing of the clumps. The same is true even if we adopt different compression factors along the two axes (provided both are well above unity) or if we impose an initial perturbation which is axially symmetric and has no sharp edges. Using an initial glass with a different number of particles produces a change in the interclump separation which scales as the cube-root of N. Clearly then, the break up is associated with a feature of the unperturbed glass.

The regular spacing of these artifacts indicates that modes with $k \sim N^{1/3}$ dominate at least the early nonlinear evolution of structure along the filament. This is visible in the left panels of Fig. 3.7, which repeat the power spectra at the initial time and at $a = 2.4$ (just after collapse) from Fig. 3.5. At the initial time the power around $k \sim 160$ is more than three orders of magnitude below the threshold for nonlinearity, but by $a = 2.4$ it is already approaching unity and is well above the power on all the other scales plotted. This is the reflection in Fourier space of the remarkable regularity seen in Fig. 3.6. The lower left panel of Fig. 3.7 plots growth factors for individual modes between the two times. The fastest growing modes have k somewhat smaller than 100, but their growth is insufficient for them to overtake the initial power peak near $k \sim 160$. The power in all the modes in this peak grows by a similar amount so the peak remains relatively narrow. This causes the regular spacing of clumps along the filament. Tests with a 270^3 particle glass show identical behaviour but with the peak shifted to $k \sim 270$. We conclude that the regularly spaced clumps which form on the filaments of our HDM simulations are produced by a narrow peak in power near the mean interparticle separation of our initial glass load. This peak is amplified to nonlinearity by the remarkably rapid growth of structure which occurs once a filament has collapsed.

Careful examination of Fig. 3.7 shows that there are particular modes for which the growth appears anomalously strong, notably those with $k = 64, 128, 256, 384....$ This is very likely a consequence of anisotropies in Gadget's Poisson solver which is based on a binary decomposition of the computational volume. For the "good" glass used here

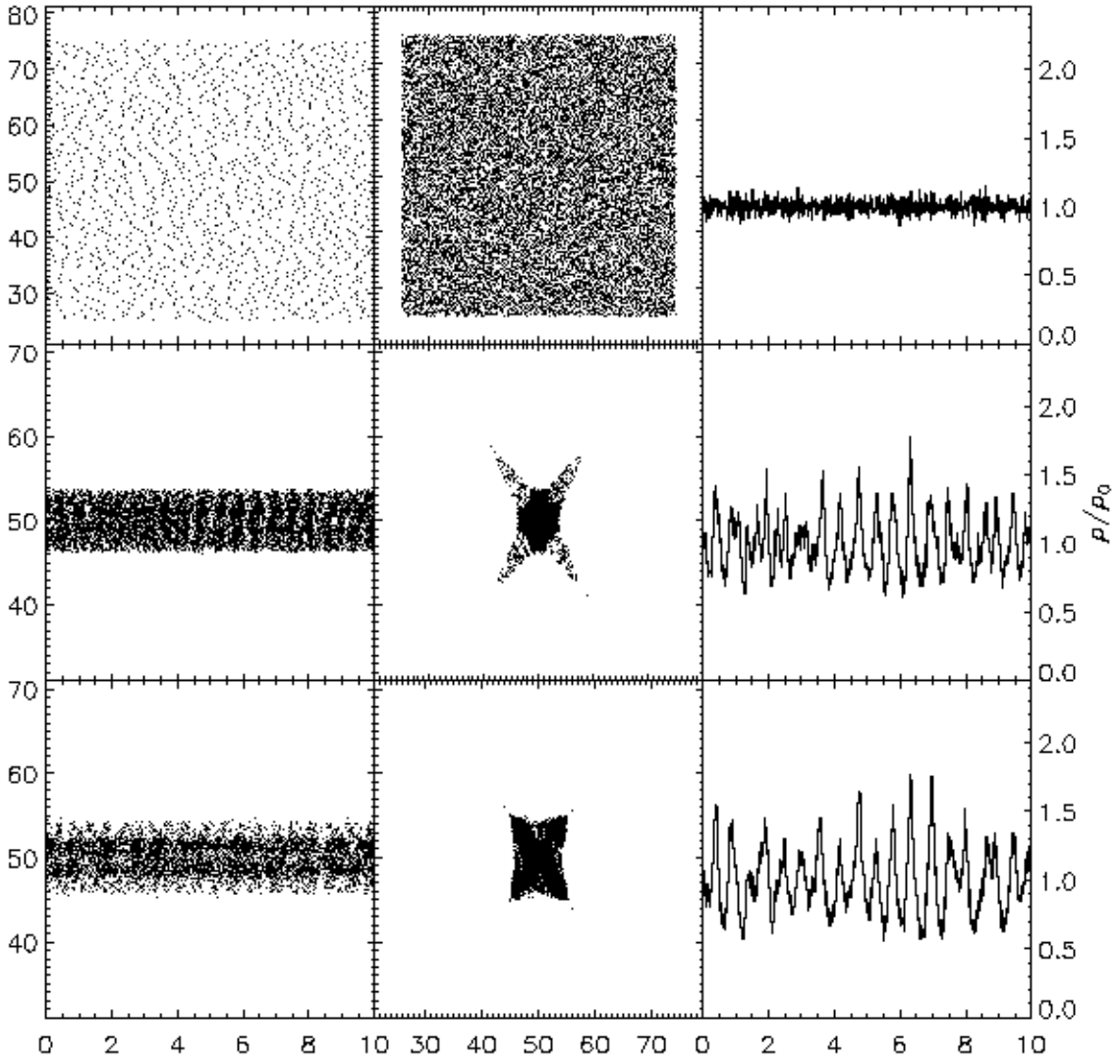

Figure 3.6: The evolution of an idealised infinite straight filament. The first and second columns are views perpendicular to and along the filament. Comoving coordinates are here normalised so that the side of the computational cube is 100. The third column is the 1-D number density profile along the filament. The density is normalised to unity and overdensities should be read off against the scale on the right-hand-side of the plot. Results are shown for expansion factors $a = 1, 2.4$ and 2.6, from top to bottom. For clarity only 1/10 of the whole filament is shown here. In fact, the total number of clumps lying along the filament is about 160.

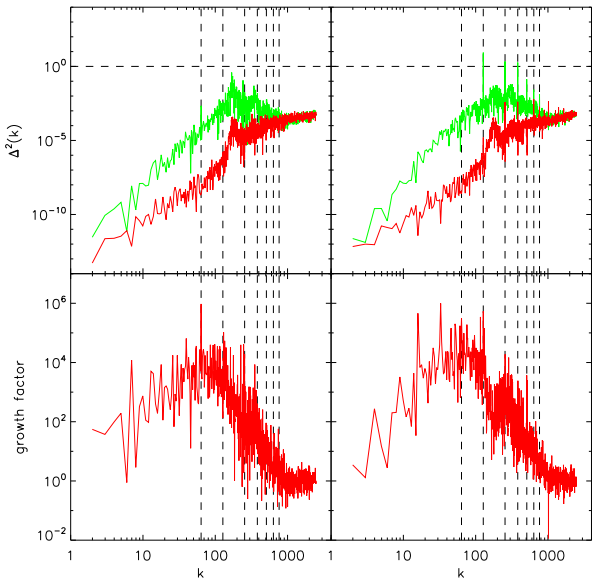

Figure 3.7: The top panels show the evolution of the 1-D power spectra corresponding to the simulations in Fig. 3.6 (a "good" glass: left) and Fig. 3.8 (a "poor" glass: right) which differ only in the initial glass used. The red curves represent the initial conditions ($a = 1$) while the green curves represent $a = 2.4$. The bottom panels show the growth factors between the two times plotted mode by mode. Note that these reach values in excess of 10^6. The dashed black vertical lines indicate modes $k = 64, 128, 256, 384, 512, 640, 768$. It can be seen that the growth factors are anomalously high for these modes in both panels, and that in the case of the "poor glass" a number of them are also anomalously high in the initial condition. As a result, at the later time the structure along the filament is dominated in the latter case by the modes with $k = 128, 256$ and 384.

these modes do not grow enough to overtake the power in the peak associated with the interparticle separation, so it is the latter which determines the initial fragmentation scale of the filament. We now show that this is not always the case.

Up to this point all our results have been based on such a "good" initial glass for which the offset technique discussed in §2 was used to minimise features due to anisotropies in the force calculations. Nevertheless, artifacts due to force anisotropies are still visible in some of our plots. For example, spikes can be seen in Fig. 3.5 at $k = 128$ and 256 in the $a = 3.1$ power spectrum of the sheet (these spikes are solely due to modes with wave-vector parallel to the fundamental axes of the computational cube) and at $k = 64$ and 256 in the $a = 2.4$ power spectrum of the filament (see also the left panels of Fig. 3.7). The growth factors in Fig. 3.7 show that these "special" modes grow substantially more rapidly than neighboring modes. If we do not use random offsets to reduce the impact of algorithmic boundaries in the force calculation, then features of this kind can be strong enough in the initial glass to significantly affect later evolution. An example is shown in the right panels of Fig. 3.7 and also in Fig. 3.8. Here we have carried out exactly the same filament collapse test as before, but using a "poor" initial glass constructed without using the offset technique. Spikes are

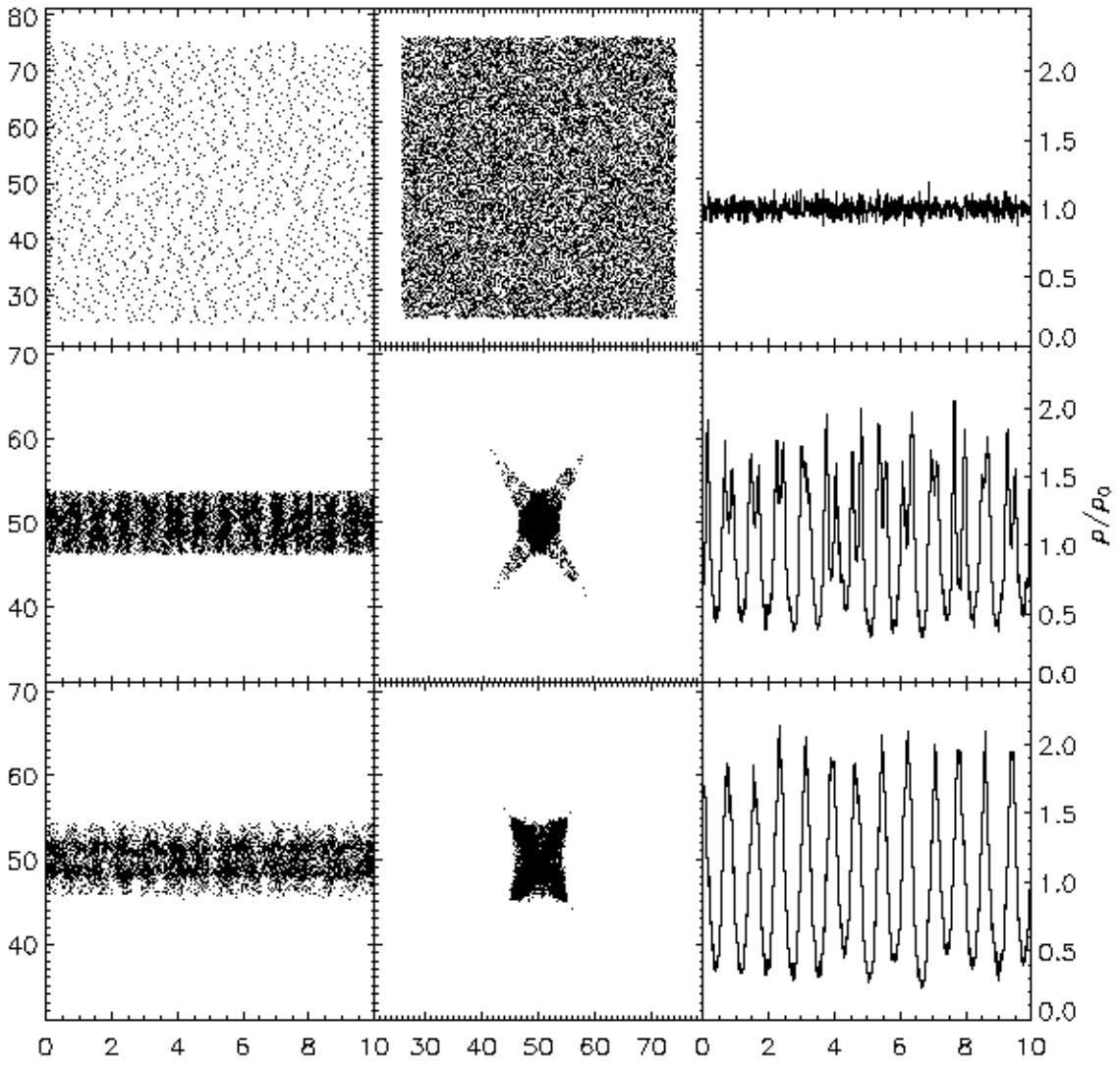

Figure 3.8: Similar to Fig. 3.6. but starting from a "poor" glass where the initial 1-D power spectrum shows spikes at $k = 64, 128, 256...$ There are about 128 clumps along the full length of the filament at the last time shown.

now visible at $k = 128, 256$ and 384 in the *initial* 1-D power spectrum. These are amplified by the evolution and at $a = 2.4$ the power is dominated by the amplified spike at $k = 128$ rather than by modes in the neighborhood of the discreteness peak at $k \sim 160$. Spikes at

$k = 256$ and 384 are also very strong and several other spikes are clearly visible. As Fig. 3.8 shows, these spikes cause the filament to break up initially into ~ 128 rather than ~ 160 clumps. Subsequent aggregation into larger objects is similar in the two cases, however, with large-scale effects overwhelming the initial differences.

Eliminating these troublesome power spikes from the initial conditions and from subsequent evolution is not easy. Changing the nominal accuracy of the force calculation affects the amplitude of the spikes but does not remove them. We were surprised to find that similar spikes are present in the initial glass used for the GIF simulations (Kauffmann et al. 1999a) even though this was created using a different code based on a P^3M Poisson solver. (For the GIF simulations the artifact was of no consequence, because of the substantial small-scale power imposed in the CDM initial conditions.) The large-scale PM force calculation in both codes imposes a regular "power of 2" spatial structure, and for Gadget-2 this is reinforced by the static Barnes-Hut oct-tree which underlies the calculation of the short range forces. The unexpected spikes appear to reflect these structural properties of the force construction algorithms. To test this, we projected the initial glass onto periodic directions which are *not* aligned with the axes of the computational box. The corresponding 1-D power spectra do not show any sharp spikes.

The tests in this section demonstrate that even with our random offset procedure artifacts due to our Poisson solver are not entirely eliminated. On the other hand, these tests are extremely sensitive to such artifacts because of the very high growth rates which occur in the idealised straight filaments we have been studying. While it is clearly important to be aware of the possibility of such numerical effects when simulating WDM or HDM universes, our results here show that for a carefully constructed glass the effects due to the Poisson solver remain subdominant with respect to effects caused by the discreteness of the particle distribution. The latter cannot be eliminated for any choice of initial particle load. They set the fundamental lower limit to the effective resolution of such simulations

3.6 Discussion and Conclusions

In this paper we have studied how discreteness effects limit the effective mass resolution of N-body simulations of cosmogonies like WDM or HDM where structure on small scales is suppressed in the linear initial conditions. Filaments occur in such models as part of the natural development of the cosmic web, but in simulations they fragment into regularly spaced clumps with a separation which reflects the mean interparticle distance in the initial load. These spurious clumps are responsible for all the low-mass substructures we have been able to identify at late times in collapsed halos. Thus, it appears that in an idealised WDM or HDM universe the first generations of dark haloes are predicted to contain *no* self-bound substructures of significantly smaller scale. Our tests on idealised systems show this fragmentation to occur because 1-D projections of a 3-D quasi-uniform particle distribution retain substantial power on the scale of the *3-D* interparticle separation, and this power amplifies very rapidly as the effectively 1-D system evolves.

We find (in disagreement with Götz & Sommer-Larsen (2002, 2003)) that spurious fragmentation of filaments occurs in almost identical fashion whether the initial particle load is a glass or a grid. Indeed, as we illustrate in Fig. 3.9, the effect appears slightly worse

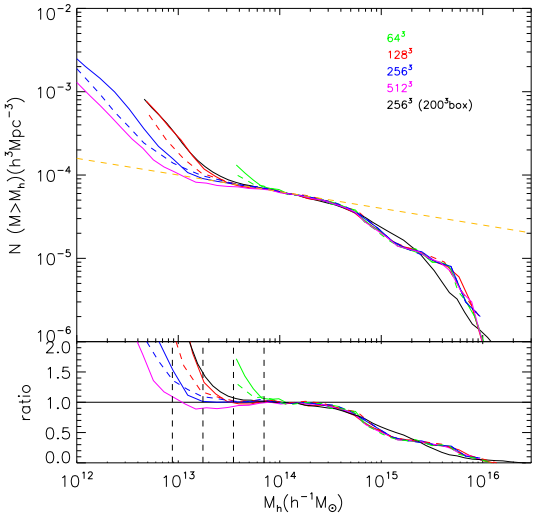

Figure 3.9: The cumulative halo mass function in eight simulations of an HDM universe. Seven of these start from the same realisation of the HDM density fluctuation field within a 100Mpc/h box, but use different initial particle loads. One follows evolution within a 200Mpc/h box in order to better constrain the high mass end of the mass function. Simulations starting from a glass initial load are indicated by solid lines, while those starting from a grid are indicated by dashed lines. The number of particles in each simulation is indicated by labels in the upper panel. The dotted line in this panel is an approximate power-law fit to the low-mass end of the mass function, $N \sim M_h^{-0.2}$, and the lower panel replots the mass functions relative to this power law in order to emphasise the upturn due to discreteness effects. Dashed vertical lines separated by factors of two provide a rough indication of the scale where spurious halos start to dominate in the various cases. The haloes here were identified using an FOF algorithm with $b = 0.2$ (Davis et al 1985).

for a glass than for a grid. This plot gives mass functions for 9 simulations from HDM initial conditions which use different particle numbers and different initial loads. In each case there is a sharp upturn in abundance at small masses which reflects the clumps visible within filaments in Figures 3.1 to 3.3. For initial loads of a given type this upturn shifts to smaller masses by a factor of 2 for each factor of 8 increase in the number of particles. For a given number of particles the upturn clearly occurs at somewhat larger masses in the glass case than in the grid case. Notice also that the upturn for the $N = 256^3$ glass simulation in a $200h^{-1}$Mpc box agrees very well with that for the $N = 128^3$ glass simulation in a $100h^{-1}$Mpc box. This confirms that it is the mean interparticle separation which sets the mass scale, rather than properties of the simulation code or of the particular HDM realisation simulated.

If we take the effective lower resolution limit of our HDM simulations to be given by the dashed vertical lines in the lower panel of Fig. 3.9, we find that it can be expressed

as $M_{lim} = 10.1 \times \bar{\rho}\ d\ k_{peak}^{-2}$, where $\bar{\rho}$ is the mean density of the universe, k_{peak} is the wavenumber at the maximum of $\Delta^2(k)$, the dimensionless power per $\ln k$ in the linear initial conditions, $d = N^{-1/3}L$ is the mean interparticle separation, N is the number of simulation particles, and L is the side of the computational box. For our HDM initial conditions $k_{peak} = 4.23 \times \lambda_{fs}^{-1} = 0.1 \times (m_\nu/30eV)\mathrm{Mpc}^{-1}$. The coefficient in our expression for $M_{\rm lim}$ is estimated directly from our HDM results. It may depend significantly on the shape of the primordial power spectrum and so need modification for WDM initial conditions. The scaling $M_{\rm lim} \propto N^{-1/3}$ should still hold in this case, however. Comparing our formula without modification to the numerical results of Bode et al. (2001) using $k_{peak} = 1.0$ and 0.5 Mpc^{-1}, as appropriate for their two WDM models, gives $M_{\rm lim} = 3 \times 10^{10}$ and $1.2 \times 10^{11} h^{-1}\mathrm{M}_\odot$. These values agree well with the upturns in the mass functions which they plot in their Fig. 9.

We can also compare with the WDM simulations presented by Knebe et al. (2002, 2003). These authors followed Bode et al. (2001) in arguing that small mass haloes form along filaments by top-down fragmentation. However, if we compare the mass functions they present for three different simulations in Fig. 4 of Knebe et al. (2002) and Fig. 3 of Knebe et al. (2003), we find the upturn at low mass for the two simulations with the same numerical resolution but different WDM particle mass to occur at masses which differ by about a factor of 4, while the upturn for the two runs with different numerical resolution but the same WDM particle mass also occur at masses differing by a factor of about 4. This is in roughly agreement with the scaling we predict for $M_{\rm lim}$ and is unexpected for a physical (rather than numerical) feature. We conclude that these results, as well as those of Bode et al. (2001) are consistent with a spurious numerical origin for the low mass halos in filaments similar to that we find in our HDM simulations. Furthermore, with our parametrisation of the characteristic scale based on the wavenumber at the peak of $\Delta^2(k)$, the dependence of the characteristic mass of the effect on the overall shape of the power spectrum appears to be weak.

This effective resolution limit is unfortunate news for simulations of HDM and WDM universes. In our highest resolution HDM model, for example, the $N = 512^3$ glass simulation of a 100Mpc/h box, the resolution limit is $M_{lim} = 8.8 \times 10^{12} h^{-1}\mathrm{M}_\odot$, which corresponds to a clump of 4300 simulation particles. Thus only halos with 5000 particles or more can be considered reliable. This is two or three orders of magnitude below the masses of typical big halos in the simulation. Contrast this with simulations of CDM universes where the positions, velocities and masses of haloes are reasonably well reproduced even for objects with about 100 simulation particles, giving a logarithmic dynamic range which is about twice as large. Furthermore the effective dynamic range in halo mass increases in proportion to N for CDM simulations, but only in proportion to $N^{1/3}$ in HDM or WDM simulations.

These results are interesting for the question of whether WDM models can reproduce the observed properties of dwarf satellite galaxies in the Milky Way. Available kinematic data for dwarf spheroidals suggest that they are sitting in dark matter halos with maximum circular velocities of order 30 km/s (e.g. Stoehr et al. 2002; Kazantzidis et al. 2004) corresponding to masses (for an *isolated* object) of about $10^{10}\mathrm{M}_\odot$. After discounting the spurious low-mass halos, the mass functions shown in Fig. 9 of Bode et al. (2001) demonstrate that halos of such small mass are not expected for a WDM particle mass of 175 eV

and are still strongly suppressed relative to ΛCDM for a mass of 350 eV. We infer that WDM particle masses well in excess of 500 eV will be necessary to produce "Milky Way" halos with sufficient substructure to host the observed satellites. This is, however, less stringent by a factor of several than constraints based on structure in the Lyman α forest (Viel et al. 2006). It will be interesting to carry out simulations of sufficient resolution to test whether the internal structure of subhalos in a WDM universe is consistent with that inferred for the halos of Milky Way dwarfs. The resolution limitations we have explored in this paper imply that, although possible, this will be a major computational challenge.

3.7 Appendix: The Quaquaversal distribution

Hansen et al. (2007) have suggested using an initial particle load constructed through a simple "Quaquaversal" tiling of space (sometimes known as a Q-set). In particular, they suggested using this initial load for WDM simulations. In this appendix, we show what happens if this distribution is used instead of a grid or glass initial load in a number of the tests we have studied in our paper.

A Q-set "lives" in a rectangular box with side ratio $1 : 1 : \sqrt{3}$, and requires a total particle number of the form $N = 2 \times 8^n$ with n an integer. Periodic boundary conditions can be assumed on opposite faces of the box to represent an infinite cosmological distribution. Fig. 3.10 compares the 3-D power spectrum of such a distribution with that of our "good" 160^3 glass. This Q-set has $n = 7$, resulting in a total of $N = 4194304$ particles, and was set up using the codes provided by Hansen et al. (2007). In order to facilitate the comparison we shift $P(k)$ for the Q-set so that its white noise level is at 160^{-3} and the mode number $k = 1$ corresponds to a wavelength 160 times the mean interparticle spacing. At all scales significantly larger than the mean interparticle spacing, the power in the Q-set lies well above that in the glass. The mean power declines approximately as $k^{3.4}$ for small k rather than as k^4, and there is substantial power in a series of additional narrow peaks separated by factors of 2 in k.

We have used this Q-set as the initial particle load for our standard $100h^{-1}$Mpc box HDM simulation. Since this simulation is carried out in a cubic region we need to chop off the long end of the Q-set rectangular box leaving a total of $2424140 \sim 134^3$ particles in the simulation. This truncation results in a violation of periodicity in the initial load for one pair of faces of the cubic volume. As a result, spurious small clumps form along this interface during later evolution, but these effects do not propagate into the rest of the simulation. They are not visible in Fig. 3.11, which is a slice through the simulation to be compared directly with Fig. 3.1. We exclude a thin slice of the simulation which contains this discontinuity when we calculate the halo mass function at $z = 0$. This is displayed in Fig. 3.12 and compared to our earlier results.

A comparison of Fig. 3.11 with Fig. 3.1 shows that the regularities of the Q-set are much more visually apparent than those of the glass, particularly in low density regions. The small halos indicated by red points are again found along filaments and on the outskirts of massive objects. Fig. 3.12 shows that the Q-set reproduces the halo mass function of our other simulations at high mass, but that the turn-up due to spurious low-mass halos occurs at significantly higher mass than for glass or grid initial loads. The effective mass

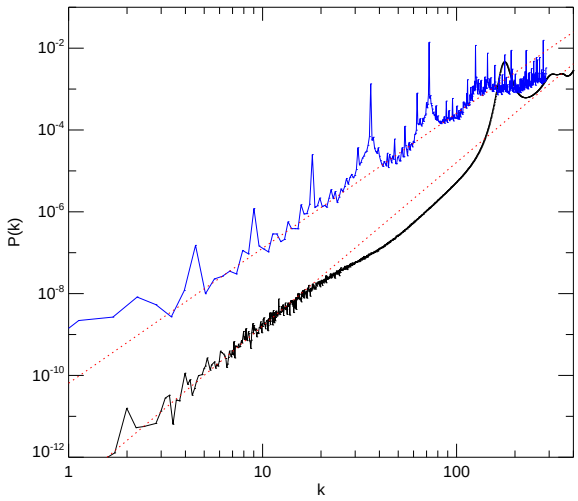

Figure 3.10: 3-D power spectra $P(k)$ for a Q-set (black) and for the "good" $N = 160^3$ glass already used in Fig. 3.4 (blue). The Q-set has 4194304 particles in a rectangular box. Its power spectrum is normalised so that its white noise level is at 160^{-3}, just as for the glass. In addition, the units of wave number are chosen so that $k = 1$ corresponds to a wavelength 160 times the mean interparticle separation for both distributions. Red dotted lines indicate power laws with slope 4 and 3.4 which are good fits to the glass and Q-set power spectra respectively on large scales.

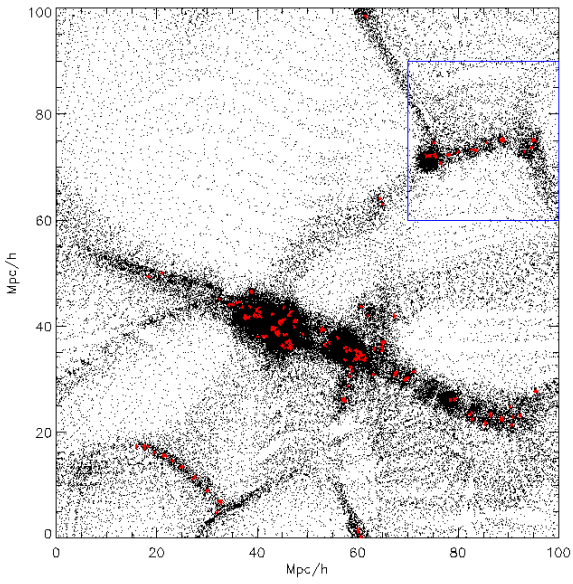

Figure 3.11: A slice through an HDM simulation directly comparable to Fig. 3.1, but for a simulation with a Q-set initial load.

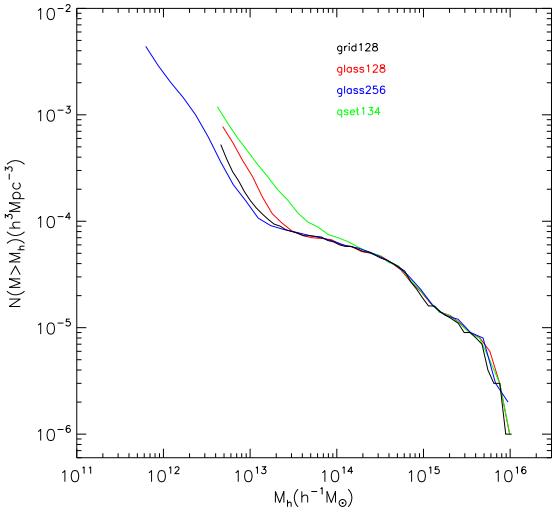

Figure 3.12: Mass functions for FOF haloes in four HDM simulations started from identical realisations of the HDM fluctuation field but with different initial particle loads. Two start from glass loads with $N = 128^3$ (red) and $N = 256^3$ (blue) and one starts from a grid with $N = 128^3$. All three of these were already shown in Fig. 3.9. The final simulation starts from a Q-set initial load with $N \simeq 134^3$.

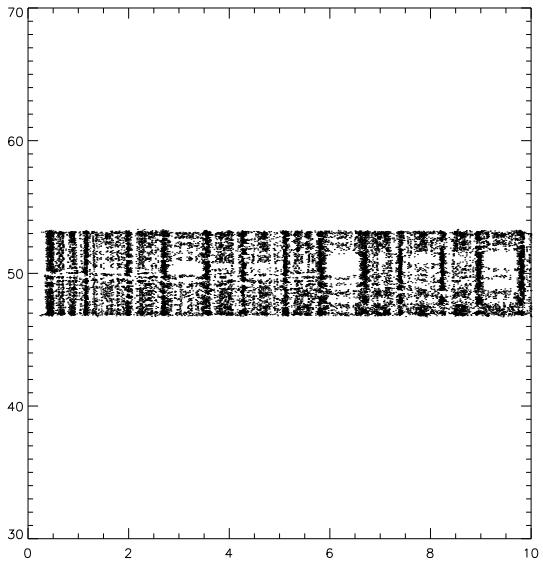

Figure 3.13: Idealised filament collapse as in Fig. 3.6 but starting from a compressed Q-set initial condition. The distribution of particles in a section of the filament is shown at $a = 2.2$ and should be compared directly with the middle left panel of Fig. 3.6.

resolution of the Q-set simulation is about a factor of three worse than in either of the other cases.

We have also carried out our standard idealised filament simulation starting from a compressed Q-set rather than a compressed glass. The particle distribution along a section of the filament is shown just after collapse in Fig. 3.13 for comparison with the central left-hand panel of Fig. 3.6. Substantial and regular clumping is seen, although the regularity is considerably more complex (and also stronger) than in the glass case. As in the glass case, the clumps rapidly aggregate into a small number of massive objects during later evolution. The different initial power spectra of the glass and Q-set cases (Fig. 3.10), result in different rates of growth of structure along the filament at later times. Structures are always more massive are arranged in a more complex pattern along the filament for Q-set than in the glass case.

Our conclusion from these tests is that for given particle number the Q-set performs significantly worse as an initial load than either a grid or a glass. Since the visual regularities it induces are very similar to those seen for a grid and are much stronger than those found with a glass, there does not seem to be any obvious situation where a Q-set would be the preferred choice for an initial quasi-uniform particle load.

Acknowledgements

We thank Volker Springel for help in devising a glass-making scheme which suppresses Poisson-solver-induced power spikes. We thank Adrian Jenkins for the suggestion to consider idealised bar collapses. We thank both of them and also Liang Gao for a number of very useful discussions of the material presented in this paper.

Chapter 4

The Dependence of Galaxy Formation on Cosmological Parameters: Can we distinguish the WMAP1 and WMAP3 Parameter Sets?

Abstract

We combine N-body simulations of structure growth with physical modelling of galaxy evolution to investigate whether the shift in cosmological parameters between the 1-year and 3-year results from the Wilkinson Microwave Anisotropy Probe affects predictions for the galaxy population. Structure formation is significantly delayed in the WMAP3 cosmology, because the initial matter fluctuation amplitude is lower on the relevant scales. The decrease in dark matter clustering strength is, however, almost entirely offset by an increase in halo bias, so predictions for galaxy clustering are barely altered. In both cosmologies several combinations of physical parameters can reproduce observed, low-redshift galaxy properties; the star formation, supernova feedback and AGN feedback efficiencies can be played off against each other to give similar results. Models which fit observed luminosity functions predict projected 2-point correlation functions which scatter by about 10-20 per cent on large scale and by larger factors on small scale, depending both on cosmology and on details of galaxy formation. Measurements of the pairwise velocity distribution prefer the WMAP1 cosmology, but careful treatment of the systematics is needed. Given current modelling uncertainties, it is not easy to distinguish the WMAP1 and WMAP3 cosmologies on the basis of low-redshift galaxy properties. Model predictions diverge more dramatically at high redshift. Better observational data at $z > 2$ will better constrain galaxy formation and perhaps also cosmological parameters.

4.1 Introduction

Our current understanding of the cosmic evolution is based heavily on measurements of the Cosmic Microwave Background (CMB). The discovery of the CMB (Penzias & Wilson 1965) led to general acceptance of the Hot Big Bang theory, and further support came from

the subsequent demonstration of its near-perfect black-body spectrum (Mather et al. 1990). The detection and continuing refinement of measures of angular structure in the CMB confirmed theoretical predictions for the growth of structure in flat cosmologies dominated by non-baryonic Cold Dark Matter (CDM) (Smoot et al. 1990; de Bernardis et al. 2000, 2002). The power spectrum of this structure encodes information about the values of the cosmological parameters, although degeneracies prevent a precise determination of all parameters from CMB data alone. By including constraints from other kinds of data, it becomes possible to constrain many cosmological parameters quite tightly. During the last decade, a growing body of such measurements have ushered in a new era of 'precision cosmology'.

The first-year data from the Wilkinson Microwave Anisotropy Probe (WMAP) (Spergel et al. 2003) did much to establish ΛCDM, a flat CDM model with a cosmological constant, as the standard model for structure formation. In addition, they provided apparently precise estimates for a number of cosmological parameters. Two further years of WMAP data have significantly refined these estimates, leading to noticeable shifts in some of the best values (Spergel et al. 2007). The most important differences are a reduction in optical depth to the last scattering surface (τ), a lower value for the amplitude of matter fluctuations on $8\,h^{-1}\,\mathrm{Mpc}$ scale (σ_8), a reduction of the scalar spectral index on primordial perturbations (n), and a lowering of the total matter density (Ω_m).

Several studies prior to the latest WMAP results suggested a lower value for σ_8. These looked at evolution in the abundance of galaxy clusters (Borgani et al. 2001; Schuecker et al. 2003), and at constraints from the abundance and clustering of low-redshift galaxies in combination with observed cluster mass-to-light ratios (van den Bosch et al. 2003; Tinker et al. 2005). Parameter estimates from these methods are partially degenerate in σ_8 and Ω_m and other studies, notably of cosmic shear, have tended to give conflicting indications (e.g, Massey et al. 2007; Benjamin & et al. 2007; Hoekstra et al. 2006). Recent studies on giant arc statistics (Li et al. 2006) also suggest that low values of σ_8 may be difficult to reconcile with the observations. It is only the shrinking of the allowed parameter region forced by the new WMAP data that has persuaded much of the astronomical community to prefer a "standard" model with a lower value of σ_8. It should be remembered, however, that including parameters beyond the usual minimal set significantly relaxes constraints, so that both first- and third-year WMAP parameter sets should probably be treated as plausible.

Modifications of the cosmological parameters of the kind discussed above can significantly affect the formation and evolution of structure. Recent studies have discussed the implications of WMAP third-year results for the formation of the first stars and black holes, and for the reionization of the intergalactic medium (Gao et al. 2007; Alvarez et al. 2006; Popa 2006; Lewis et al. 2006; Iliev et al. 2007), finding significantly later formation and reionization than previously thought.

The present paper investigates the impact of this delay on the observed properties of galaxies, both at low and at high redshift. We combine high-resolution N-body simulations with semi-analytic modelling techniques to simulate the evolution of the galaxy population (Springel et al. 2005; Croton & et. al 2006; De Lucia & Blaizot 2007). Our paper is organised as follows: the N-body simulations and the semi-analytic modelling assumptions are described in sections 4.2 and 4.3. In section 4.4 we discuss the formation of dark matter structures in cosmologies with first-year and third-year WMAP parameters, while

in section 4.5 we compare simulations of the evolution of the galaxy population in these two cosmologies. Finally, in section 4.6 we summarise and discuss our findings. For the convenience of the reader we also provide an appendix containing an analytic comparison of evolution in the abundance and clustering of dark halos in our two cosmologies, based on the formulae of Mo & White (2002)

4.2 The Simulations

We have carried out two simulations of the growth of structure in a ΛCDM Universe using the cosmological parameter sets listed in Tab. 4.1. The cosmological parameters used for our WMAP1 simulation are derived from a combination of first-year WMAP results (Spergel et al. 2003) with the 2dFGRS galaxy power spectrum (Colless et al. 2001), and correspond to those used for the *Millennium Simulation* (MS; Springel et al. 2005). Our WMAP3 simulation adopts cosmological parameters derived from a combination of third-year WMAP data on large scale, and Cosmic Background Imager (CBI) and extended Very Small Array (VSA) data on small scale (Spergel et al. 2007). We note that, among the different sets of cosmological parameters consistent with the third-year WMAP data and other observational data, we have chosen to look at the one which differs the most from the parameters of our WMAP1 simulation.

The most significant difference between the two sets of parameters listed in Table 4.1 is in the lower value of σ_8 adopted for the WMAP3 simulation. Our WMAP1 and WMAP3 cosmologies also differ in the scalar spectral index of primordial density perturbations ($n = 1 \rightarrow 0.947$), and in the matter density ($\Omega_m = 0.25 \rightarrow 0.226$). As noted above, a number of recent studies have shown that this change in cosmology results in a significant delay of structure formation in the WMAP3 case in comparison to WMAP1. We will discuss this in more detail in the following section.

The numerical parameters used for our simulations are listed in Table 4.2. The mass and force resolution are the same as used for the MS, while the volume is a factor 64 smaller. We have stored the data at the same 64 output times as in the MS. These are approximately logarithmically spaced between $z = 20$ and $z = 1$ and approximately linearly spaced in time thereafter. Friends-of-friends (FOF) group catalogues were computed on the fly for each snapshot, and the algorithm SUBFIND (Springel et al. 2001) was employed to decompose each FOF group into a set of disjoint substructures. As in Springel et al. (2005), only substructures which retain at least 20 bound particles after a gravitational unbinding procedure are considered to be genuine substructures. Substructure catalogues are then used to construct detailed merger history trees that provide the basic input needed for the semi-analytic model described in the next section. We refer to Springel et al. (2005) for more details of the merger-tree construction. Both our simulations were run using the tree-based parallel code GADGET2 (Springel 2005). The initial power spectra were generated using CMBFAST (Seljak & Zaldarriaga 1996) with the cosmological parameters listed in Tab. 1 as input. The Fourier modes of the initial density field in the two cases were identical except for the amplitude adjustment needed to reproduce the correct power spectrum. Thus structures correspond closely in the two cases.

Fig. 4.1 shows the power per decade in the linear initial conditions of our WMAP1 (blue)

Table 4.1: Cosmological parameters of the two simulations used in this study. Ω_m, Ω_Λ, Ω_b are the density of matter, dark energy and baryons respectively. σ_8 and n are the amplitude of the mass density fluctuations, and slope of initial power spectrum. The Hubble constant is parameterised as $H_0 = 100\,h\,\mathrm{km\,s^{-1}Mpc^{-1}}$.

	WMAP1	WMAP3
Ω_m	0.25	0.226
Ω_Λ	0.75	0.774
Ω_b	0.045	0.04
σ_8	0.9	0.722
h	0.73	0.743
n	1	0.947

Table 4.2: Numerical parameters of our two simulations. L is the box size, n_p is the particle number, ϵ is the softening length, and m_p is the particle mass.

L	n_p	ϵ	m_p(WMAP1)	m_p(WMAP3)
$125\,\mathrm{Mpc}\,h^{-1}$	540^3	5kpc	$8.61e8\mathrm{M}_\odot\,h^{-1}$	$7.78e8\mathrm{M}_\odot\,h^{-1}$

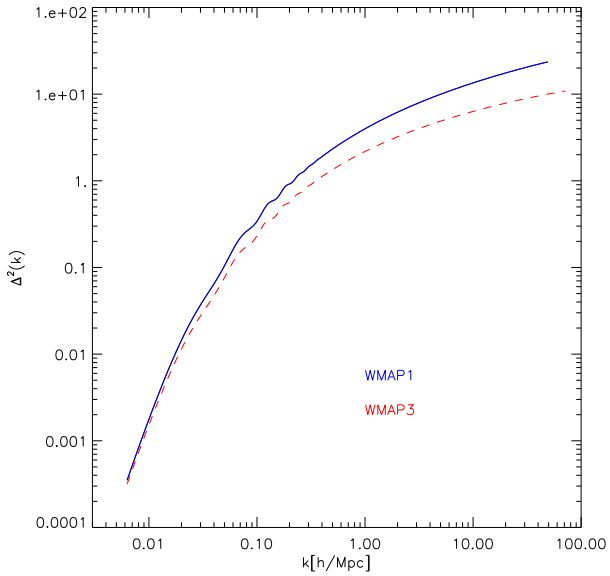

Figure 4.1: The power spectra of our two simulations: WMAP1 (blue solid) and WMAP3(red dashed). These were generated using CMBFAST with the cosmological parameters listed in Tab. 4.1. The quantity plotted is $\Delta^2(k) \propto k^3 P(k)$.

and WMAP3 (red) simulations. The significantly lower value of σ_8 in the WMAP3 case reduces the overall normalisation. In addition, the red tilt in the primordial power spectrum index makes the difference greater on small scales than on large scales. Indeed, on the scales responsible for the low ℓ microwave background fluctuations the two power spectra are almost the same, reflecting the fact that they are both required to fit observed CMB fluctuations on these scales. Conversely, the suppression of power is particularly significant on the small scales responsible for the formation of the first nonlinear structures.

4.3 The Semi-Analytic Model

In this paper we use the galaxy formation model described in De Lucia & Blaizot (2007) which is based on the WMAP1 cosmology and builds on previous work by the "Munich" galaxy formation group (Kauffmann et al. 1999a; Springel et al. 2001; De Lucia et al. 2004; Springel et al. 2005; Croton & et. al 2006). Although not in perfect agreement with all aspects of the local galaxy population (see, for example, Weinmann et al. (2006)), this model does quite a good job of reproducing the observed relations between stellar mass, gas mass, and metallicity (De Lucia et al. 2004), the observed luminosity, colour, and morphology distributions (Croton & et. al 2006; De Lucia et al. 2006) and the observed two-point correlation functions (Springel et al. 2005). Kitzbichler & White (2007) have recently shown that it also agrees reasonably well with the observed galaxy luminosity and mass functions at high redshift. We refer the reader to the original papers for a full description of the numerical implementation, and of the physical processes modelled. In the following, we summarise briefly the treatment of those physical processes for which we needed to change the efficiency parameters in order to maintain agreement with observations of the local galaxy population when we switch from WMAP1 to WMAP3 (see Table 4.3 and Sec. 4.5).

In the semi-analytic model we use in this work, star formation is assumed to occur at a rate given by:

$$\dot{m}_* = \alpha_{\rm SF}(m_{\rm cold} - m_{\rm crit})/t_{\rm dyn,disc} \tag{4.1}$$

where $m_{\rm cold}$ and $t_{\rm dyn,disc}$ are the cold gas mass and the dynamical time of the galaxy, defined as the ratio between the disk radius and the virial velocity, $m_{\rm crit}$ corresponds to a critical value for the gas surface density (Kennicutt 1998; Kauffmann 1996; Mo et al. 1998), and $\alpha_{\rm SF}$ controls the efficiency of the transformation of cold gas into stars when the gas surface density is above the critical value. (See Croton & et. al (2006) for more detailed descriptions of the implementation of this process and of the feedback processes described below.)

Massive stars explode as supernovae shortly after a star formation event and are assumed to reheat a gas mass that is proportional to the mass of stars formed (based on the observations of Martin 1999):

$$\Delta m_{\rm reheated} = \epsilon_{\rm disk}\Delta m_*, \tag{4.2}$$

Again following Croton & et. al (2006), we write the energy released by an event which forms a mass Δm_* in stars as:

$$\Delta E_{\rm SN} = 0.5\epsilon_{\rm halo}\Delta m_* V_{SN}^2, \tag{4.3}$$

where $0.5V_{\rm SN}^2$ is the mean supernova energy injected per unit mass of newly formed stars, and $\epsilon_{\rm halo}$ represents the efficiency with which this energy is able to convert cold interstellar medium into hot, diffuse halo gas. The amount of gas that leaves the dark matter halo in a "super-wind" is determined by computing whether excess SN energy is available to drive the flow after reheating of material to the halo virial temperature.

As in Kauffmann & Haehnelt (2000), black holes are formed and fuelled during mergers:

$$\Delta m_{\rm BH} = \frac{f'_{\rm BH} m_{\rm cold}}{1 + (280{\rm kms}^{-1}/V_{\rm vir})^2} \tag{4.4}$$

We assume here that black holes grow during both major and minor mergers, and that the efficiency of gas accretion onto the black hole scales with the baryonic mass ratio of the merging galaxies:

$$f'_{\rm BH} = f_{\rm BH} \times (m_{\rm sat}/m_{\rm central}) \tag{4.5}$$

This is the primary process driving the growth of the total mass in supermassive black holes. Individual black holes can also gain mass through merging when their host galaxies merge.

Finally, we use the model by Croton & et. al (2006) to describe heating by centrally located AGN in massive groups and clusters. This process is assumed to be associated with "radio mode" outflows which suppress cooling flows and thus the condensation of gas onto the central galaxies. The process is assumed to occur whenever a massive black hole finds itself at the centre of a static hot gas halo. During this phase, the accretion rate onto the central supermassive black hole is taken to be:

$$\dot{m}_{\rm BH,R} = \kappa_{\rm AGN} \left(\frac{m_{\rm BH}}{10^8 M_\odot}\right) \left(\frac{f_{\rm hot}}{0.1}\right) \left(\frac{V_{\rm vir}}{200{\rm kms}^{-1}}\right)^3, \tag{4.6}$$

where $m_{\rm BH}$ is the black hole mass, $f_{\rm hot}$ is the fraction of the total halo mass in the form of hot gas, $V_{\rm vir}$ is the virial velocity of the halo, and $\kappa_{\rm AGN}$ is efficiency parameter with units of $M_\odot {\rm yr}^{-1}$. The energy released during this accretion process is used to reduce the cooling flow. Croton & et. al (2006) showed that this results in complete suppression of cooling in relatively massive haloes and groups. The process starts being effective at a mass scale that evolves as a function of redshift as shown in their Fig. 7.

In our simulation scheme, haloes (and the galaxies within them) are followed even after they are accreted onto larger systems. The dynamics of such a satellite subhalo is followed explicitly by the N-body simulation until tidal stripping causes its mass to fall below the resolution limit of the simulation (Ghigna et al. 2000; De Lucia et al. 2004; Gao et al. 2004). When this happens, we estimate a survival time ($t_{\rm merge}$) for the associated galaxy using its current orbit and the classical dynamical friction formula of Binney & Tremaine (1987). Once this time has elapsed, the galaxy is assumed to merge onto the central galaxy of its current halo. While it still survives it is assumed to follow the particle which was the most bound particle of the subhalo at the last time it was identified. De Lucia & Blaizot (2007) found that increasing the merging time by a factor of 2 slightly improves the fit to observed luminosity function. Such an increase has other effects which De Lucia & Blaizot (2007) did not study, for example, it increases the amplitude of small-scale galaxy correlations by about a factor of 2 at $r < 100$ kpc. Others authors have claimed that this

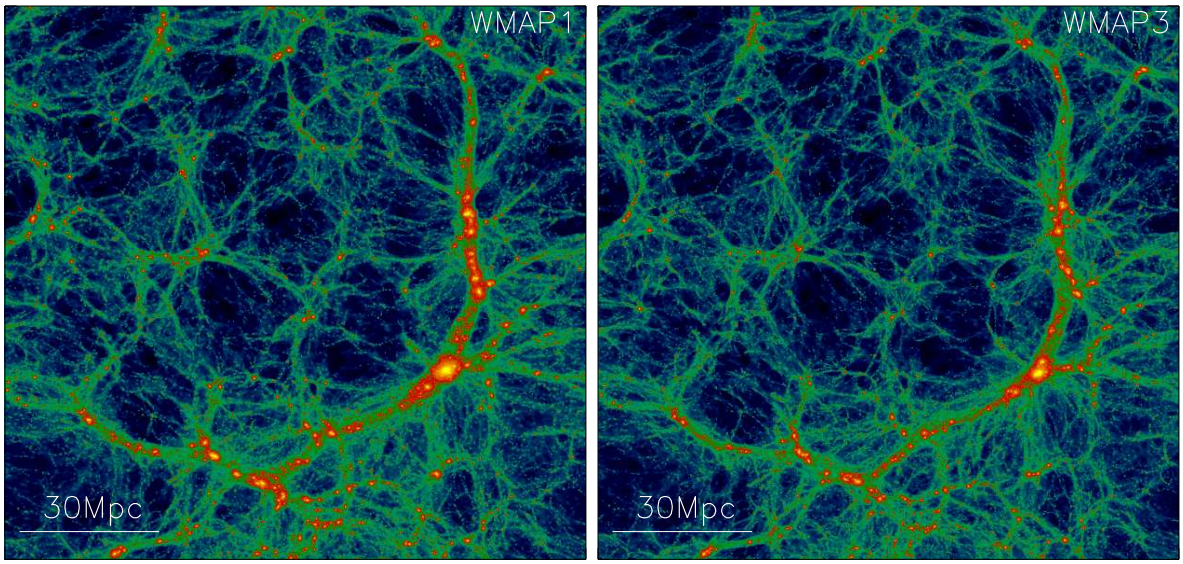

Figure 4.2: Redshift zero distribution of dark matter within a slice of thickness $20\,\mathrm{Mpc}\,h^{-1}$ through our two simulations, WMAP1 (left) and WMAP3 (right).

merging time should be effectively set to zero, so that such "orphan" galaxies lose their identity at the same time as their subhaloes (Conroy et al. 2007). Here we leave this issue for detailed study in future work and simply consider the pre-factor to be used for t_{merge} as a free parameter.

4.4 Formation of dark matter structures

Figure 4.2 shows the dark matter distribution at $z = 0$ within a slice $20\,\mathrm{Mpc}\,h^{-1}$ thick cut from the full volume of our simulations. The WMAP1 model is on the left and the WMAP3 model on the right. The projection is colour-coded by density and provides a visual illustration of the delay of structure formation in the lower σ_8 model. Although the overall structure is very similar, it is clear that massive haloes lying at the nodes of the cosmic web are in a more advanced stage of merging in the WMAP1 case than in the WMAP3 case.

The differing fluctuation amplitudes of the two simulations translate into a systematic difference between their halo mass functions. This is illustrated in Fig. 4.3 where we compare the cumulative number density of halos for the two cases (blue for WMAP1, red for WMAP3). In addition, we show the corresponding function for the much larger Millennium Simulation (green) which used our WMAP1 cosmological parameters. It agrees very well with the smaller WMAP1 simulation of this paper. At $z = 0$, the most massive haloes in our WMAP3 simulation are about 1.5 times less massive than their counterparts in the WMAP1 simulation. The number of haloes more massive than $10^{13}\,\mathrm{M}_{\odot}\,h^{-1}$ is ~ 25 per cent smaller in the WMAP3 case than in the WMAP1 case. These differences increase

at higher redshift. At $z \sim 6$ (i.e. at the end of the reionization epoch) the most massive haloes in the two simulations differ by about a factor of 5 in mass.

We recall that the main differences between the cosmological parameters used in the two simulations are the lower value of σ_8 and the redder primordial power spectrum index n in the WMAP3 case. As shown in Fig. 4.1, these combine to produce a substantial suppression of small-scale power. This has important implications for the formation of the first objects and for the star formation history at early times. Gao et al. (2007) studied this problem using high-resolution cosmological simulations with a smoothed particle hydrodynamics treatment of baryonic processes. They found a much lower abundance of potentially star-forming halos at high redshift for WMAP3 than for WMAP1. This reduction in the number of 'mini-haloes' at $z \sim 10$ was also discussed by Reed et al. (2007) using analytic models to explore the dependence on cosmological parameters. For fluctuation amplitudes at the WMAP1 level, very efficient production of UV radiation is needed to reionize the intergalactic medium by $z \sim 15$, as required by the WMAP1 value for the electron scattering optical depth τ (e.g. Ciardi et al. 2003). Interestingly, the delay in structure formation in a WMAP3 Universe is such that *equally* efficient UV production is needed to reionize by $z \sim 10$, as inferred from the WMAP3 value of τ (Alvarez et al. 2006).

Fig. 4.4 shows $z = 0$ autocorrelation functions in our WMAP1 and WMAP3 simulations for the dark matter (in the top panel) and for all dark matter substructures identified by SUBFIND (in the bottom panel; this corresponds to all self-bound (sub)haloes with more than 20 simulation particles). The difference in fluctuation amplitude causes the correlation strength to be almost a factor of two smaller in the WMAP3 case than in the WMAP1 case on scales below a few Mpc. Curiously, however, this decrease is almost completely compensated by an increase in the (sub)halo bias, so that the 2-point correlation functions for subhaloes are almost identical in the two cases. There is a slight residual offset on scales $0.5\,\mathrm{Mpc}h^{-1} \lesssim r \lesssim 5\,\mathrm{Mpc}h^{-1}$. As we will see below, this results in very similar galaxy correlation functions being predicted in the two cases.

4.5 Galaxy Formation

In this section we analyse galaxy populations simulated using the semi-analytic framework presented in Sec. 4.3. Table 4.3 lists the combinations of semi-analytic parameters for which we will show detailed results. Model A is the parameter set used by De Lucia & Blaizot (2007) for the Millennium Simulation. As expected, this also gives good agreement with observation for our WMAP1 simulation. Models B and C are parameter combinations that, as we show below, produce a similar agreement with local data for the WMAP3 cosmology.

Model B has the same star formation efficiency as model A (α_{SF}), but lower supernova feedback efficiency (ϵ_{halo} and ϵ_{disk}), and lower AGN feedback efficiency (κ_{AGN}). For this model, we have also eliminated the pre-factor of 2 which De Lucia & Blaizot (2007) introduced in the definition of the merging time. In contrast, in model C, we double the star formation efficiency (relative to model A) in order to compensate for the delay in structure formation, but this must be compensated by much higher feedback efficiencies (both from supernovae and from AGN) to prevent the overproduction of stars at late times. For this model we keep the pre-factor of 2 in the definition of the merging times of satellite galax-

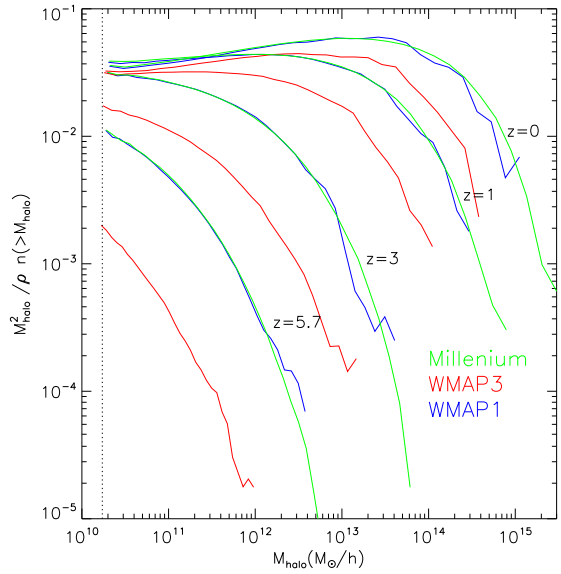

Figure 4.3: Cumulative halo number density as a function of halo mass and redshift. Results for the WMAP3 and WMAP1 simulations are represented by red and blue curves respectively. Results for the Millennium Simulation are shown in green. The halo abundance is multiplied by M^2 in order to reduce the dynamic range of the ordinate.

Table 4.3: Principal parameters of our galaxy formation models (see text for details).

	A	*B*	*C*
$\alpha_{\rm SF}$	0.03	0.03	0.07
$\epsilon_{\rm halo}$	0.35	0.2	0.28
$\epsilon_{\rm disk}$	3.5	3	4.5
$\kappa_{\rm AGN}$	7.5e-6	6.5e-6	1.2e-5
$f_{\rm BH}$	0.03	0.03	0.05
$t_{\rm merge}$	$2 \times t_{\rm friction}$	$t_{\rm friction}$	$2 \times t_{\rm friction}$
Best for	WMAP1	WMAP3	WMAP3

ies. We also increase the efficiency of accretion onto black holes during mergers (which increases the effectiveness of the 'radio' mode - see Eq. 6). In the following, we will show that models B and C give similar $z = 0$ results for the WMAP3 cosmology, and that these resemble the results of model A for the WMAP1 simulation. This shows that there are at least two independent way to 'compensate' for the delay in the structure formation within this physical framework: we can decrease feedback on all scales while keeping the same star formation efficiency (model B), or we can increase both the star formation efficiency and the feedback efficiency on all scales (model C).

In the following sections we discuss how the predictions of our three models compare to

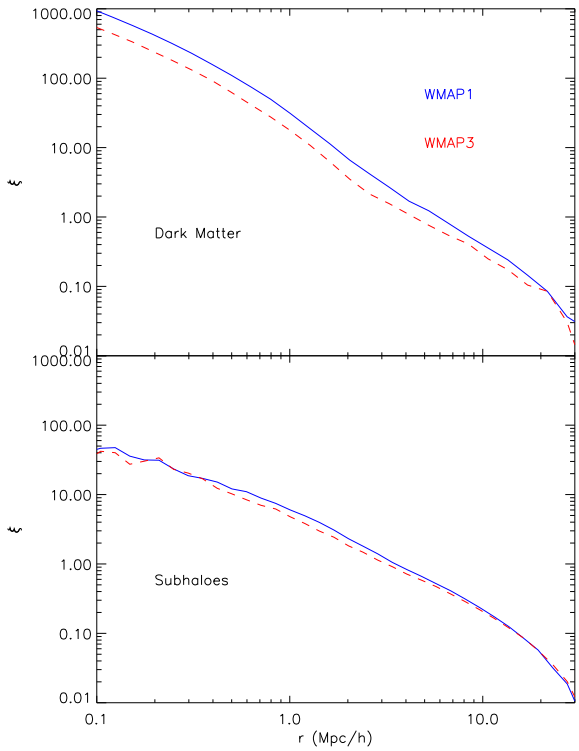

Figure 4.4: Autocorrelation functions at $z = 0$ for dark matter (top panel) and for all subhaloes with at least 20 particles (bottom panel). Blue solid and red dashed curves show results for our WMAP1 and WMAP3 simulations respectively.

observational data both in the local Universe and at high redshift.

4.5.1 Low-redshift Luminosity Functions

Figure 4.5 compares observational estimates of the K-band luminosity function of nearby galaxies to predictions from our three galaxy formation models (differentiated by colour) applied to each of our two simulations (differentiated by line type). In both cosmologies models B and C give almost identical results, while model A predicts fewer galaxies at bright luminosities ($M_{\rm K} < -22$) by a factor that varies from 1.3 to 3. The inset in Fig. 4.5 repeats the figure showing only results from model A applied to our WMAP1 simulation and from models B and C applied to our WMAP3 simulation. This shows all three models to produce similarly good fits to the observations around and above the 'knee'. All three models show an excess of galaxies fainter than $\mathrm{M_K} - 5\log h \sim -22$ with respect to the Cole et al. (2001) data, although they lie below the luminosity function given by Huang et al. (2003). This possible excess is more pronounced in model A. In the following we will only discuss results from our 'best' models (i.e. model A for our WMAP1 simulation and for the Millennium Simulation, models B and C for our WMAP3 simulation; in the following we denote these

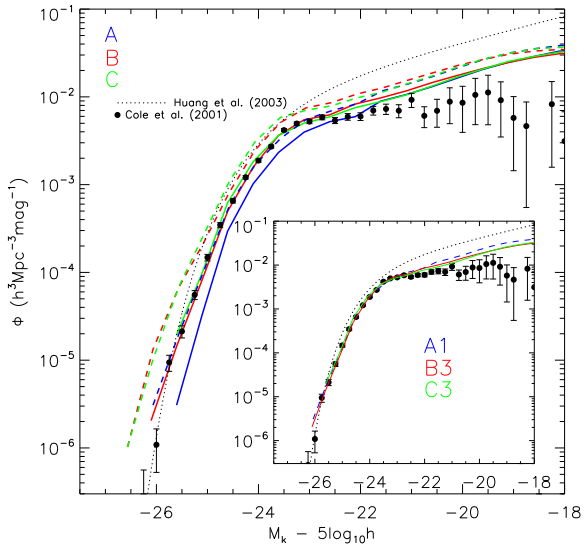

Figure 4.5: K-band luminosity function for the three galaxy formation models and the two cosmologies simulated in this study. Results from models A, B, and C are shown in blue, red and green respectively. Solid and dashed lines correspond to our WMAP3 and WMAP1 simulations respectively. The black symbols with error bars show the observational determination by Cole et al. (2001), while the black dotted curve shows the measurements of Huang et al. (2003). The inset repeats the figure but shows results only from model A applied to WMAP1 and from models B and C applied to WMAP3.

as A1, MSA, B3 and C3).

Figure 4.6 compares model galaxy luminosity functions in the Sloan Digital Sky Survey (SDSS) r-band to observational measurements from the SDSS itself. Here the observational uncertainties are much smaller than for the K-band luminosity function of Fig. 4.5. Since the observed absolute magnitudes quoted by Blanton & et al. (2003) are band-shifted to $z = 0.1$, we also correct our simulated r-band absolute magnitude to this redshift using their K-correction code. Fig. 4.6 shows all our "good" models to agree very well with the observational data, particularly around the knee of the luminosity function ($-22 < M_r < -19$). All models overpredict the abundance of faint galaxies, although the problem appears significantly less dramatic here than in Fig. 4.5. In all models the rarest and most luminous galaxies are also too bright by 0.2 to 0.6 magnitudes. This problem may be ,at least partially, due to our assigning light to these objects which should be part of the intracluster light of the groups or clusters of which they are the central galaxies (see also Conroy et al. (2007)).

4.5.2 The Tully-Fisher Relation

In Fig. 4.7, we compare the Tully-Fisher relation for our model galaxies to the observational determination by Giovanelli et al. (1997). Green symbols show all model central galaxies

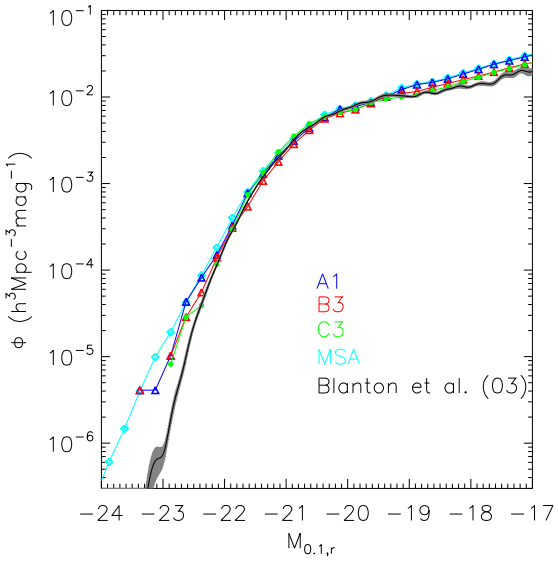

Figure 4.6: Galaxy luminosity function at SDSS $r_{0.1}$ band. Coloured lines show predictions from the three "good" models of this paper. We also plot results from model A applied to the Millennium Simulation. The black curve with an error band corresponds to the observational measurement from Blanton & et al. (2003).

with $1.5 < M_{B,\mathrm{bulge}} - M_{B,\mathrm{total}} < 2.6$ where $M_{B,\mathrm{bulge}}$ and $M_{B,\mathrm{total}}$ are the absolute magnitude of the bulge and the total B-band magnitude, respectively. This selection is made in order to isolate Sb/c spirals as in the observed sample of Giovanelli et al. (1997). The mean observational relation is shown by a solid blue line in the figure, with the corresponding 1σ scatter indicated by the dashed lines. The relation of Giovanelli et al. is already corrected for internal extinction. We therefore do not include dust effects when predicting I–band magnitudes for this plot. Red lines in each panel show a linear fit to the model results. The top panel of Fig. 4.7 demonstrates that model A1 reproduces both the slope and the zero-point of the observed relation (as also shown in Croton & et. al 2006). Models B3 and C3 exhibit a substantially brighter zero-point than observed. This occurs because fitting the observed luminosity function within the less evolved halo mass function of the WMAP3 cosmology (see Fig. 2) requires us to put galaxies of given luminosity at the centre of lower mass halos than in the WMAP1 case.

Finding theoretical models which simultaneously fit both the observed luminosity functions and the observed Tully-Fisher relation has always been difficult(e.g. Cole et al. 2000). The results in Fig. 4.7 show that this remains true. Note, however, that it is uncertain how best to extract quantities from our models for comparison with the observational data. For example, we assume here that W (the measured HI linewidth) is twice the maximum circular velocity of the galaxy's dark halo, as measured directly from the simulation and without any correction for the effects of the baryonic mass of the galaxy. This is a rough assumption which may be systematically in error. In particular, if galaxy formation results

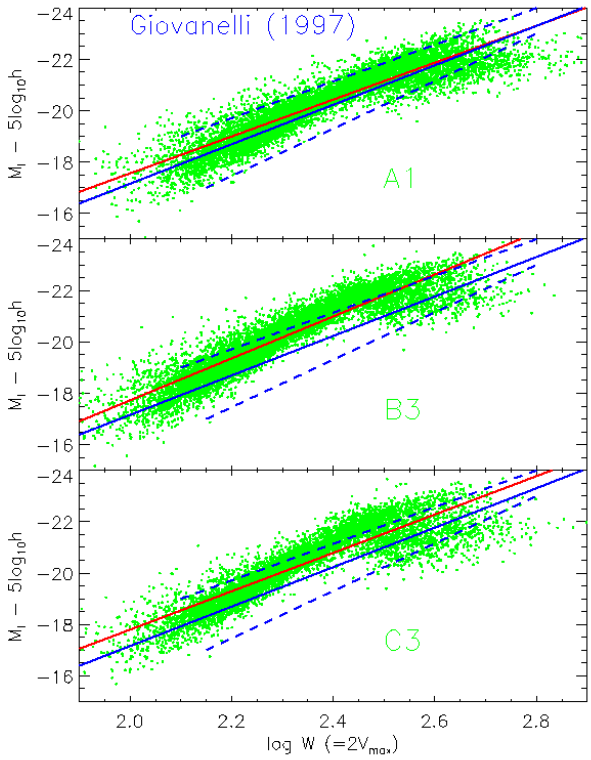

Figure 4.7: Tully-Fisher relation for spiral galaxies in our three models. We show only central galaxies with $1.5 < M_{B,\mathrm{bulge}} - M_{B,\mathrm{total}} < 2.6$, and we approximate the observed HI linewidth by twice V_{max} for the dark halo, as measured directly in our simulations. Red lines are linear fits to the model results. The blue solid line shows the mean observational relation by Giovanelli et al. (1997), with blue dashed lines indicating the scatter in this relation.

in a maximum disk rotation velocity which is significantly and systematically above this value, the population of galaxies in our WMAP3 model could be reconciled with the observations. Changing the transformation between these two velocities can change the slope and zero-point, or introduce curvature into the model Tully-Fisher relation. Semi-analytic models provide robust estimates for the locations, velocities and global properties (luminosity, colour, stellar mass, etc,) of galaxies, but become less reliable when quantities (such as W) which depend sensitively on the internal structure of the galaxies must be predicted (see also the discussion in Somerville & Primack 1999).

4.5.3 Mass-to-Light Ratios of Clusters

In Fig. 4.8, we plot SDSS $r_{0.1}$ band mass-to-light ratios ($M/L_{r,0.1}$) for individual clusters with $M \geq 10^{14} M_{\odot}$ (symbols) and the running median value over the full resolved mass range (solid lines). Both M and $L_{r,0.1}$ are computed within R_{200}, defined as the radius

within which the mean mass overdensity is 200 times the critical value. Blue, red and green are used for models A1, B3, and C3 respectively. Cyan is used for the model MSA which provides a larger number of clusters than the smaller simulations used in our study. The black horizontal line and hatched area show the region occupied by the observational data in Carlberg et al. (1996,see Tinker et al. 2005 for details on the conversion to the SDSS $r_{0.1}$ band). Our models exhibit a very weak mass dependence over the observed mass range and agree reasonably well with the observational measurements. The differences between the two cosmological models, and between the two galaxy formation models for same WMAP3 cosmology are small, even at small masses where van den Bosch et al. (2007) found a more pronounced decrease in the mass-to-light ratio for WMAP3 cosmology with respect to WMAP1.

It is interesting to compare our results with those based on halo occupation distribution (HOD) models. van den Bosch et al. (2003) found that their conditional luminosity function (CLF) model was unable to fit the observed mass-to-light ratios of clusters in a cosmology with WMAP1 parameters, and they argued strongly in favour of a cosmology with a lower value of σ_8, similar to that subsequently preferred by WMAP3. Once their models are constrained to fit the observed luminosity and correlation functions of galaxies, they find $\langle M/L \rangle$ to vary roughly as σ_8^2 on cluster scales. Tinker et al. (2005) found a similarly strong dependence of the mass-to-light ratio on σ_8 using an HOD model which differed in detail and which they constrained with different observational data. M/L predictions from these models are shown in Fig. 4.8 by the horizontal dashed and dotted lines (blue and red are used for WMAP1 and WMAP3 respectively). Predictions from van den Bosch et al. (2003) were obtained by converting their B-band estimates to the SDSS $r_{0.1}$ band using the conversion factor adopted in Tinker et al. (2005). These authors convert the mean B-band mass-to-light ratio $< M/L_B >= 363h(M/L)_\odot$ of Carlberg et al. (1996) to $< M/L_{r,0.1} >= 359h(M/L)_\odot$ in the SDSS $r_{0.1}$ band. Thus we multiply the results of van den Bosch et al. (2003) by a factor of $359/363 = 0.988$. Fig. 4.8 shows that the mass-to-light ratio dependence on σ_8 in our models is much weaker than in the two HOD models mentioned above. This is surprising since our models are also a good fit to the observed galaxy luminosity functions, and fit observed correlation functions moderately well, at least on large scale (see below).

In Fig. 4.8, we also show as a black solid line the average mass-to-light ratio predicted by the physically based HOD model presented in Wang et al. (2006). These authors use the same positions and velocities for galaxies as our semi-analytic model (taken directly from the Millennium Simulation) but adopt simple parametrized functions to relate the star formation rates of galaxies to the mass and location (satellite or central) of their parent subhalo. The parameters of these functions are then minimized in order to optimize the fit to the observed luminosity function and luminosity-dependent correlation functions. The cluster mass-to-light ratios predicted by this model are higher than those in any of the semi-analytic models in our study, and are reasonably close to the predictions of van den Bosch et al. (2003) and Tinker et al. (2005) for a WMAP1 cosmology (the cosmology adopted in the Millennium Simulation). Comparing the model of Wang et al. (2006) in detail to the MSA model, we find that the larger mass-to-light ratio on cluster scales is due to systematic lower central galaxy luminosities (by a factor ~ 2) in the HOD model. We note that De Lucia & Blaizot (2007) found reasonable agreement when compar-

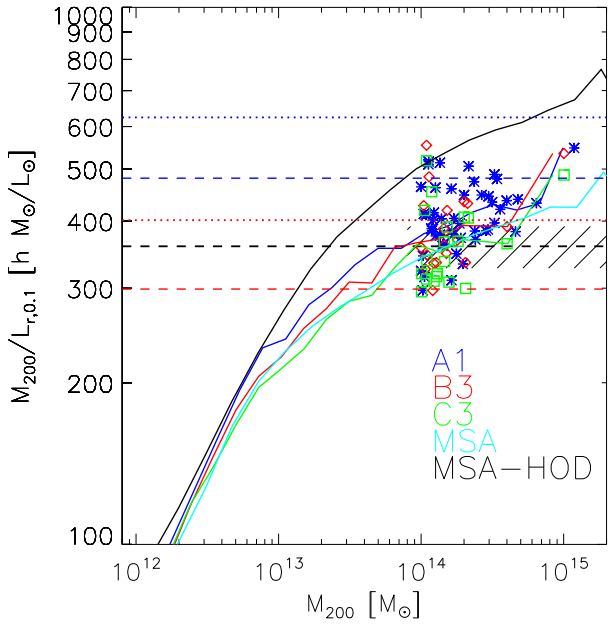

Figure 4.8: Mass-to-light ratios in the SDSS $r_{0.1}$ band as a function of halo mass. Symbols show results for the 48 (20) clusters with mass $M > 10^{14} M_\odot$ in our WMAP1 (WMAP3) simulation. Solid lines show a running median over a wider range of halo masses. Blue, red, green and cyan are used for models A1, B3, C3 and MSA respectively. The black solid curve refers to the HOD model of Wang et al. (2006) applied to the Millennium Simulation (MSA-HOD). The black dashed line and the hatched area show the region occupied by the observational data of Carlberg et al. (1996). The horizontal dotted and dashed lines show predictions for M/L of clusters $M > 10^{14} M_\odot$ from van den Bosch et al. (2003) and Tinker et al. (2005) respectively. In each case blue refers to the WMAP1 and red to the WMAP3 prediction.

ing this same MSA model to the observed K-band magnitudes of brightest cluster galaxies (BCGs). We note also that precise measurements of BCGs luminosities are complicated by the intrinsic difficulty in separating the contribution of the cD envelope (Schombert 1988; Gonzalez et al. 2005; Zibetti et al. 2005). The three HOD models shown in Fig. 4.8 exhibit a stronger dependence on cosmology (in particular σ_8), but also a larger dependence on modelling details than do our semi-analytic models. It seems, therefore, that a good understanding of the consequences of modelling assumptions is needed before firm conclusions can be drawn about σ_8 or other cosmological parameters.

4.5.4 Pairwise Velocity Dispersion

Pairwise velocity dispersions (PVD) are a useful tool because of their strong sensitivity to the abundance of massive haloes (Mo et al. 1993; Jing & Börner 2004; Yang et al. 2004; Tinker et al. 2006). Fig. 4.3 shows that the present-day abundance of massive haloes with

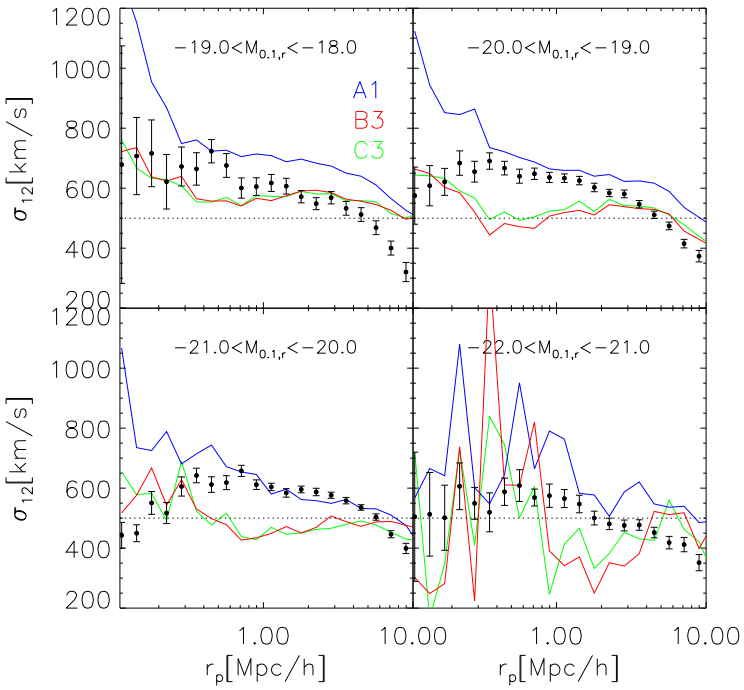

Figure 4.9: Pairwise velocity dispersions for our three SA models and for four luminosity bins in the SDSS $r_{0.1}$ band. Results from our three models are presented in blue (A1), red (B3) and green (C3). The black symbols with error bars are observational data from (Li et al. 2007). The horizonal dotted line corresponds to the $\sigma_{12} = 500$km/s

.

mass $\geq 10^{14} M_{\odot}/h$ in WMAP3 is almost 2.5 times lower than the corresponding abundance in WMAP1. This should be reflected in differences in the predicted PVD.

In Fig. 4.9, we present the dependence of PVD on SDSS $r_{0.1}$ luminosity for the three SA models used in this work. The black points with error bars show observational estimates from Li et al. (2007) obtained by modelling the full two-dimensional redshift-space correlations. In order to compare our model prediction with these data, we adopt the assumptions and modelling methods of Jing et al. (1998); Li et al. (2007) except that rather than constructing large mock catalogues, we measure directly both the 2-dimensional correlation function in redshift space ($\xi(r_p, \pi)$) and the real space correlation ($\xi(r)$) using the distant observer approximation for the former. Fig. 4.9 shows that model A1 produces higher dispersions (by $\sim 50 - 150$km/s) on all scales and for all luminosity subsamples than do the two WMAP3 models. Except for the faintest galaxies, model A1 also gives a better fit to the observational data. This agrees with Li et al. (2007) who compared their measurements to the model of Croton & et. al (2006) which is very similar to our A1. Both WMAP3 models predict lower PVD than are observed, and they also seem to show a different slope. Thus, PVD observations seem to prefer a WMAP1 cosmology, as can be inferred from Jing & Börner (2004).

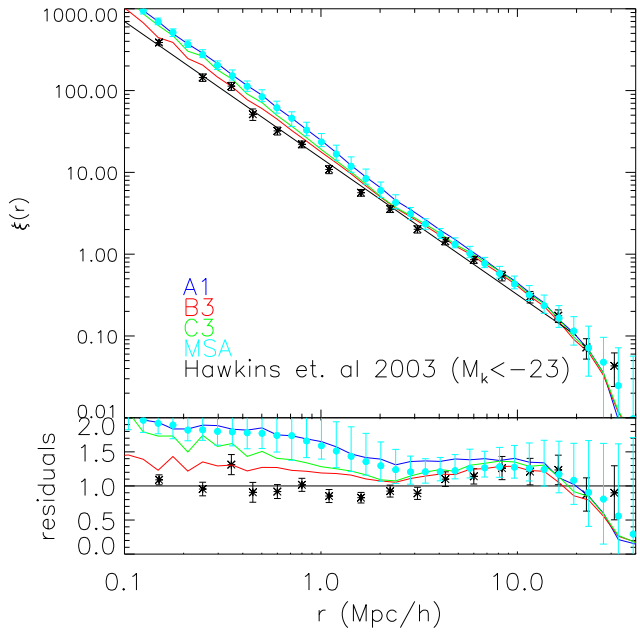

Figure 4.10: 2-point autocorrelation functions for luminous galaxies in K-band at $z = 0$. Solid colored curves show results for the three "good" models of this paper. The cyan symbols with error bars are predictions based on 64 small boxes (each with the volume of the simulations of this paper) cut from the Millennium Simulation catalogue of De Lucia & Blaizot (2007). Black symbols with error bars and the black solid line show observational estimates and a power law fit from the 2DFGRS(Hawkins et al. 2003). The residuals shown in the lower panel are calculated with respect to this power law fit.

4.5.5 Galaxy Clustering

Figure 4.10 compares the 2-point correlation function of our model galaxies at redshift $z = 0$ to a recent measurement from the 2dFGRS (Hawkins et al. 2003). Solid colored lines show predictions from our three "good" models (blue for model A1, red and green for models B3 and C3 respectively). For each model there are about 17000 galaxies with $M_{\rm k} < -23$. This magnitude limit is just fainter than the knee in Fig. 4.5 so that most luminous galaxies are included. In order to estimate the cosmic variance in these estimates, we divide the *Millennium Simulation* galaxy catalogue of De Lucia & Blaizot (2007) into 64 small boxes, each with the same volume as our new simulations, and then calculate the mean and scatter of the resulting 64 autocorrelation estimates. (We have taken care to eliminate edge effects when calculating correlations for galaxies within these subvolumes.) Cyan symbols show the mean calculated in this way, while the error bars give the 10% to 90% range. Our models were not tuned to match observational measures of galaxy clustering, so the overall agreement with observations demonstrated by Fig. 4.10 is encouraging.

We can also see that results from the three models converge on large scales ($\gtrsim 6h^{-1}$Mpc). On intermediate scales ($6h^{-1}\text{Mpc} \gtrsim r \gtrsim 1h^{-1}\text{Mpc}$), models B3 and C3 exhibit weaker

clustering than model A1, agreeing better with the observational estimates. Interestingly, the 2-point correlation function of subhaloes (see Fig. 4.4) shows a similar offset between the models on these scales. On smaller scales ($r < 1h^{-1}$Mpc) the three models give different results – B3 agrees with the observational data to within the scatter found among the 64 Millennium samples, while C3 is marginally high and A1 is significantly high. Clearly clustering on these scales is quite sensitive to details of the galaxy formation physics.

It is also interesting that model A1 is significantly high compared to the mean of the Millennium results on scales between 2 and $8h^{-1}$Mpc, even though the two simulations adopt the same galaxy formation physics within the same cosmology. This suggests that the particular realisation of a $L = 125h^{-1}$Mpc box used in this paper overestimates clustering on these scales. Correcting for this would bring models B3 and C3 into excellent agreement with the observations for $r > 2h^{-1}$Mpc. In summary, all three models agree well with the data on the large scales that are sensitive to 2-halo correlations. Model B3 also agrees well with observation on smaller scales which are dominated by galaxy pairs within a common halo. C3 is slightly high on these scales and A1 is too high to be compatible with the observational data. We note, however, that there is a significant difference between B3 and C3 which are implemented on the same WMAP3 simulation. This emphasizes that small-scale galaxy correlations are very sensitive to details of the adopted galaxy formation physics and are unlikely to be useful for constraining cosmological parameters.

In Fig. 4.11 we study how galaxy correlations vary with luminosity, comparing the projected autocorrelations $w(r_\mathrm{p})$ from our models (solid coloured lines) with observational data from the SDSS (Li et al. 2006) (symbols with error bars). Results are shown for six magnitude bins from faint (top left) to bright (bottom right). Below each panel, we also show the ratio between the model and the observed estimates. The model projected correlation function has been determined by integrating the real space correlation function ($\xi(r)$) along the line-of-sight:

$$w(r_\mathrm{p}) = 2 \int_0^\infty \xi(\sqrt{r_\mathrm{p}^2 + r_{||}^2}) dr_{||} = 2 \int_{r_\mathrm{p}}^\infty \xi(r) \frac{r\ dr}{\sqrt{r^2 - r_\mathrm{p}^2}} \tag{4.7}$$

We note that if the integration is truncated at $r = 60\mathrm{Mpc}/h$ (half the box size of our simulations) the resulting projected correlation function is reliable up to $\sim 10\mathrm{Mpc}/h$. Because of the limited volume of our simulations, the two brightest magnitude bins contain only a few thousand and a few hundred galaxies respectively. Results for the fainter bins are based on much larger numbers of galaxies. The straight black line reproduced in each panel to facilitate comparison corresponds to the power-law:

$$\xi = (r/5\,\mathrm{Mpc}\,h^{-1})^{-1.8}$$

The results in this figure show reasonably good agreement between the models and the observations for $M_r < -20$, but significant overpredictions, particularly for model A1, at fainter absolute magnitudes and at large scales. The differences between model and observation show similar trends with pair separation for all the models, and are as large as the differences between the models themselves. On the basis of this comparison none of the models is obviously better or worse than the others. In particular, at bright magnitudes

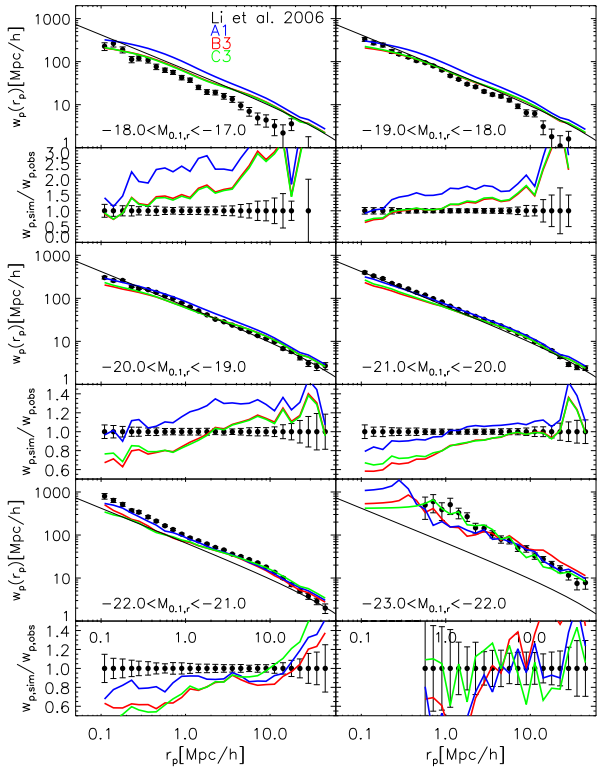

Figure 4.11: Projected correlation function $w_{\rm p}$ in the SDSS $r_{0.1}$ band. Coloured lines show results for our simulated galaxy catalogues. Black points are for the SDSS data (Li et al. 2006). Each pair of panels corresponds to a different absolute magnitude bin. The solid black line in the upper panel of each pair corresponds to the power-law: $\xi = (r/5\,{\rm Mpc}\,h^{-1})^{-1.8}$. The lower panel of each pair plots the ratio of model to observation, with error bars to indicate the uncertainty in the observational estimate.

($M_r < -20$) model A1 is a significantly better fit to the observations than either B3 or C3. This reproduce the trends which Li et al. (2007) found in their own comparison of SDSS correlation to the Millennium Simulation catalogue of Croton & et. al (2006). This is the exact opposite of the conclusion drawn above from Fig. 4.10, suggesting that the level of agreement between different observational estimates of galaxy correlations is not yet good enough to distinguish between the various models we are discussing.

4.5.6 Evolution to high redshift

Figure 4.12 shows how results from our models compare to the observed cosmic star formation rate density as a function of redshift. Symbols with error bars are a compilation of observational data taken from Fig. 12 of Springel & Hernquist (2003). Models B3 and C3 have quite similar star formation histories, although C3 lies above B3 by about 15 per cent at $z > 2$. This is due to the higher star formation efficiency used in model C. Model

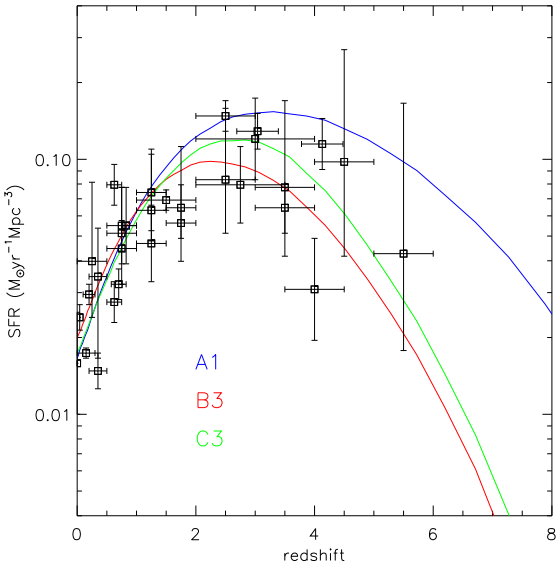

Figure 4.12: Cosmic star formation rate density as a function of redshift. Symbols with error bars are a compilation of observational data (taken from Fig. 12 of Springel & Hernquist 2003). The solid coloured curves show results from our 'best' models (see text for details).

A1 provides much larger star formation rates than either B3 or C3 for $z > 1$ and lower star formation rates in the local Universe. The high redshift difference reflects the earlier formation of structure in the WMAP1 cosmology, while the difference at late times is a consequence of the requirement that all models produce the same total number of stars (as measured by the K-band luminosity function) in the present universe.

The most dramatic difference in Fig. 4.12 is that between the two cosmologies at the highest redshifts. For $z \sim 6$, the star formation rates are almost an order of magnitude lower in models B3 and C3 than in model A1. A related result, also visible in Fig. 4.12, is that the peak of the cosmic star formation history is shifted to lower redshift in the new cosmology: from $z \sim 3$ in model A1 to $z \sim 2$ in model B3 or to $z \sim 2.5$ in model C3. Fig. 4.12 suggests that measurements of the cosmic star formation rate at high redshift can potentially constrain models like those discussed here. Unfortunately, observational uncertainties (e.g. due to the use of different star formation estimators at different redshifts, and to the need for substantial dust corrections) are too large to discriminate reliably between our three models. In addition, these models are far from exhausting all physically plausible possibilities for the phenomenology of star formation and feedback, so the true theoretical uncertainty is undoubtedly larger than suggested by Fig. 4.12.

In a recent paper Kitzbichler & White (2007) compared results from the model discussed in De Lucia & Blaizot (2007) to a variety of observational data at high redshift. They found this model (which is identical to our model A) to give moderately good agreement with the observed luminosity and stellar mass functions of galaxies over a large redshift range. As

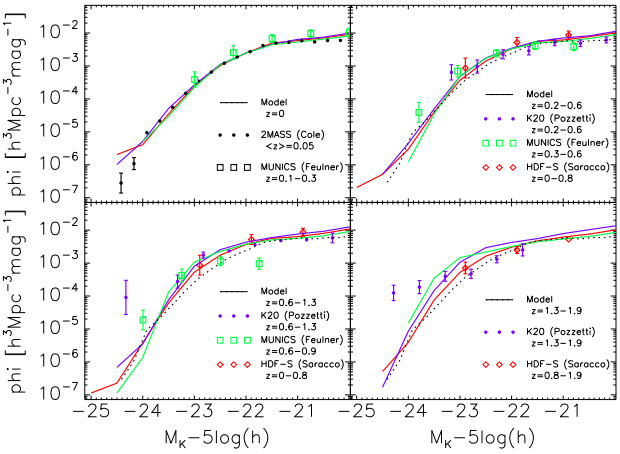

Figure 4.13: Rest-frame K-band luminosity functions for different redshift intervals. Model results are shown as solid lines (blue for A1, red for B3, and green for C3). Symbols with error bars show observational estimates from several surveys, as labelled in each panel. The low-redshift observational determinations of Cole et al. (2001) is repeated as a dotted black line in the other panels.

shown in Fig. 4.12, the three models used in the present study have a significantly different behaviour at high redshift, so it is interesting to see if the observations can discriminate between them.

Our figures 4.13 and 4.14 correspond to figures 5 and 7 of Kitzbichler & White (2007) and show evolution with redshift of the rest-frame K-band luminosity function, and of the stellar mass function respectively. In Fig. 4.13, symbols with error bars show observational determinations from Cole et al. (2001); Pozzetti et al. (2003); Feulner et al. (2003); Saracco et al. (2006). The observational estimate in the local Universe from Cole et al. (2001) is repeated in the other panels as a black dashed line. Model results are shown as solid coloured lines (blue for A1, red for B3 and green for C3). Fig. 4.13 already showed all three models to agree nicely with local observations. At higher redshifts, the agreement is also reasonably good. All three seem to underpredict the number of luminous galaxies in the highest redshift bin, but it should be kept in mind that the rest-frame K-band luminosities here have been extrapolated beyond the directly observed region, and so are quite uncertain (see the discussion in Kitzbichler & White 2007). Our three models start to show significant differences for $z > 1$. Note that model A1 lies between models B3 and C3 in this plot so that the differences are due mainly to galaxy formation physics rather than to cosmological parameters. They are, in any case, comparable to the uncertainties in the observations, so that significantly better data are required at these redshifts to put strong constraints on our models. Finally, we note that the error bars of Fig. 4.13 underestimate the true uncertainties as they do not include the effects of cosmic variance. These are particularly important when small regions of the sky are sampled - as is the case for the data in the highest redshift bin.

Fig. 4.14 shows the evolution of the galaxy stellar mass function for our three “good”

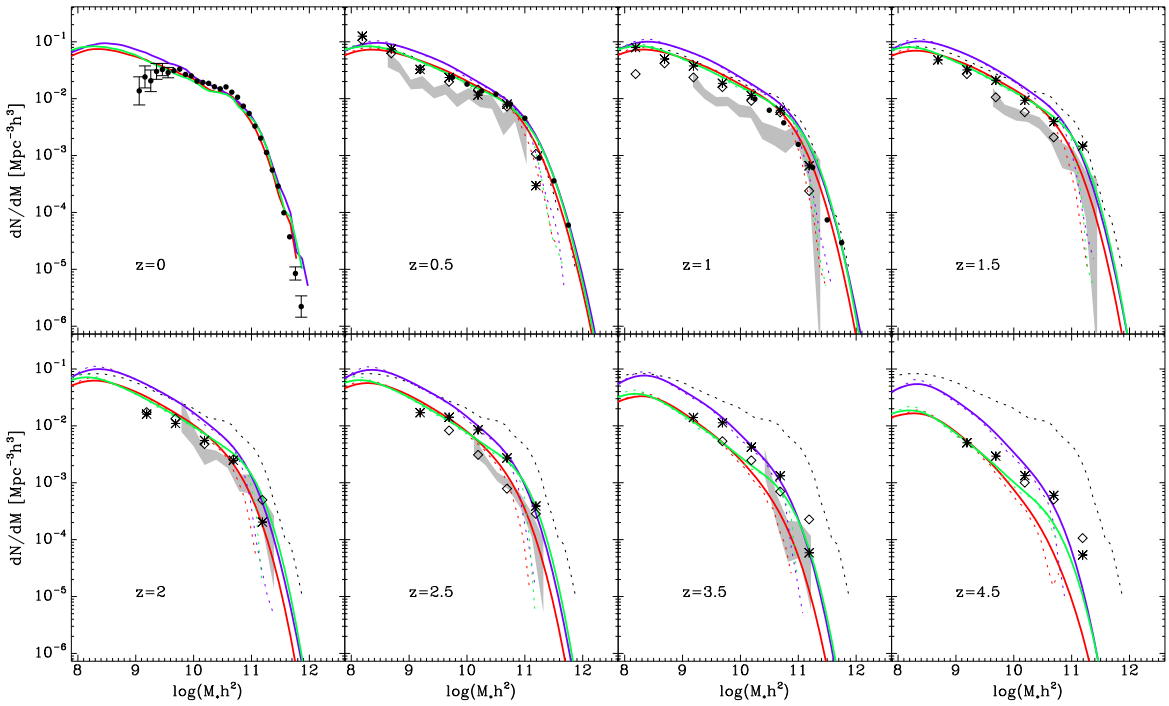

Figure 4.14: Evolution of the galaxy stellar mass function from $z = 0$ to $z = 4.5$. Model results are shown as solid lines (blue for A1, red for B3, and green for C3). Local data are from Cole et al. (2001) and are repeated as a black dashed curve in the high redshift panels. High redshift data are taken from Drory et al. (2005, symbols) and Fontana et al. (2006, grey shaded areas). Model predictions are shown both with (solid) and without (dotted) convolution with a normal distribution of standard deviation 0.25. At $z = 0$ we consider the mass determinations precise enough to neglect this effect.

models (coloured solid and dashed lines) and compares them with observational determinations from Cole et al. (2001); Drory et al. (2005); Fontana et al. (2006). As in Kitzbichler & White(2007), model results are shown both with (solid) and without (dashed) convolution with a normal distribution of standard deviation 0.25 dex, intended to represent measurement errors in $\log \mathrm{M}_*$. The dashed black line in each panel repeats the local observational estimate by Cole et al. (2001). At redshifts beyond 1, model A1 predicts substantially more galaxies in the mass range $9 < \log(M_*/M_\odot) < 10.6$ than either of the models in the WMAP3 cosmology. This remains true at higher redshift for model B3, but not for model C3. For $\log(M_*/M_\odot) > 10.8$ models A1 and C1 predict similar numbers of massive galaxies at all redshifts. The increased star formation efficiency in model C as compared to model A clearly compensates for the lower σ_8 in the WMAP3 cosmology. This demonstrates that even at high redshift it may be difficult to use galaxy data to distinguish between cosmologies unless the physics of galaxy formation can be independently constrained. Model B3 severely underpredicts the number of massive objects at $z = 4.5$, but even this disagreement may not be significant once cosmic variance and observational uncertainties are taken into

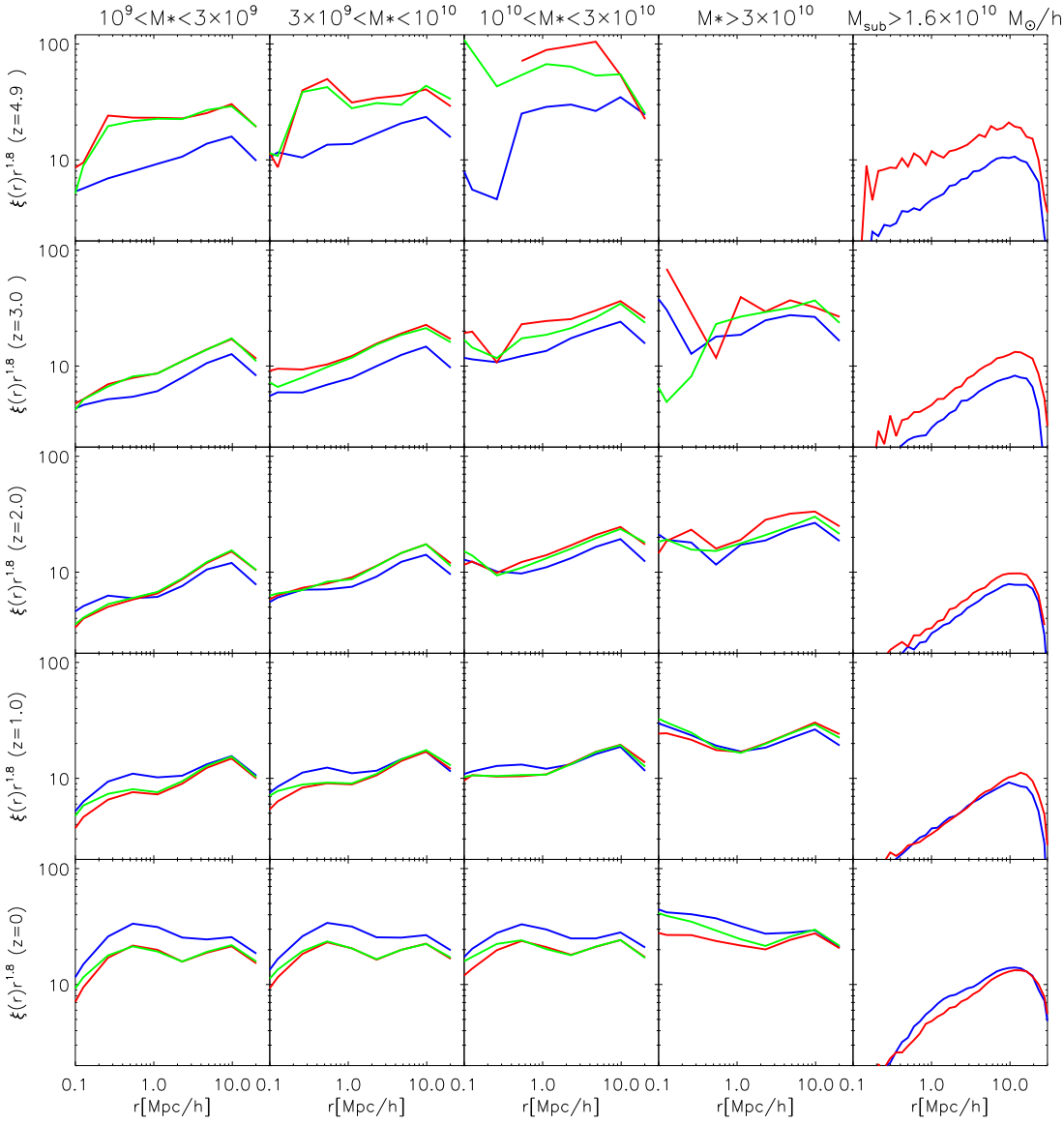

Figure 4.15: Autocorrelation functions for galaxies and for resolved subhaloes at five different redshifts ($z = 4.9; 3.0; 2.0; 1.0; 0.$). The galaxy results are given for four disjoint ranges in stellar mass, as indicated. (Stellar mass $M*$ is given in units of $M_{\odot}$.) For $M* > 3 \times 10^{10}$ there are too few galaxies at $z = 4.9$ to get meaningful results, so we leave this panel blank. Different colours in the galaxy panels refer to our different formation models, blue for A1, red for B3, and green for C3. In the subhalo column the colours refer to our two simulations, blue for WMAP1, red for WMAP3. We have multiplied all correlation functions by $r^{1.8}$ to make the differences between the models more visible. Note that r is a comoving coordinate with units of h^{-1}Mpc.

account.

Finally, we look at the evolution of clustering to high redshift. Fig. 4.15 presents spatial 2-point correlation functions at five different redshifts for all resolved subhaloes (for comparison with the lower panel of Fig. 4.4) and for galaxies in four different stellar mass bins in each of our three "good" galaxy formation models. Perhaps surprisingly, although the result of section 4.4, that the clustering of resolved subhaloes is very similar in our two cosmologies, is even more accurately true at $z = 1$, it does not hold out to high redshift. For $z > 3$, resolved subhaloes are actually substantially *more* strongly clustered in the WMAP3 cosmology than in WMAP1, despite the fact that the former has a significantly *lower* mass clustering amplitude. This effect is also visible in the galaxy autocorrelations. At the present day our models predict galaxies of all stellar masses to be somewhat more strongly clustered in the WMAP1 cosmology than in the WMAP3 cosmology. Beyond $z = 2$ the opposite is true. By $z = 5$ the effect is quite strong, more than a factor of two in correlation amplitude. These effects may seem surprising, but in fact the corresponding results for dark halos are easily obtained if standard analytic models are applied to our two cosmologies. For the convenience of the reader we provide an appendix repeating Mo & White's (2002) graphical analysis of evolution in the abundance and clustering of halos for these two cases. The large difference in the predicted galaxy clustering properties in the two cosmological model could potentially help to diagnose cosmological parameters. We note, however, that our model is not able to predict reliably high redshift galaxy populations such as Ly-α emitters, ultraluminous infrared galaxies etc. In addition, observational measurements at these redshifts are affected by systematics that are not currently well understood. A rigorous comparison between model predictions and observational measurements at these redshifts is thus still difficult.

4.6 Conclusions and Discussion

We have carried out cosmological structure formation simulations of a ΛCDM Universe for the cosmological parameter sets suggested by the first- and third-year WMAP results. The significant reduction in the best value for the amplitude of matter fluctuations on $8\,h^{-1}$ Mpc scale (σ_8) combines with the decrease in the estimate of the scalar spectral index for primordial perturbations (n), and with the lowered matter density (Ω_m) to produce a significant delay in structure formation in the WMAP3 case (see Sec. 4.4).

By coupling our numerical simulations to semi-analytic models for galaxy formation, we have investigated the implications of this delay for the observed properties of galaxies, both at low and at high redshift. Specifically, we have compared the galaxy formation model described in De Lucia & Blaizot (2007) for the WMAP1 cosmology to two galaxy formation models for the WMAP3 cosmology which use the same physical framework but different efficiency parameters. We find that both new parameter sets can compensate for the delay in structure formation to produce galaxy populations at $z = 0$ which agree with observation just as well as the old model for the WMAP1 cosmology. The luminosity functions are almost identical, the correlation functions show at most small differences, and offsets in the predicted Tully-Fisher relations are difficult to interpret because disk rotation velocities cannot be predicted reliably to the level of accuracy required.

Pairwise velocity dispersion measurements are sensitive to cluster abundance and therefore differ significantly for the two cosmological models of our study. We have shown that the two WMAP3 models underpredict the measured PVD by more than 100km/s on scales $0.3 < \mathrm{r_p} < 2$Mpc/h, and are lower than the corresponding predictions of the WMAP1 model by $50 \sim 150$km/s on all scales.

Substantial differences between the various models appear at high redshift. The delay in the structure formation translates directly into a delay in the global star formation history: at $z \sim 6$ the star formation rates in the models based on WMAP3 are lower than those based on WMAP1 by almost an order of magnitude. As discussed elsewhere, this has important implications for the formation of the first stars, and for reionization. Predictions of our three models for galaxy luminosity and mass functions at high redshift show substantial differences. Unfortunately, the uncertainties in the observed luminosities and masses, combined with large cosmic variance uncertainties, are still too large to place strong constraints on the efficiencies and scalings of the physical processes we model. Somewhat counterintuitively, we find that at high redshift galaxies of given stellar mass are predicted to be substantially more clustered in the WMAP3 cosmology than for WMAP1.

When comparing $z = 0$ correlation functions from our three models to recent observational determinations from the 2dFGRS (Hawkins et al. 2003) and the SDSS (Li et al. 2006), we found interesting and apparently significant differences between the models, particularly for galaxies fainter than ~ -20 in the SDSS r-band. At these magnitudes, our WMAP3 galaxy catalogues provide better agreement with the SDSS data but the opposite is true for galaxies around the knee of the luminosity function. It is important to realise that the reduced mass clustering amplitude implied by the WMAP3 parameters is almost entirely offset by an increase in halo bias, so that predictions for galaxy clustering change very little. At least at separations $r < 20h^{-1}$Mpc, galaxy clustering is much more sensitive to galaxy formation physics than to cosmological parameters (see also the discussion in van den Bosch et al. 2003). In fact, for almost all of the population properties we have examined, the variations induced by "acceptable" variations in the galaxy formation parameters are at least as large as those produced by the variation in cosmological parameters between WMAP1 and WMAP3. The systematic properties of galaxies and their small-scale clustering should be used to understand how galaxies form, not to constrain cosmology. A similar conclusion was reached by Kauffmann et al. (1999a) who used cruder semianalytic models to show that similar $z = 0$ clustering was predicted in two quite different cosmological models (τCDM and ΛCDM). In this case, however, the predicted evolution to high redshift was different enough to offer a clear way to distinguish the models (Kauffmann et al. 1999b).

In this paper we have shown that varying efficiency parameters within a given framework for modelling galaxy formation can lead to very similar predictions for the evolution and clustering of galaxies in the WMAP1 and WMAP3 cosmologies. The problem is sufficiently degenerate that a variety of acceptable parameter sets can be found in either cosmology. It may seem unsatisfactory to 'fine-tune' model parameters to fit the observational data, but it is interesting that substantially different efficiencies of star formation and feedback are required in the various cases. More detailed observational data on how these processes work in individual systems may therefore shed light on which parameter values are appropriate. In addition, differing efficiencies translate into significantly different predictions at high

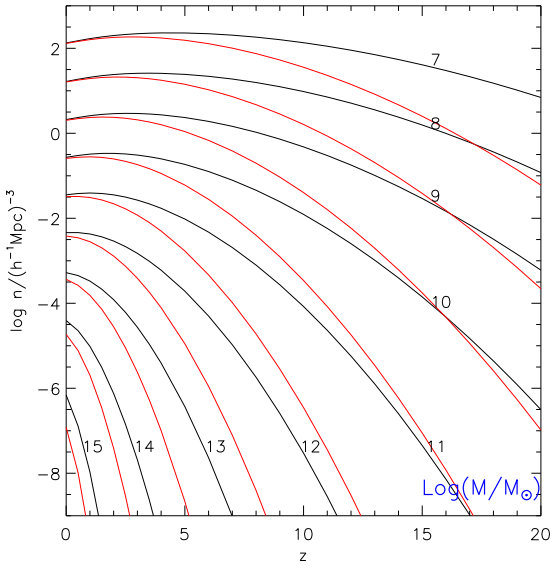

Figure 4.16: The evolution of the comoving number density of dark matter haloes with mass exceeding a specific value M in our two cosmological models: WMAP1 (black curves) and WMAP3 (red curves). The numbers labelling the black curves indicate the value of $\log(M/M_\odot)$ for the WMAP1 case. See the text for more details.

redshift. More detailed and more statistically precise observations of high-redshift galaxies will be able to distinguish between the models. Once these aspects of the galaxy formation process are better understood, it may indeed be possible to use galaxy surveys to constrain cosmological parameters.

4.7 Appendix : Halo abundance and clustering

In this appendix we use the formulae and the graphical presentation scheme of Mo & White (2002) to illustrate how the evolution of halo abundance and clustering differs between our WMAP1 and WMAP3 cosmologies. As in figures 1 and 2 of Mo & White (2002), we present plots of comoving abundance against redshift for halo samples defined by lower mass limits $M_{min}(z)$ corresponding to a variety of halo properties, in particular, for lower limits which correspond at all redshifts to a given halo mass, a given halo virial temperature, a given fraction of the total cosmic mass density, a given clusering strength in comoving units, and a given clustering stgrength at $z = 0$ for the halo descendents. We refer to Mo & White (2002) for detailed discussion of these quantities and for the relevant formulae.

Figure 4.16 corresponds to figure 1 of Mo & White (2002). Each curve gives the comoving abundance as a function of redshift of halos more massive than the value indicated by the label. Curves for our WMAP1 parameters are shown in black while curves for our WMAP3 parameters are shown in red. Labels give the decimal logarithm of halo mass in units of solar masses and are placed next to the corresponding WMAP1 curve. Curves are

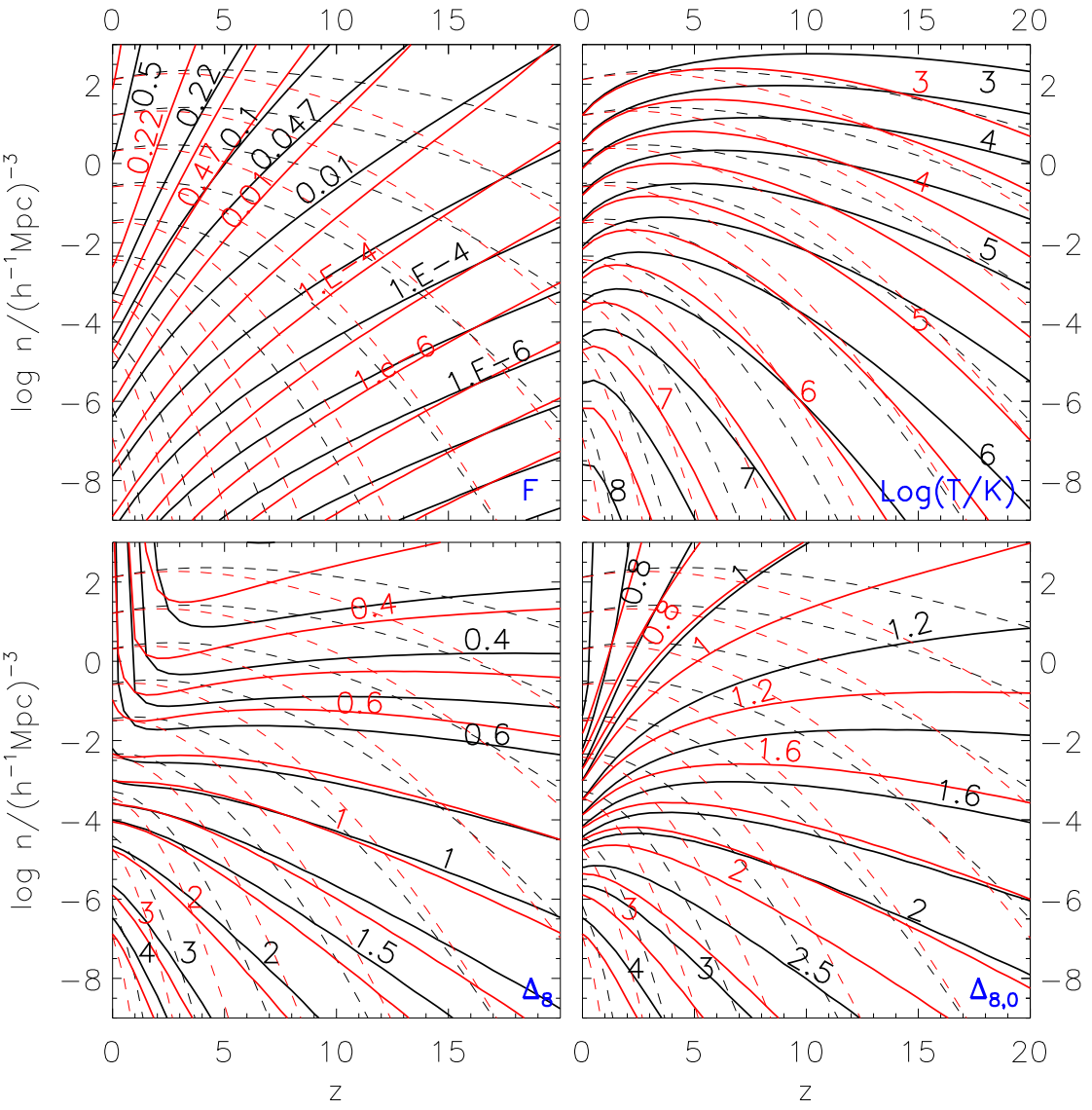

Figure 4.17: A repeat of figure 2 of Mo & White (2002) but showing results for both WMAP1 (black) and WMAP3 (red) parameters. The limiting mass of the halo population is chosen so as to keep a different quantity constant along a solid curve in each panel: cosmic mass fraction F (top left), minimum virial temperature T (top right), clustering strength Δ_8 (bottom left) and clustering strength of the $z = 0$ descendents $\Delta_{8,0}$ (bottom right). The dashed curves in each panel repeat those of Fig. 4.16. The black and red numbers label the WMAP1 and WMAP3 curves, respectively. See the text for details.

plotted for the same set of mass limits in the two cosmologies, and give almost identical abundances at $z = 0$ for low masses. This can be used to identify the WMAP3 curves at high redshift where they deviate very substantially from the WMAP1 curves. Springel et al. (2005) showed these theoretical predictions to be in excellent agreement with Millennium

Simulation results for $z \leq 10$. At all masses the difference in halo abundance between the two cosmologies increases with the increasing redshift. For $M > 10^{15} M_{\odot}$ the abundance difference is already almost an order of magnitude at $z = 0$, and the same is true for $M > 10^{12} M_{\odot}$ at $z = 5$ and $M > 10^{8} M_{\odot}$ at $z = 10$.

In Fig. 4.17, we give abundance-redshift relations for halo samples defined above lower mass limits $M_{min}(z)$ which correspond to other conditions, as in figure 2 of Mo & White (2002). In each of these plots the two curves of Fig. 4.16 are repeated as dashed curves. These can be used as a reference to obtain the halo mass corresponding to each point in the abundance-redshift plane.

In the upper left panel of Fig. 4.17 the solid curves link halo populations containing given fractions F of the total cosmic mass density at each redshift. The labels give F values for the curves they are placed next to. Where no label is given the F value can be inferred from the surrounding curves. Red curves show WMAP3 results for the same F values and lie above the corresponding WMAP1 curves at all redshifts. At $z = 0$ the curves are close enough that it is easy to infer the F value for each red curve by comparing it with the corresponding black curve. For example, for WMAP1 at $z = 0$, one percent of all cosmic mass is in dark halos above a lower mass limit corresponding to abundance $n = 5 \times 10^{-7} h^3 \mathrm{Mpc}^{-3}$, thus $M > 10^{15} \mathrm{M}_{\odot}$ (from Fig. 4.16). For WMAP3, the $z = 0$ abundance at $F = 0.01$ is about a factor of 2 higher, and the corresponding mass is about 2.5 times smaller. At $z = 5$ the one percent mass point corresponds to $n = 10^{-3} h^3 \mathrm{Mpc}^{-3}$ and $M > 4 \times 10^{11} \mathrm{M}_{\odot}$ for WMAP1, but to $n = 10^{-2} h^3 \mathrm{Mpc}^{-3}$ and $M > 4 \times 10^{10} \mathrm{M}_{\odot}$ for WMAP3.

In the upper right panel of Fig. 4.17 the solid curves link halo populations at each redshift with virial temperatures T in excess of a given value. Labels give the decimal logarithm of the limiting temperature in Kelvin and are placed next to the curve they refer to. At $z = 0$, there is a close correspondance between WMAP1 and WMAP3 at high abundance. At low abundance (high mass) the WMAP3 curves lie below their WMAP1 counterparts. At $z = 10$, the current best estimate of the reionization redshift, only halos with $M > 8 \times 10^{7} \mathrm{M}_{\odot}$ have virial temperatures sufficient to ionize hydrogen ($T > 10^4 K$) and are thus able to cool their baryonic component effectively. For WMAP1 parameters, the comoving abundance of such halos is $n = 10 h^3 \mathrm{Mpc}^{-3}$ and they contain a fraction $F \sim 0.04$ of all cosmic matter (from the upper left plot of Fig. 4.17). For WMAP3 parameters, the predicted abundance of such halos drops by about a factor of 6, and the fraction of cosmic matter contained in them drops by about an order of magnitude. This is the reason why reionization is much more difficult to explain (at $z = 10$) for the revised WMAP parameters. Differences of this kind also explain why we get higher global star formation rates at $z \sim 5$ in our model A1 than in our models B3 and C3 (Fig.4.12) as well as a correspondingly higher stellar mass function in A1 at high redshift (Fig. 4.14).

In the lower left panel of Fig. 4.17 the solid curves link halo populations at each redshift which have a given strength of clustering in comoving coordinates as characterized by $\Delta_8(M, z)$, the rms fluctuation in overdensity of haloes more massive than M at redshift z after smoothing with a spherical top-hat filter of comoving radius $8h^{-1}\mathrm{Mpc}$. As in the other panels, the labels give Δ_8 values for the curves they are placed next to. At redshifts 5 to 10, the WMAP3 curves lie below the corresponding WMAP1 curves at low abundances but above them at high abundances. Comparing the dashed and solid curves in this panel,

one sees that at $z = 0$ the clustering strength of halos is very similar in the two cosmologies for all lower limits to halo mass. This is the result visible in the lower panel of Fig. 4.4. At $z = 5$, however, these same curves show the clustering strength of halos to be substantially stronger in WMAP3 for all limiting halo masses than in WMAP1 (typically by 25 to 40% in Δ_8). This is the result seen for low-mass (sub)halos in the right column of Fig. 4.15.

Finally, in the lower right panel of Fig. 4.17 solid curves link halo populations at each redshift for which the $z = 0$ descendents have a given clustering strength, as indicated by $\Delta_{8,0}$, their present-day value ofΔ_8. As in the other panels, the labels give values of $\Delta_{8,0}$ for the curves they are placed next to. At $z = 0$, the two cosmologies predict nearly identical clustering strengths at intermediate abundances. Mo & White (2002) give a number of examples of how this plot may be used. Here we note that the progenitor population which ends up with a given $z = 0$ clustering strength is substantially more strongly clustered at high redshift in the WMAP3 cosmology than in the WMAP1 cosmology.

Acknowledgements

We thank Volker Springel for providing us with the simulation code GADGET2 and with post-processing software. We thank Cheng Li for help in understanding the SDSS data and for providing the PVD fitting code used in his paper. We thank Lan Wang for providing the HOD galaxy catalogue from her Millennium Simulation model. We also thank J. Blaizot, L. Gao, G. Guzzo and Y. P. Jing for helpful discussions, and an anonymous referee for suggesting the inclusion of the PVD analysis and offering other useful comments. The simulations described in this paper were carried out on the Blade Centre cluster of the Computing Center of the Max-Planck-Society in Garching. The Millennium Simulation data used in this paper are publicly available from http://www.mpa-garching.mpg.de/millennium

Chapter 5

Are mergers responsible for universal halo properties?

Abstract

N-body simulations of Cold Dark Matter (CDM) have shown that, in this hierarchical structure formation model, dark matter halo properties, such as the density profile, the phase-space density profile, the distribution of axial ratio, the distribution of spin parameter, and the distribution of internal specific angular momentum follow 'universal' laws or distributions. Here we study the properties of the first generation of haloes in a Hot Dark Matter (HDM) dominated universe, as an example of halo formation through monolithic collapse. We find all these universalities to be present in this case also. Halo density profiles are very well fit by the Navarro et al (1997) profile over two orders of magnitude in mass. The concentration parameter depends on mass as $c \propto M^{0.2}$, reversing the dependence found in a hierarchical CDM universe. However, the concentration-formation time relation is similar in the two cases: earlier forming haloes tend to be more concentrated than their later forming counterparts. Halo formation histories are also characterized by two phases in the HDM case: an early phase of rapid accretion followed by slower growth. Furthermore, there is no significant difference between the HDM and CDM cases concerning the statistics of other halo properties: the phase-space density profile; the velocity anisotropy profile; the distribution of shape parameters; the distribution of spin parameter, and the distribution of internal specific angular momentum are all similar in the two cases. Only substructure content differs dramatically. These results indicate that mergers do not play a pivotal role in establishing the universalities, thus contradicting models which explain them as consequences of mergers.

5.1 Introduction

The mass distribution of the self-gravitating, quasi-equilibrium dark haloes that form in an expanding universe is an issue of fundamental importance. Early work on self-similar spherical collapse predicts virialized structures with power-law density profiles (Fillmore & Goldreich 1984; Bertschinger 1985). As N-body techniques improved, it was realised that, in the hierarchical universes, the profile departs significantly from a single

power law and is better fitted by a profile with curvature in a log-log plot. (Efstathiou et al. 1985; Dubinski & Carlberg 1991). Later, it was established that the density profiles of haloes in CDM and other hierarchical clustering cosmologies, have a universal form which is well represented by the simple fitting formula of Navarro et al. (1996, 1997,hereafter NFW)

$$\rho(r) = \frac{\rho_s}{(r/r_s)(1 + r/r_s)^2} \tag{5.1}$$

where r_s is a characteristic radius where the logarithmic density slope is -2, and $\rho_s/4$ is the density at r_s. The above equation implies that $\rho \propto r^{-1}$ in the inner regions and $\rho \propto r^{-3}$ in the outskirts. A useful alternative parameter for describing the shape of the profile is the concentration parameter $c = r_{200}/r_s$ (r_{200} is the virial radius defined as the radius within which the mean density is 200 times the critical value). Shortly after the NFW papers, Huss et al. (1999b) showed that the NFW model also fit halos which form by monolithic collapse (i.e. without mergers) in a HDM cosmology. Nevertheless much work has focused on the role of mergers in establishing the NFW profile, since mergers contribute substantially to the growth of haloes in the CDM model (Raig et al. 1998; Salvador-Sole et al. 1998; Syer & White 1998; Subramanian et al. 2000; Dekel et al. 2003). Syer & White (1998) analysed dynamical processes during repeated mergers, concluding that the universal profile is generated by tidal stripping of small haloes as they merge into larger objects. Dekel et al. (2003) extended this model and found the tidal compression from a halo core makes the satellite orbits decay from the radius where $\rho \propto r$ to the halo center and causes a rapid steepening of the inner profile to $\rho \propto r^{-\alpha}(\alpha > 1)$. Recent work has confirmed the NFW hypothesis, extending the comparison to a much wider range of densities and radii than the original work, and uncovering small but significant deviation, between the mean density profiles of simulated dark halos and the NFW formula (Power et al. 2003; Diemand et al. 2004; Merritt et al. 2006; Graham et al. 2006; Gao et al. 2007; Hayashi & White 2007). The differences, however, are quite small compared to the scatter between different haloes of the same mass.

In addition to the density profile, other halo properties are found to follow universal profiles or universal distributions in the hierarchical CDM model. The "phase-space density" $\rho(r)/\sigma^2(r)$ has a remarkably accurate pure power-law distribution with radius (Taylor & Navarro 2001; Barnes et al. 2006). The distributions of shape parameters (e.g. the axis ratios) have a weak dependence on mass and redshift (Bullock 2002; Kasun & Evrard 2005; Allgood et al. 2006; Bett et al. 2007). The spin parameter distribution is well described by a log-normal function which varies weakly with halo mass (Barnes & Efstathiou 1987; Warren et al. 1992; Cole & Lacey 1996; Bullock et al. 2002; Bett et al. 2007). Bullock et al. (2001) also found that the cumulative mass distribution of specific angular momentum j is well fitted by a universal function. All these distributions appear to depend little, if at all, on the global cosmological parameters and on the shape of the initial matter power spectrum. However, the origin of these universalities is still not well understood.

In this paper, we will test whether mergers are the dominant physical mechanism to produce these universal profiles or distributions. To this end, we study a range of properties of the haloes which grow by two different paradigms, by hierarchical aggregation and monolithic collapse. The concordance cosmology (ΛCDM) is a standard hierarchical universe, and the HDM dominated universe provides an example where formation of the first

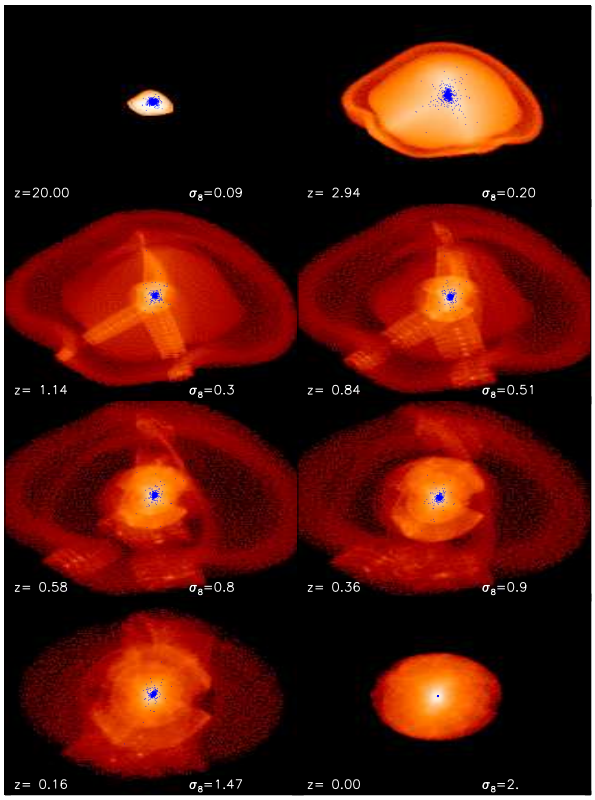

Figure 5.1: The evolution of a massive halo in a HDM universe with mass $1.3 \times 10^{15} M_{\odot}/h$ at redshift zero. All particles within r_{200} at $z = 0$ are traced back to seven higher redshifts. In addition the particles in the very inner region $r < 0.01 r_{200}$ are traced back and are shown as the blue points. The size of each box is 8Mpc/h in physical (not comoving) units. The redshift and the corresponding σ_8 are showed in each panel.

haloes is monolithic. In a HDM universe, small objects cannot form because free-streaming effects smooth out small-scale structure in the initial condition. The first halos then form by smooth collapse.

We begin in section 5.2 with a summary of the N-body simulations and halo catalogues used in this paper. In section 5.3, we give a general description of how halos form and evolve in the HDM universe. In section 5.4, a range of halo properties are studied in depth in our two model universes. Then, we will summarise and discuss our results in section 5.5.

5.2 The simulations and halo catalogues

In this work, we simulate the HDM density field using 512^3 particles within a $100\mathrm{h}^{-1}\mathrm{Mpc}$ cube. For simplicity, we choose an Einstein-de Sitter universe dominated by a single massive

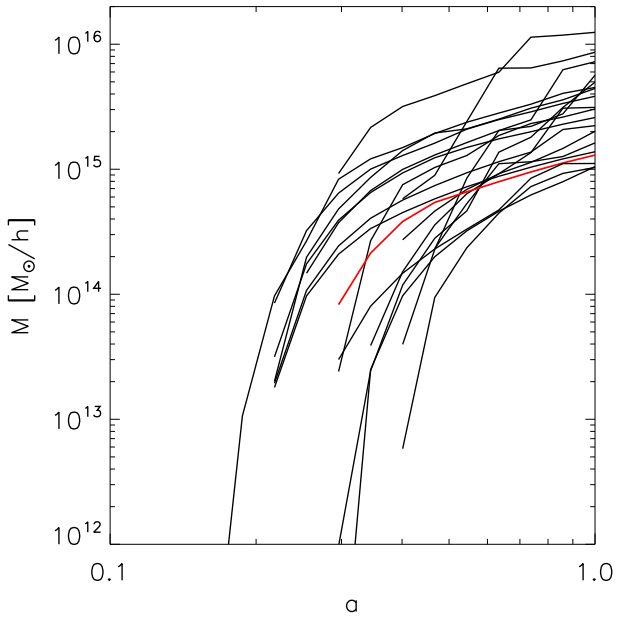

Figure 5.2: Mass assembly histories (MAH) for the 10 most massive haloes at $z = 0$ in the HDMRUN sample. The red curve indicates the halo presented in Fig. 5.1

neutrino. Then the cosmological matter density parameter is $\Omega_m = 1$ and the simulation particle mass is $2.07 \times 10^9 M_\odot/h$. The initial power spectrum used to perturb the initial particle set is based on the theoretical prediction of Bond & Szalay (1983). The power spectrum in a HDM universe possesses a coherent free streaming scale: $\delta_{\rm nu} = 22.2$Mpc in our case. The corresponding damping mass is $7.28 \times 10^{14} M_\odot/h$. This power spectrum is normalised to $\sigma_8 = 2$ which corresponds to the collapse of the first non-linear structures at $z \sim 6$. This simulation was presented as glass512 in Wang & White (2007, hereafter paper I) and more technical details can be found there. We choose to compare it with a simulation of the WMAP1 model from Wang et al. (2008). This simulates a concordance ΛCDM universe with 540^3 particles in a $125{\rm h}^{-1}$Mpc cube. Hereafter we refer these two simulations as HDMRUN and CDMRUN. The softening lengths for these two simulations are 10 and 5kpc/h in the HDM and CDM cases respectively.

As pointed out in Paper I, the population of haloes in HDMRUN is contaminated because discreteness effects break up the filaments and produce many artificial small haloes. The resolution limit above which haloes are immune to this effect is $M_{lim} = 8.8 \times 10^{12} M_\odot/h$, and corresponds to about 5000 particles. In the current study we therefore focus primarily on well resolved haloes with particle number $N_{200} > 10000$ within virial radius r_{200} in two simulations. Several of our most massive HDM haloes experience one or two major mergers at low redshift as in the CDM case. We exclude these second generation haloes from our analysis below. The number of haloes which satisfy the above constraints is 58 and 304 in HDMRUN and CDMRUN respectively. When studying the M_{200}-c relation, we reduce

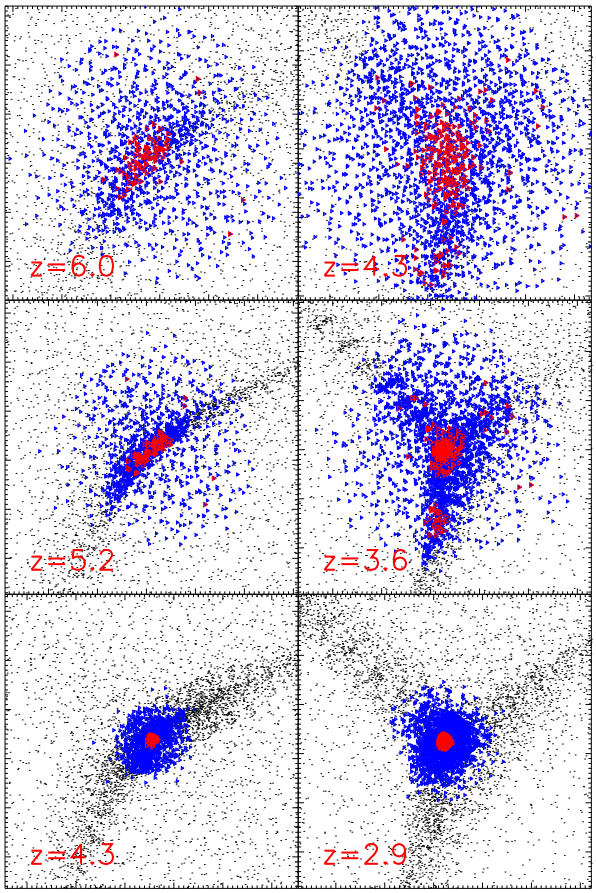

Figure 5.3: Formation histories of two "first" objects in a HDM universe. The right column shows a halo with $N_{200} = 2686$ at $z = 2.9$ (roughly $M_{200} = 3.5 \times 10^{14} M_{\odot}$); while the left column shows another halo with $N_{200} = 1215$ ($M_{200} = 1.6 \times 10^{14} M_{\odot}$) at $z = 4.3$. All particles in both halos at the last redshift are traced back to higher redshifts and presented as blue points. Particles in the very inner region $r < 0.1 r_{200}$ are traced back and presented as red points. Other background particles are shown with black points. The coordinate is comoving scale, and the size of each box is 6Mpc/h. The redshift is labeled in each panel. The simulation glass128 (see Paper I) is used here. Note the artificial discreteness features visible in the filaments in the $z = 3.6$ panel.

the particle number limit to 5000 in order to cover a wider mass range. We then have 84 (HDMRUN) and 1752 (CDMRUN) haloes in the two simulations.

Our halos are identified by a standard $b = 0.2$ friends-of-friends (FOF) group-finder (Davis et al. 1985). Then the SUBFIND algorithm (Springel et al. 2001) is used to resolve these objects into substructures and main subhaloes. The latter then define our halo sample through our N_{200} limits. At high redshift, the FOF method tends to link more particles

together especially in our HDMRUN where large filaments and sheets are easily joined. SUBFIND defines the centre as the minimum of the gravitational potential, and this is used to estimate N_{200}. We also use merger trees built up from the subhalo catalogue produced by the SUBFIND algorithm (see Springel et al. 2005).

5.3 Monolithic Growth

In Fig: 5.1, we study the evolution of a typical halo in our HDMRUN simulation. The mass of this halo is about twice the free-streaming mass scale. In the lower right corner ($z = 0$), all particles within r_{200} are chosen. These are then traced back to the initial condition in the other panels. The particles within the central region $r < 0.01r_{200}$ are also traced back to high redshift and are highlighted with blue points. It is interesting that these images are not similar to those found in the concordance CDM universe using a similar representation by Gao et al. (2004): the whole density field is smooth at all times and no obvious substructures are seen. The collapse along the filaments into knots occurs simultaneously with the accretion of diffuse particles. At redshift 1.14 and 0.84, some parts of the filaments are missing since they fall outside r_{200} at $z = 0$. The particles which end up within $0.01r_{200}$ stayed close together at all times, even in the initial condition. They fall to the centre in a smooth spherical collapse. In a CDM universe, as presented in Fig 2. of Gao et al. (2004), the matter which ends up in the central region typically comes from a number of different objects at early times.

In Fig 5.2 we present the mass assembly history (MAH) of the 10 most massive haloes in the HDMRUN sample. This is just the mass growth of the most massive progenitor in each case. We find that the MAHs are similar to those of haloes in a CDM universe: at early stages, the mass grows rapidly; but this slows dramatically towards $z = 0$. For example, the MAH of the halo shown in Fig. 5.1 is presented as a red curve in Fig 5.2. This halo stays in the rapid growth phase until $z = 1.2$, and its assembly is dominated by smooth spherical infall as Fig. 5.1 indicates. This appears quite different from the hierarchical growth described by Wechsler et al. (2002) and Zhao et al. (2003): their rapid growth phase is dominated by mergers. They also speculated that the universal inner density profile results from violent relaxation during this fast merger phase. We will see below that the density profile is also universal in our HDM simulation. Thus the NFW profile apparently does not require mergers, as noted originally by Huss et al. (1999a).

Halo formation histories obviously differ in CDM and HDM universes. Another interesting question is how and where the first objects form in the HDM case. Here we must keep in mind that the free-streaming scale in HDM is just a characteristic scale and its relationship to the actual mass of the first objects is not obvious. In Fig. 5.3, we present formation histories for two "first" objects. They were identified at $z = 4.3$ (left column) and $z = 2.9$ (right column) when they had gathered 1215 and 2686 particles within r_{200} respectively. In order to see the particles better, we here use a lower mass resolution simulation glass128 which was also presented in Paper I. This simulation has the same initial density field as HDMRUN, but 16 times lower mass resolution. As in Fig 5.1, we trace back all particles within r_{200} (blue) and within $0.1r_{200}$ (red) to higher redshift. Other background particles are shown as black points. It is obvious that both haloes form by smooth spherical col-

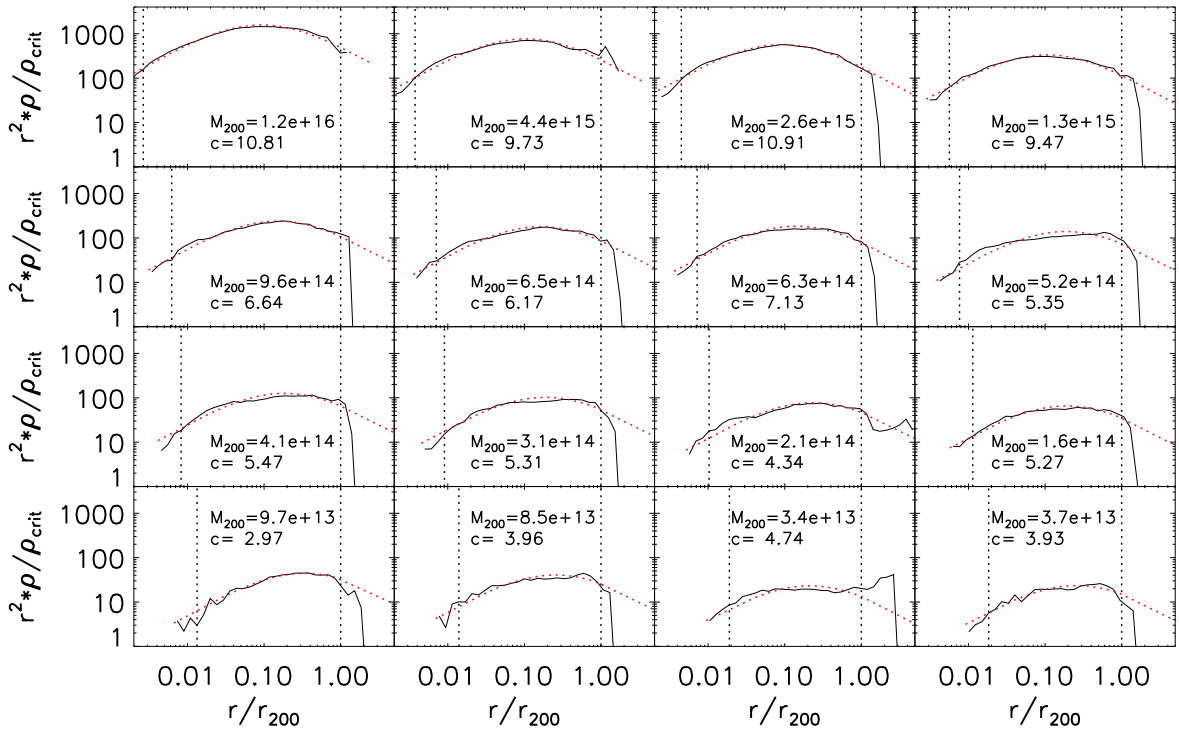

Figure 5.4: Density profiles for 16 haloes with particle number within r_{200} (N_{200}) greater than 10,000. These 16 haloes cover two orders of magnitude in mass. The density profiles are normalized by r^2/ρ_{crit} and the radius are normalized by r_{200}. In each panel, the red dotted curve is the NFW fit to the numerical measurement (black solid curve). Two vertical dotted lines show the softening length and r_{200}. The corresponding M_{200} (in unit of $h^{-1}M_{\odot}$) and the concentration parameter c are listed in each panel.

lapse. In other words, the particles in the filaments and "voids" fall into the halo together. Even the particles within the central region ($< 0.1r_{200}$) seem to follow a roughly spherical collapse. This agrees with what we see in Fig 5.1. In the right column, the halo forms in a node which connects three filaments, and the halo forms almost at the same time as the three neighbour filaments. For the case in the left column, the halo forms at the end of one filament ($z = 6.0$) and then grows at the same time as another filament. We have also checked some other examples and find that almost all of them are born in nodes or at the ends of filaments and grow by spherical accretion.

Merger events in such a monolithic universe are expected to be rare. We find this to be true in our HDM simulations. For example, in HDMRUN, if we define merger events as the merging of 'real' haloes whose masses are larger than the mass limit, only a few haloes experience a major merger event (with mass ratio of the two progenitors greater than $1:3$). We exclude these haloes from our study in this paper. Only about 30 percent of the remaining haloes experience minor merger events, and it is thus reasonable to regard them as a sample of 'first' haloes.

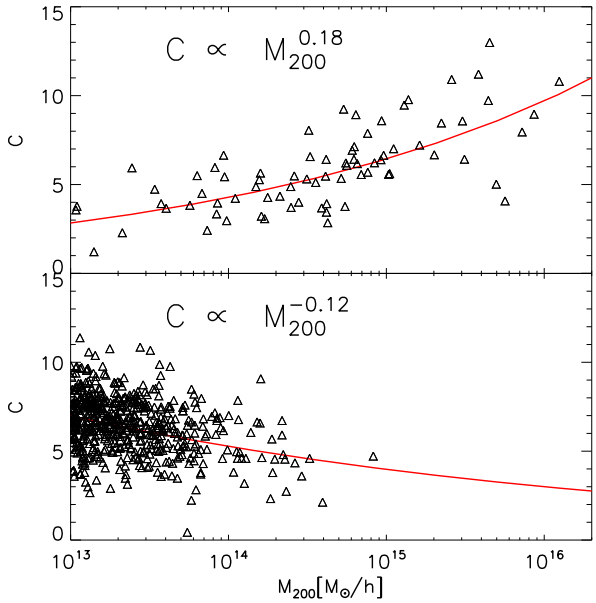

Figure 5.5: The distributions of halo mass M_{200} and concentration parameter c. The top panel is from HDMRUN and the bottom one from CDMRUN.

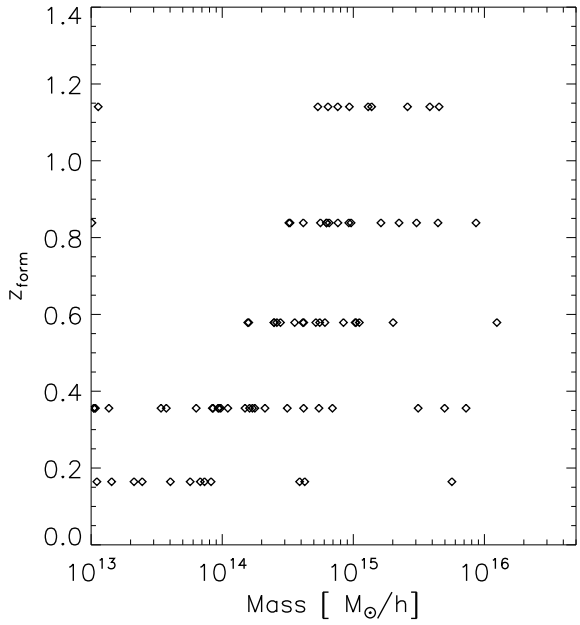

Figure 5.6: The distribution of formation time for haloes with $M_{200} \geq 10^{13} M_{\odot}/h$ in the HDMRUN sample.

5.4 Halo properties in the two universes

In this section, we will study a range of "first" halo properties in the HDM universe and compare them with their counterparts in the ΛCDM model.

5.4.1 Density Profile and Formation History

Previous studies (Moore et al. 1999; Colín et al. 2000; Eke et al. 2001; Busha et al. 2007) have focused on the formation of the first haloes in a WDM cosmology and have claimed that the density profiles of these haloes do not differ substantially from the NFW form found in a CDM universe. We support these findings also in our HDM case, confirming the original result of Huss et al. (1999b). In Fig. 5.4, we present density profiles for 16 haloes with mass from $3 \times 10^{13} M_{\odot}/h$ to $4.5 \times 10^{15} M_{\odot}/h$. All these haloes include more than $10,000$ particles. Here the concentration parameter is measured by fitting an NFW profile to the numerical results using logarithmically spaced radial bins in the range $2\epsilon < r < r_{200}$. The softening length ϵ and r_{200} are shown in the plot by vertical dotted lines. We find these profiles to follow the NFW model very well. It is also obvious that the ρ_s and c have a strong mass dependence. Both parameters increase with increasing halo mass. These mass dependences disagree with those in a CDM universe where more massive halos have a lower ρ_s and c. In Fig. 5.5, we display the dependence of concentration parameter on halo mass for our two halo samples. In the lower panel, we present results for CDMRUN. The mass dependence, $c \propto M_{200}^{-0.12}$, is close to that found by Neto et al. (2007) and Macciò et al. (2007) $c \propto M_{200}^{-0.11}$. In the upper panel, we present this relation for HDMRUN. It is interesting that the mass dependence inverts and follows $c \propto M_{200}^{0.2}$: the more massive a halo, the larger its concentration parameter.

Many previous studies have found that the structural properties and the mass accretion histories of haloes are closely related in a CDM universe (e.g. Navarro et al. 1996, 1997; Wechsler et al. 2002; Zhao et al. 2003). Concentration increases with the formation time and the characteristic density ρ_s can be related with the mean cosmic density at the time of formation. In Fig. 5.6 , we check this relation for our HDMRUN haloes. The formation time is defined here as the earliest time when half of the halo mass was in its main progenitor. It is interesting that massive haloes form a bit earlier than their low mass counterparts in this cosmology. Combining with the $M_{200} \sim c$ relation showed in Fig. 5.5, we find that the earlier forming objects do indeed have a larger concentration parameter, in agreement with the result for a CDM universe. This indicates that here also the inner part is assembled during the fast early growth phase.

5.4.2 Kinematics

If haloes follow a universal density profile as discussed above, and are in an equilibrium state, then the solution of Jeans equation for spherical, isotropic systems indicates that their kinematic structure may also be universal. Taylor & Navarro (2001) have found that, for dark haloes in a CDM universe, there is a power-law relationship between "phase-space density" and radius: $\rho/\sigma^3 \approx r^{-\alpha}$ with $\alpha = 1.875$, where phase-space density is defined as the ratio of local matter density ρ to the cube of the local velocity dispersion σ. This

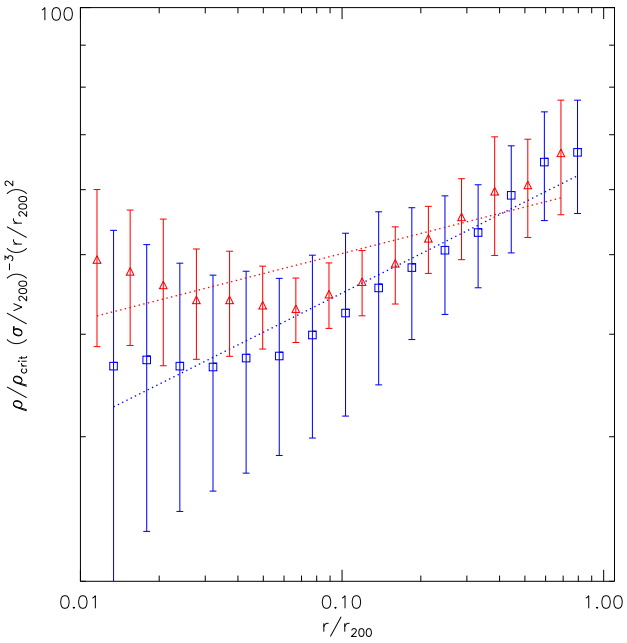

Figure 5.7: Stacked phase density profiles for the 20 most massive haloes in our two halo samples. The profile of each halo is normalized by a factor v_{200}^3/ρ_{crit} before stacking. The dotted straight lines are our power law fits with indices $\alpha = 1.94$ and $a = 1.83$ for HDMRUN(red triangles) and CDMRUN (blue squares) respectively. In order to get a better dynamic range, all symbols and lines multiplied by $(r/r_{200})^2$. The error-bars indicate the 1σ scatter.

phase-space density is inversely related to the local entropy density. In the semi-analytic extended secondary infall model, this nearly scale-free nature of ρ/σ^3 is a robust feature of virialized haloes in equilibrium (Austin et al. 2005). Further investigation of halo formation processes indicates that this scale-free feature cannot be the result of hierarchical merging; rather it must be an outcome of violent relaxation (Austin et al. 2005; Barnes et al. 2006). We show results for massive haloes in our HDM and CDM samples in Fig. 5.7. In order to reduce the noise, we stack the 20 most massive haloes in each case. Before the stacking, the profile for each halo is normalized by a factor V_{200}^3/ρ_{crit}. The error-bars in the plot indicate the 1σ scatter. We find the two profiles to follow a power laws moderately well. The fitted indices differ slightly: $\alpha = 1.94$ and 1.83 for HDMRUN (red) and CDMRUN (blue) respectively.

In addition, the velocity anisotropy in haloes depends on radius: The dispersion tensor is isotropic near the center and moderately radially anisotropic near the virial radius. In Fig. 5.8, we present averaged velocity anisotropy profiles $\beta(r) = 1 - \sigma_t^2/\sigma_r^2$ for the 20 most massive haloes in our CDM and HDM samples. Here σ_t and σ_r are the tangential and radial velocity dispersions respectively. We again find very similar results for the two cases. Outside $0.2r_{200}$, the mean radial anisotropy in HDMRUN (red) is slightly larger than in

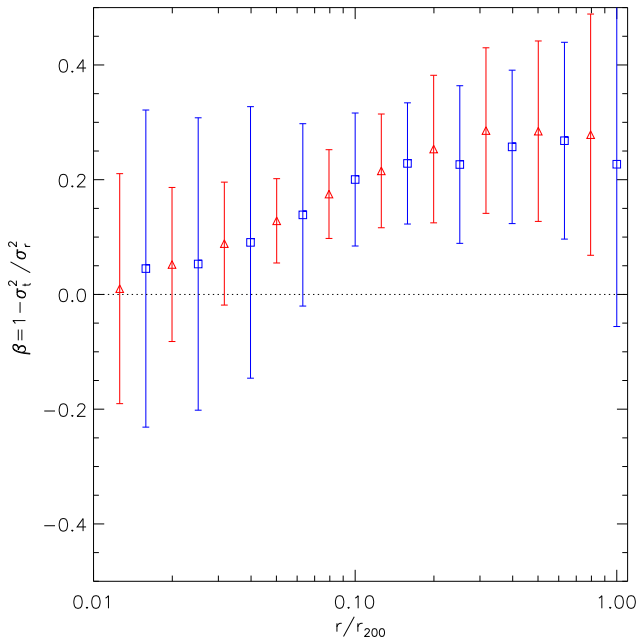

Figure 5.8: The stacked velocity anisotropy profile $\beta(r)$ for the 20 most massive haloes in the HDMRUN (red triangles) and CDMRUN (blue squares) samples. The error-bars indicate the 1σ scatter.

CDMRUN (blue), but the effect is very small.

The similarities in phase-space density profile and velocity anisotropy profile in the two cases indicate that these properties are also universal and depend little on whether a halo is assembled by mergers or by monolithic collapse.

5.4.3 Halo Shape

In Fig. 5.9, we show axis ratios for haloes in HDMRUN and CDMRUN. We define the axes using the inertia tensor of the mass distribution within the virial radius r_{200}:

$$I_{\alpha\beta} = \frac{1}{N_p}\Sigma_{i=1}^{N_p} r_{i,\alpha} r_{i,\beta}. \tag{5.2}$$

where the r_i are the positions of the N_p particles within r_{200}. α and β are tensor indexes with values of 1,2 or 3 and indicate the three components of each particle's position. After diagonalizing this matrix, characteristic axis lengths are found as the square root of the eigenvalues. In the top two panels of Fig. 5.9, the intermediate-major (b/a) and minor-intermediate (c/b) axis ratios of halo samples from the two simulations are presented. The distributions of shape parameters are clearly very similar in the two cases. The mean values of the axis ratios b/a and c/b are both close to 0.82. In the lower two panels, we compare the probability distributions of b/a and c/b in the two simulations. The Kolmogorov-Smirnov

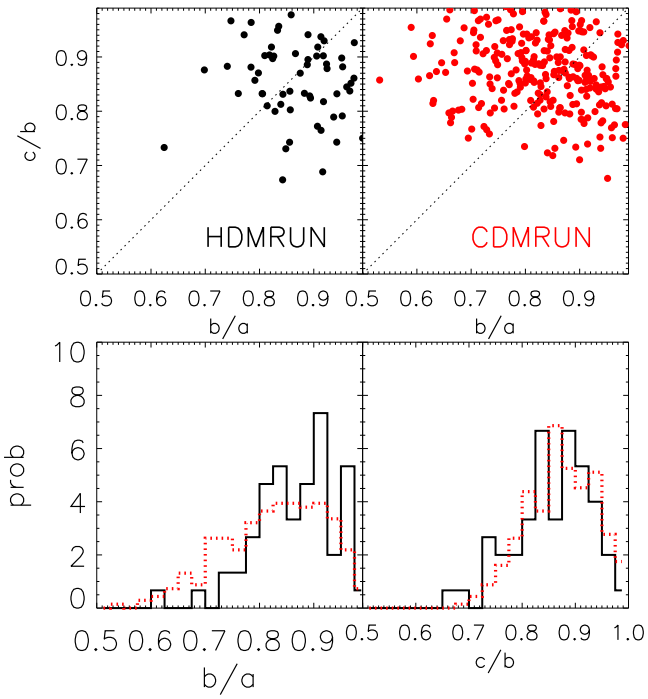

Figure 5.9: Scatter plots of the axis ratios of haloes in HDMRUN and CDMRUN (top two panels) and histograms of their probability distributions (lower two panels: red dotted and black solid curves are histograms for CDMRUN and HDMRUN respectively). Here a, b and c are the major, intermediate and minor axis lengths. Kolmogorov-Smirnov tests indicate that the distributions in two universes do not differ significantly.

test shows no evidence for any difference between the distributions in the HDM and CDM cases.

The above results indicate that different growth paths (monolithic or hierarchical) affect the global shape of halos very little.

5.4.4 Spin and Angular Momentum Distribution within Haloes

The conventional measure of halo angular momentum, the dimensionless spin parameter λ, is defined in terms of mass, energy and angular momentum and is related to the ratio between a halo's mean angular velocity (ω) and the angular velocity which would be required to support it by rotation alone(ω_0) (Peebles 1969):

$$\lambda \equiv \frac{J|E|^{1/2}}{GM^{5/2}} \simeq 0.4\frac{\omega}{\omega_0}. \tag{5.3}$$

The total angular momentum J and energy E are needed to calculate this parameter. However, in this study, we follow Bullock et al. (2001) and define a more easily measured spin parameter λ' as:

$$\lambda' = \frac{J}{\sqrt{2}M_{200}Vr_{200}} \tag{5.4}$$

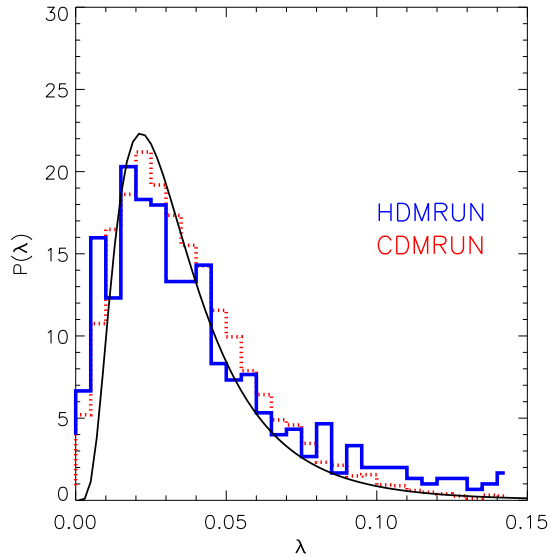

Figure 5.10: The probability distribution of the spin parameter λ' in HDMRUN (blue solid) and CDMRUN (red dotted). The black solid curve is the fit to a CDM universe from Bullock et al. (2001).

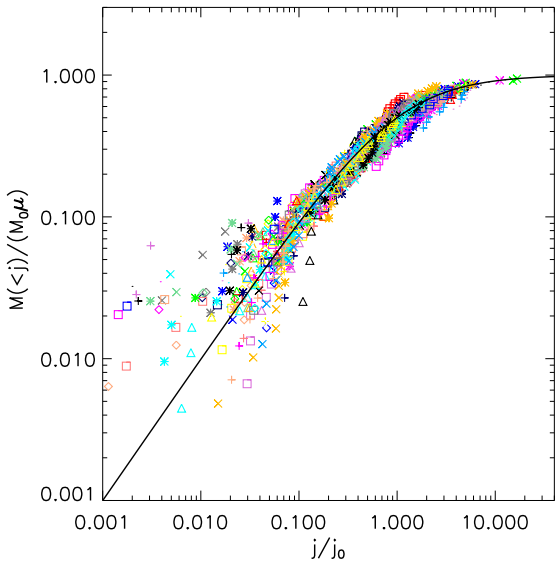

Figure 5.11: Mass distributions of specific angular momentum within 58 massive haloes in HDMRUN. Each coloured symbol presents one halo. Each mass distribution is normalized by its own virial mass (M_0) and shape parameter μ, all symbols then stay around the black curve $\frac{x}{1+x}$.

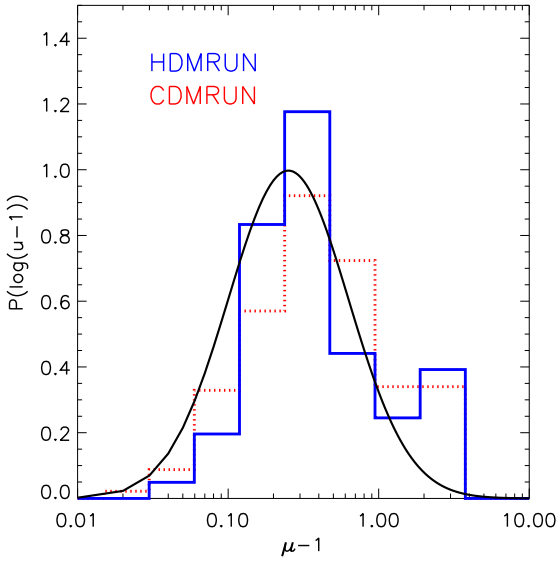

Figure 5.12: The probability distribution of the shape parameter μ in HDMRUN (blue solid) and CDMRUN (red dotted). The black solid curve is the fit to a CDM universe from Bullock et al. (2001).

where J is the total angular momentum of all particles within r_{200} and $V = \sqrt{GM_{200}/r_{200}}$ is the circular velocity at radius r_{200}. This definition gives similar value to Equ. 5.3. Because λ' is defined for isolated systems but applied to haloes in their cosmic context, the practical definition of a halo is more critical than the choice of definition of λ (Bett et al. 2007).

The nett spin of a dark halo is acquired from torques exerted by neighbouring structures at early times (Hoyle 1949; Peebles 1969; Doroshkevich 1970; White 1984), and does not evolve much after the turnaround point of a halo's MAH. After this time, the moment of inertia of the collapsing material decreases and the universal expansion reduces the strength of tidal forces (Porciani et al. 2002). Vitvitska et al. (2002) noted that the spin parameter fluctuates strongly with time, depending on the details of assembly: the spin increases abruptly during a major merger and decreases gradually between such mergers. D'Onghia & Navarro (2007) found this effect to reflect the unrelaxed nature of the system; equilibrium haloes show no significant correlation between spin and merging history. In our HDM simulation, most haloes grow in a monolithic way, so the impact from major mergers should be negligible.

In Fig. 5.10, we compare the distribution of spin parameters in our HDMRUN halo sample with that in the CDMRUN sample. A Kolmogorov-Smirnov test shoes no significant difference between two different cases.

Bullock et al. (2001) noticed that the distribution of specific angular momentum j within the CDM haloes has a universal profile, specifically that the distribution of mass over

specific angular momentum j is well fit in most haloes by the universal form:

$$M(< j) = M_0 \frac{\mu j}{j_0 + j} \tag{5.5}$$

where M_0 is the virial mass, which we here replace by M_{200}. $j_0 = (\mu - 1)j_{max}$ and j_{max} is the maximum specific angular momentum. This behaviour is not truly universal since μ is an adjustable shape parameter which varies from halo to halo. We now check this distribution for haloes in our HDM and CDM simulations.

In order to resolve the j profile adequately, we only consider haloes with particle number larger than 3×10^4. Different regions are defined as cells in the usual spherical coordinates (r, θ, ϕ). We make sure that each cell contains an approximately equal number of particles. We first divide the whole halo into 10 radial shells which host almost equal particle numbers. Then each shell is further divided into six zones: each cell spans the full 2π range in ϕ and spans the equal solid angle between $\cos(\theta) = -1$ and 1. The two zones with the same r and $|\cos(\theta)|$ that are above and below the equatorial plane are assigned to one cell. In Fig. 5.11, we present the distribution of normalized mass fraction $M(< j)/(M_0\mu)$ for 58 haloes from HDMRUN. Different coloured symbols present different haloes. We find that, after the parameter μ has been adjusted, all haloes are close to the curve $x/(1+x)$, thus the specific angular momentum profile can be described by one shape parameter μ very well. We compare the probability distribution of this parameter for the HDMRUN and CDMRUN samples in Fig. 5.12. The distributions are similar and close to a log-normal distribution as noted by Bullock et al. (2001) (A Kolmogorov-Smirnov test shows no indication of a difference.) A similar result was found by Chen & Jing (2002) for WDM haloes: the distribution is statistically indistinguishable from the CDM case. As in van den Bosch et al. (2002) and Chen & Jing (2002), we also find some cells with negative angular momentum. These are excluded from our analysis.

The similarity between the distributions of spin parameter and internal specific angular momentum in the HDM and CDM cases shows that formation through mergers is not necessary to generate "universal" angular momentum distributions. This conflicts with the explanation which Vitvitska et al. (2002) give for the origin of the angular momentum distribution within CDM haloes.

5.4.5 Substructure

In Paper I, we gave a detailed discussion of the formation of substructures in a HDM Universe. We found almost all substructures in HDM haloes are either a result of spurious filament fragmentation (at low masses) or major mergers at late times (at large masses). As we see in Fig.5.1, at $z = 0.84$ and $z = 0.58$, there are many artificial regularly spaced objects falling into the clusters from filaments and these become substructures of the HDM haloes. This effect prevents us from studying the abundance of the real subhaloes at low mass since it is hard to identify which subhaloes (if any) are real. In Fig 5.13, we present cumulative mass functions of subhaloes for stacks of the 30 most massive haloes in each sample. For the HDM case, the subhalo mass functions of a few individual haloes are presented with black curves. For haloes in the HDM universe, we define 'real' subhaloes to have mass greater than $0.1M_{\rm lim} = 8.8 \times 10^{12} M_\odot/h$, and smaller subhaloes are considered

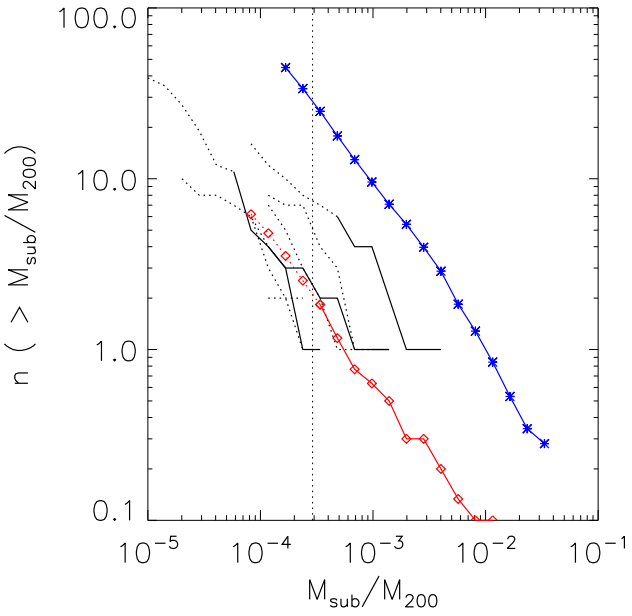

Figure 5.13: The stacked cumulative subhalo mass function of the 30 most massive haloes for our two samples: red diamonds and blue stars are for HDM and CDM haloes respectively. The results for several individual HDM haloes are also presented as black curves. The HDM curves are divided into two parts at $0.1M_{lim}$: real (spurious) subhaloes have masses greater (less) than this mass limit and are shown with solid (dotted) curves. The vertical dashed line indicates the mean mass limit for all 30 haloes in HDMRUN $< 0.1M_{lim} >$.

'spurious'. The mass function of the 'real' and 'spurious' subhaloes are shown as solid and dotted lines respectively. The vertical dashed line indicates the mean mass limit $< 0.1M_{lim} >$ for all 30 haloes in the HDMRUN. We have assumed here that the average mass loss fraction is 0.1 when a subhalo falls into its parent halo and suffers tidal stripping. It is interesting that both distributions follow a similar power law. That of the HDMRUN sample is approximately one order of magnitude lower than the counterpart in CDMRUN and on average very few 'real' subhaloes are found in each halo in the HDM case. This reflects the lack of hierarchical build up in the HDM case.

5.5 Conclusions and Discussion

In this paper , we study the haloes which form by monolithic collapse in HDM cosmological simulations, and we compare a range of properties of these haloes with these of their counterparts in a ΛCDM hierarchical universe. From this comparison we explore which physical mechanisms are responsible for the universal profiles or distributions of halo properties. Our simulated HDM universe has an inherent characteristic scale below which the

formation of small haloes is suppressed. In this universe, the first generation of halo forms in a "top-down" way – more massive haloes form earlier by smooth accretion. Mergers occur in significant numbers only when building up later halo generations. The HDM cosmology thus provides a good example of monolithic halo growth from Gaussian initial condition. Furthermore, because the HDM characteristic scale is much more sharply imprinted than in the WDM case, we have a large and well defined monolithic halo sample. As a result, we can explore monolithic growth in a better controlled way than previous work based on WDM universes. We summarise our conclusions on monolithic halo formation as follows:

(i) First generation haloes grow by smooth accretion. Such haloes form from roughly spherical collapse of matter around the nodes or ends of filaments. The formation histories of these monolithic haloes are also characterised by two phases: fast initial and slow later accretion, very similar to those found in a CDM universe. In the fast growth phase, smooth infall is the main mechanism rather than the mergers seen in the CDM case.

(ii) The density profiles of our monolithic haloes are well fit by the NFW profile. The concentration parameter c and the characteristic density ρ_s have strong dependences on halo mass: the more massive a halo, the larger c and ρ_s. This is the inverse of the CDM dependence, but the concentration-formation time relation is quite similar in the two cases: earlier formed haloes tend to be more concentrated than their later formed counterparts.

(iii) Phase-space density profiles and velocity dispersion anisotropy profiles are very similar in our two cases. This indicates that the kinematic structure of haloes is generated by wide variety of dynamical collapse processes, not just by mergers.

(iv) The distribution of shape parameter is very similar in HDM and CDM universes, as are the distributions of spin parameter λ' and of internal specific angular momentum.

(v) In our HDM simulations, most subhaloes result from the infall of spurious small haloes which form in the filaments as a result of numerical discreteness. The subhalo abundance is much lower than in CDM haloes, and indeed there are very likely no subhaloes in first generation HDM haloes.

The above results show that, except for substructure, the properties of haloes formed by monolithic collapse are very similar to those of haloes formed by hierarchical clustering in a CDM universe. In particular, they have very similar profiles of density, phase-space density and specific angular momentum, and very similar distributions of axial ratios and spin parameter. These results indicate that mergers are not responsible (or are not required) for the universal properties of CDM haloes. This agrees with results from earlier work based on constrained simulations (Huss et al. 1999a; MacMillan et al. 2006). Attempts to explain these universal properties with merger-driven models seem unlikely to be on the right track.

The results in this study could also find some applications in realistic dark matter models, especially for the WDM cosmology. In our HDM universe, first generation haloes form by smooth near-spherical accretion with initial mass well below the characteristic free-streaming mass. These haloes form simultaneously with the filaments and sheets. This picture is different from that in the familiar CDM universe. Our results suggest that the structure of the first haloes, in a WDM universe (and thus, presumably, also of their later descendants) will differ little from the structure of CDM haloes, despite the differences in assembly history. This makes it seem unlikely that changing to a WDM model will help resolve the apparent problems of the CDM model on galactic scales.

Acknowledgments

We thank Volker Springel for providing us with the simulation code GADGET2 and with post-processing software. JW thanks Carlos Frenk for his hospitality at ICC, Durham where the draft of this paper was finished. JW also thanks Liang Gao and LiXin Li for useful comments. The simulations described in this paper were carried out on the Blade Centre cluster of the Computing Center of the Max-Planck-Society in Garching.

Conclusions and Outlook

N-boy techniques and semi-analytic galaxy formation models are very useful tools for studying the formation of structure in the Universe. In this thesis, I have used both tools to study three different problems related to this subject. At the end of each chapter, I gave conclusions for each project. Here I just briefly summerise the main results of these three projects, and sketch some future perspectives.

In Chapter 3, I studied how discreteness effects limit the effective mass resolution of N-body simulations of cosmonogies like WDM or HDM where structure on small scales is suppressed in the linear initial conditions. Filaments occur in such models as part of the natural development of the cosmic web, but I find that spurious discreteness-driven fragmentation of filaments occurs in almost identical fashion whether the initial particle load is a glass or a grid. These spurious clumps are responsible for all the low-mass substructures I have been able to identify at late times in the first generation collapsed HDM halos. Thus, it appears that in an idealised WDM or HDM universe early dark haloes are predicted to contain *no* self-bound substructure of small scale. My tests on idealised systems show this fragmentation to occur because 1-D projections of a 3-D quasi-uniform particle distribution retain substantial power on the scale of the 3-D inter-particle separation, and this power amplifies very rapidly as the effectively 1-D system evolves. By comparing the mass function of dark haloes in 9 simulations from HDM initial conditions based on different particle numbers and different initial loads, I found that these artificial fragments form below a characteristic mass which scales as $m_p^{1/3}k_{peak}^{-2}$, where m_p is the N-body particle mass and k_{peak} is the wavenumber at the maximum of $k^3P(k)$ ($P(k)$ is the power spectrum). This indicates that the effective mass resolution of such simulations improves only as the cube root of the number of particles employed. This effective resolution limit poses a challenge for high mass-resolution WDM simulations which are intended to explore possible resolutions to problems of the CDM model at galactic scales. One possible but very difficult way to resolve filament fragmentation would be to find or design better pre-initial-conditions in which the substantial power at small scale in the 1-D projected power spectrum (e.g. the spikes corresponding to the mean inter-particle separation) is suppressed. Then the breakup of filaments can be avoided due to the absence of initial fluctuations. Besides, discreteness effects is also important in the dynamically resolving the structures of haloes in CDM universe, especially in the very inner region. The detailed studies on these issues are needed to provide more reliable formulas or conditions for the

implements in modern simulation codes.

In Chapter 4, I carried out cosmological structure formation simulations of a ΛCDM universe for the cosmological parameter sets suggested by the first- and third-year WMAP analyses. The significant reduction in the best value for the amplitude of matter fluctuations on $8\,h^{-1}$ Mpc scale (σ_8) combines with the decrease in the estimate of the scalar spectral index for primordial perturbations (n), and with the lowered matter density (Ω_m) to produce a significant delay in structure formation in the WMAP3 case. By coupling my numerical simulations to semi-analytic models for galaxy formation, I found that, in both cosmologies, several combinations of physical parameters can reproduce observed, low-redshift galaxy properties. The star formation, supernova feedback and AGN feedback efficiencies can be played off against each other to give similar results. Given current modelling uncertainties, it is not easy to distinguish the WMAP1 and WMAP3 cosmologies on the basis of low-redshift galaxy properties. However, substantial differences between the various models appear at high redshift. The delay in the structure formation translates directly into a delay in the global star formation history: at $z \sim 6$ the star formation rates in the models based on WMAP3 are lower than those based on WMAP1 by almost an order of magnitude. Somewhat counter-intuitively, I found that at high redshift galaxies of given stellar mass are predicted to be substantially more clustered in the WMAP3 cosmology than for WMAP1. Unfortunately, the uncertainties in the observed luminosities and masses, combined with large cosmic variance uncertainties, are still too large to place strong constraints on the efficiencies and scalings of the physical processes I modeled. More detailed and more statistically precise observations of high-redshift galaxies should be able to discriminate between the models. Once these aspects of the galaxy formation process are better understood, it may indeed be possible to use galaxy surveys to constrain cosmological parameters. For example, careful modelling of high-z objects (Lyman-break galaxies, Luminous Red Galaxies, sub-mm galaxies) and more precise observations help us to distinguish between different cosmological models (e.g. WMAP1 Vs. WMAP3).

In Chapter 5, I analysed a range of halo's properties in two cosmological models: ΛCDM and HDM. These two universes are taken as examples for hierarchical and monolithic structure formation respectively. Using large samples of haloes, I was able to draw statistically robust conclusions on the universality of halo properties in two cases, and on their dependence on halo growth history. In a monolithic universe merger events are extremely rare for the first generation of haloes (because structure formation at small scales is seriously suppressed), but the halo density profile is still well described by the NFW model. In addition, the concentration-formation time relation is similar to that in a hierarchical universe: the haloes which form earlier tend to be more concentrated than their later forming counterparts. These results indicate that the early merger phase in a CDM universes does not play a critical role in establishing the universal NFW profile and the tight correlation between internal structure and formation time. I also found that the absence of merger events has no obvious impact on the universality of other halo properties. In a HDM universe, the phase-space density profile, the distribution of shape parameters, the distribution of spin parameter and the distribution of internal angular momentum all still follow the universal profiles or distributions found for halos formed by hierarchical clustering. These results pose a challenge for merger-driven models which seek to explain these universal properties as a consequence of mergers. Given the similar properties of haloes in CDM and

HDM models, the WDM model cannot be expected to help a lot in resolving the angular momentum problem and core/cusp problem in CDM models. In addition, I found that in HDM universe the first generation of haloes forms by smooth near-spherical accretion with initial mass much less than the characteristic free-streaming mass. They also form simultaneously with the filaments and sheets. This picture is different from that in the normal CDM universe. There are still some space for the detailed studies on these issues. Future possible developments include: a detailed study on the formation of haloes with mass much lower than the free-streaming scale; a more detailed study on the formation of the first objects in WDM universe; a more careful check on the formation of substructures in the first generations of haloes. Such studies will require new simulation techniques.

Acknowledgements

In the past three years, many many people have contributed not only to making my science better and my skills improve, but also to making my life happier, more interesting, and more meaningful. My sincere thanks are due to all of them, even if they are not explicitly mentioned as follow.

Firstly, very warm thanks go to my supervisor Simon White for your invaluable advises and continuous encouragements. I have leaned a lot from you on the approach and attitude to research. It is you who teach me how to be a researcher; how to do the researching; how to write out a good paper; and how to find out the idea for the new researches. Thanks! Simon, it really has been the most amazing experience to work with you. You are one of the two MIPs in my astronomy life. In addition, thank you for being patient for my Chinese-English.

Many thanks also go to Alex Szalay and Carlos Frenk. Although the works which are under your supervisions don't go into this thesis, these projects are also an inseparable part to my PhD life. What I leaned from you is beyond the knowledges and experiences I gained on the science. I also have been impressed with you on how to be a charming researcher. Special thanks to Carlos Frank for your hospitality during my visit to Durham for a half year, then I can finish the writing of this thesis. Many thanks also go to Prof. Gehard Boerner for being the second referee of my thesis and careful reading of the whole thesis.

Many thanks go to Volker. You are so kindly and warm-hearted. Your timely reply to my emails and numerous suggestions helped me a lot on numerical techniques. Besides, the whole thesis is based on your fantastic codes. It is impossible for me to finish this thesis without these codes. Many thanks to Gabriella for your many kindly and timely helps. It is really my pleasure to work with you. Thank you for numerous suggestions on different aspects, for many helps on improving my English writing. Many thanks to Adrian, Manfred, Andreas, Mark, Agis, Andre for your numerous helps and friendship! Many thanks also go to all lecturers in the IMPRS courses. I leaned from you much more than from the books. Many thanks to Cornelia, Kate, Maria, Gabi and other personal secretaries. You made my live in Garching easier and enjoyable. As well many thanks to Werner Becker and Christa Ingram for your efforts to make the life in IMPRS pleasant and enjoyable.

Many thanks to ShuDe Mao, YiPeng Jing, LiXin Li, Liang Gao. I enjoyed very much

talking with you. I was benefited a great deal from your invaluable experiences and comments. Many thanks to my flatmate Lan Wang. It is great to have so much pleasant time with you. Thanks for your wonderful cake, for noting me for the lunch everyday, for numerous encouragements and supports. Many thanks to all Chinese friends I met at Garching: Cheng Li, Qi Guo, Fei Xiang, XiaoLing Zhang, YangFang Li, YuYing Zhang and other guys (I think the complete list will beyond this page). I enjoyed the debats on the science and society with all of you. I enjoyed cooking and drinking with you. Thank all of you to share so much pleasant time with me during these three years.

Many thanks to my friends. I never feel alone in my life because you are always around. I love you for ever! YanChuan Cai, ShuHua Chen and other guys at Durham, thank you for giving me so many wonderful memories there.

Finally, I want to give my special thanks to my dear parents and my lovely young sister. Everything was, is and will be impossible for me without your encouragements and supports.

Bibliography

Allgood B., Flores R. A., Primack J. R., Kravtsov A. V., Wechsler R. H., Faltenbacher A., Bullock J. S., 2006, MNRAS, 367, 1781

Alvarez M. A., Shapiro P. R., Ahn K., Iliev I. T., 2006, ApJ, 644, L101

Austin C. G., Williams L. L. R., Barnes E. I., Babul A., Dalcanton J. J., 2005, ApJ, 634, 756

Banday A. J., Gorski K. M., Bennett C. L., Hinshaw G., Kogut A., Lineweaver C., Smoot G. F., Tenorio L., 1997, ApJ, 475, 393

Bardeen J. M., Bond J. R., Kaiser N., Szalay A. S., 1986, ApJ, 304, 15

Barkana R., Loeb A., 2001, Phys. Rep., 349, 125

Barnes E. I., Williams L. L. R., Babul A., Dalcanton J. J., 2006, ApJ, 643, 797

Barnes J., Efstathiou G., 1987, ApJ, 319, 575

Barnes J., Hut P., 1986, Nature, 324, 446

Baugh C. M., 2006, Reports of Progress in Physics, 69, 3101

Baugh C. M., Gaztanaga E., Efstathiou G., 1995, MNRAS, 274, 1049

Benjamin J., et al. 2007, MNRAS, 381, 702

Benson A. J., Bower R. G., Frenk C. S., Lacey C. G., Baugh C. M., Cole S., 2003, ApJ, 599, 38

Benson A. J., Lacey C. G., Baugh C. M., Cole S., Frenk C. S., 2002, MNRAS, 333, 156

Bertschinger E., 1985, ApJS, 58, 39

Bertschinger E., Gelb J. M., 1991, Computers in Physics, 5, 164

Bett P., Eke V., Frenk C. S., Jenkins A., Helly J., Navarro J., 2007, MNRAS, 376, 215

Binney J., Tremaine S., 1987, Galactic dynamics. Princeton, NJ, Princeton University Press, 1987, 747 p.

Blanton M. R., et al. 2003, ApJ, 592, 819

Bode P., Ostriker J. P., Turok N., 2001, ApJ, 556, 93

Bond J. R., Cole S., Efstathiou G., Kaiser N., 1991, ApJ, 379, 440

Bond J. R., Myers S. T., 1996a, ApJS, 103, 1

Bond J. R., Myers S. T., 1996b, ApJS, 103, 41

Bond J. R., Myers S. T., 1996c, ApJS, 103, 63

Bond J. R., Szalay A. S., 1983, ApJ, 274, 443

Borgani S., Rosati P., Tozzi P., Stanford S. A., Eisenhardt P. R., Lidman C., Holden B., Della Ceca R., Norman C., Squires G., 2001, ApJ, 561, 13

Bower R. G., Benson A. J., Lacey C. G., Baugh C. M., Cole S., Frenk C. S., 2001, MNRAS, 325, 497

Bower R. G., Benson A. J., Malbon R., Helly J. C., Frenk C. S., Baugh C. M., Cole S., Lacey C. G., 2006, MNRAS, 370, 645

Bullock J. S., 2002, in Natarajan P., ed., The shapes of galaxies and their dark halos, Proceedings of the Yale Cosmology Workshop, New Haven, Connecticut, USA, p.109 Shapes of dark matter halos. pp 109–+

Bullock J. S., Dekel A., Kolatt T. S., Kravtsov A. V., Klypin A. A., Porciani C., Primack J. R., 2001, ApJ, 555, 240

Bullock J. S., Kravtsov a. A. V., Colín P., 2002, ApJ, 564, L1

Busha M. T., Evrard A. E., Adams F. C., 2007, ApJ, 665, 1

Carlberg R. G., Yee H. K. C., Ellingson E., Abraham R., Gravel P., Morris S., Pritchet C. J., 1996, ApJ, 462, 32

Carroll S. M., Press W. H., Turner E. L., 1992, ARA&A, 30, 499

Cen R., Miralda-Escudé J., Ostriker J. P., Rauch M., 1994, ApJ, 437, L9

Centrella J., Melott A. L., 1983, Nature, 305, 196

Centrella J. M., Gallagher III J. S., Melott A. L., Bushouse H. A., 1988, ApJ, 333, 24

Chen D. N., Jing Y. P., 2002, MNRAS, 336, 55

Ciardi B., Ferrara A., White S. D. M., 2003, MNRAS, 344, L7

Cole S., Aragon-Salamanca A., Frenk C. S., Navarro J. F., Zepf S. E., 1994, MNRAS, 271, 781

Cole S., Helly J., Frenk C. S., Parkinson H., 2008, MNRAS, 383, 546

Cole S., Kaiser N., 1989, MNRAS, 237, 1127

Cole S., Lacey C., 1996, MNRAS, 281, 716

Cole S., Lacey C. G., Baugh C. M., Frenk C. S., 2000, MNRAS, 319, 168

Cole S., Norberg P., Baugh C. M., Frenk C. S., Bland-Hawthorn J., Bridges T., Cannon R., Colless M., et al. 2001, MNRAS, 326, 255

Colín P., Avila-Reese V., Valenzuela O., 2000, ApJ, 542, 622

Colless M., Dalton G., Maddox S., Sutherland W., Norberg P., Cole S., Bland-Hawthorn J., Bridges T., et. al 2001, MNRAS, 328, 1039

Conroy C., Wechsler R. H., Kravtsov A. V., 2007, ApJ, 668, 826

Couchman H. M. P., Rees M. J., 1986, MNRAS, 221, 53

Croton D. J., et. al 2006, MNRAS, 365, 11

Davis M., Efstathiou G., Frenk C. S., White S. D. M., 1985, ApJ, 292, 371

Davis M., Peebles P. J. E., 1983, ApJ, 267, 465

de Bernardis P., Ade P. A. R., Bock J. J., Bond J. R., Borrill J., Boscaleri A., Coble K., Contaldi C. R., et al. 2002, ApJ, 564, 559

de Bernardis P., Ade P. A. R., Bock J. J., Bond J. R., Borrill J., Boscaleri A., Coble K., Crill B. P., et al. 2000, Nature, 404, 955

De Lucia G., Blaizot J., 2007, MNRAS, 375, 2

De Lucia G., Kauffmann G., Springel V., White S. D. M., Lanzoni B., Stoehr F., Tormen G., Yoshida N., 2004, MNRAS, 348, 333

De Lucia G., Kauffmann G., White S. D. M., 2004, MNRAS, 349, 1101

De Lucia G., Springel V., White S. D. M., Croton D., Kauffmann G., 2006, MNRAS, 366, 499

Dekel A., Devor J., Hetzroni G., 2003, MNRAS, 341, 326

Diemand J., Moore B., Stadel J., 2004, MNRAS, 353, 624

D'Onghia E., Navarro J. F., 2007, MNRAS, 380, L58

Doroshkevich A. G., 1970, Astrophysics, 6, 320

Drory N., Salvato M., Gabasch A., Bender R., Hopp U., Feulner G., Pannella M., 2005, ApJ, 619, L131

Dubinski J., Carlberg R. G., 1991, ApJ, 378, 496

Efstathiou G., Bond J. R., 1986, MNRAS, 218, 103

Efstathiou G., Davis M., White S. D. M., Frenk C. S., 1985, ApJS, 57, 241

Eke V. R., Navarro J. F., Steinmetz M., 2001, ApJ, 554, 114

Feulner G., Bender R., Drory N., Hopp U., Snigula J., Hill G. J., 2003, MNRAS, 342, 605

Fillmore J. A., Goldreich P., 1984, ApJ, 281, 1

Fontana A., Salimbeni S., Grazian A., Giallongo E., Pentericci L., Nonino M., Fontanot F., Menci N., Monaco P., Cristiani S., Vanzella E., de Santis C., Gallozzi S., 2006, A&A, 459, 745

Frenk C. S., White S. D. M., Davis M., 1984, in Setti G., Van Hove L., eds, Large-Scale Structure of the Universe Elementary Particles and the Large-Scale Structure of the Universe - Short Contributions. pp 257–+

Gao L., Loeb A., Peebles P. J. E., White S. D. M., Jenkins A., 2004, ApJ, 614, 17

Gao L., Navarro J. F., Cole S., Frenk C., White S. D. M., Springel V., Jenkins A., Neto A. F., 2007, ArXiv e-prints, 711

Gao L., Springel V., White S. D. M., 2005, MNRAS, 363, L66

Gao L., White S. D. M., Jenkins A., Stoehr F., Springel V., 2004, MNRAS, 355, 819

Gao L., Yoshida N., Abel T., Frenk C. S., Jenkins A., Springel V., 2007, MNRAS, 378, 449

Ghigna S., Moore B., Governato F., Lake G., Quinn T., Stadel J., 2000, ApJ, 544, 616

Giovanelli R., Haynes M. P., da Costa L. N., Freudling W., Salzer J. J., Wegner G., 1997, ApJ, 477, L1+

Gnedin N. Y., 2000, ApJ, 535, 530

Gonzalez A. H., Zabludoff A. I., Zaritsky D., 2005, ApJ, 618, 195

Götz M., Sommer-Larsen J., 2002, Ap&SS, 281, 415

Götz M., Sommer-Larsen J., 2003, Ap&SS, 284, 341

Graham A. W., Merritt D., Moore B., Diemand J., Terzić B., 2006, AJ, 132, 2701

Hansen S. H., Agertz O., Joyce M., Stadel J., Moore B., Potter D., 2007, ApJ, 656, 631

Hawkins E., Maddox S., Cole S., Lahav O., Madgwick D. S., Norberg P., Peacock J. A., Baldry e., 2003, MNRAS, 346, 78

Hayashi E., White S. D. M., 2007, ArXiv e-prints, 709

Hoekstra H., Mellier Y., van Waerbeke L., Semboloni E., Fu L., Hudson M. J., Parker L. C., Tereno I., Benabed K., 2006, ApJ, 647, 116

Hoyle F., 1949, MNRAS, 109, 365

Huang J.-S., Glazebrook K., Cowie L. L., Tinney C., 2003, ApJ, 584, 203

Huss A., Jain B., Steinmetz M., 1999a, ApJ, 517, 64

Huss A., Jain B., Steinmetz M., 1999b, MNRAS, 308, 1011

Iliev I. T., Mellema G., Pen U.-L., Bond J. R., Shapiro P. R., 2007, ArXiv Astrophysics e-prints

Jing Y. P., Börner G., 2004, ApJ, 617, 782

Jing Y. P., Mo H. J., Boerner G., 1998, ApJ, 494, 1

Kaiser N., 1984, ApJ, 284, L9

Kasun S. F., Evrard A. E., 2005, ApJ, 629, 781

Kauffmann G., 1996, MNRAS, 281, 475

Kauffmann G., Colberg J. M., Diaferio A., White S. D. M., 1999a, MNRAS, 303, 188

Kauffmann G., Colberg J. M., Diaferio A., White S. D. M., 1999b, MNRAS, 307, 529

Kauffmann G., Haehnelt M., 2000, MNRAS, 311, 576

Kauffmann G., White S. D. M., 1993, MNRAS, 261, 921

Kauffmann G., White S. D. M., Guiderdoni B., 1993, MNRAS, 264, 201

Kazantzidis S., Mayer L., Mastropietro C., Diemand J., Stadel J., Moore B., 2004, ApJ, 608, 663

Kennicutt Jr. R. C., 1998, ApJ, 498, 541

Kitzbichler M. G., White S. D. M., 2007, MNRAS, 376, 2

Knebe A., Devriendt J. E. G., Gibson B. K., Silk J., 2003, MNRAS, 345, 1285

Knebe A., Devriendt J. E. G., Mahmood A., Silk J., 2002, MNRAS, 329, 813

Knebe A., Green A., Binney J., 2001, MNRAS, 325, 845

Kolb E. W., Turner M. S., 1990, The early universe. Frontiers in Physics, Reading, MA: Addison-Wesley, 1988, 1990

Kravtsov A. V., Klypin A. A., Khokhlov A. M., 1997, ApJS, 111, 73

Lewis A., Challinor A., Lasenby A., 2000, ApJ, 538, 473

Lewis A., Weller J., Battye R., 2006, MNRAS, 373, 561

Li C., Jing Y. P., Kauffmann G., Börner G., Kang X., Wang L., 2007, MNRAS, 376, 984

Li C., Kauffmann G., Jing Y. P., White S. D. M., Börner G., Cheng F. Z., 2006, MNRAS, 368, 21

Li G. L., Mao S., Jing Y. P., Mo H. J., Gao L., Lin W. P., 2006, MNRAS, 372, L73

Lynden-Bell D., 1967, MNRAS, 136, 101

Macciò A. V., Dutton A. A., van den Bosch F. C., Moore B., Potter D., Stadel J., 2007, MNRAS, 378, 55

MacMillan J. D., Widrow L. M., Henriksen R. N., 2006, ApJ, 653, 43

Martel H., 1991, ApJ, 366, 353

Martin C. L., 1999, ApJ, 513, 156

Massey R., Rhodes J., Leauthaud A., Capak P., Ellis R., Koekemoer A., Refregier A., Scoville N., et al. 2007, ApJS, 172, 239

Mather J. C., Cheng E. S., Eplee Jr. R. E., Isaacman R. B., Meyer S. S., Shafer R. A., Weiss R., Wright E. L., et al. 1990, ApJ, 354, L37

Merritt D., Graham A. W., Moore B., Diemand J., Terzić B., 2006, AJ, 132, 2685

Mo H. J., Jing Y. P., Borner G., 1993, MNRAS, 264, 825

Mo H. J., Mao S., White S. D. M., 1998, MNRAS, 295, 319

Mo H. J., White S. D. M., 1996, MNRAS, 282, 347

Mo H. J., White S. D. M., 2002, MNRAS, 336, 112

Moore B., Quinn T., Governato F., Stadel J., Lake G., 1999, MNRAS, 310, 1147

Naab T., Johansson P. H., Ostriker J. P., Efstathiou G., 2007, ApJ, 658, 710

Natarajan P., Croton D., Bertone G., 2007, ArXiv e-prints, 711

Navarro J. F., Frenk C. S., White S. D. M., 1994, MNRAS, 267, L1+

Navarro J. F., Frenk C. S., White S. D. M., 1996, ApJ, 462, 563

Navarro J. F., Frenk C. S., White S. D. M., 1997, ApJ, 490, 493

Neto A. F., Gao L., Bett P., Cole S., Navarro J. F., Frenk C. S., White S. D. M., Springel V., Jenkins A., 2007, MNRAS, 381, 1450

Norman M. L., Bryan G. L., 1999, in Miyama S. M., Tomisaka K., Hanawa T., eds, Numerical Astrophysics Vol. 240 of Astrophysics and Space Science Library, Cosmological Adaptive Mesh Refinement. pp 19–+

Parkinson H., Cole S., Helly J., 2008, MNRAS, 383, 557

Peebles P. J. E., 1969, ApJ, 155, 393

Peebles P. J. E., 1980, The large-scale structure of the universe. Princeton, N.J., Princeton University Press, 1980. 435 p.

Peebles P. J. E., 1982, ApJ, 263, L1

Penzias A. A., Wilson R. W., 1965, ApJ, 142, 419

Popa L. A., 2006, ArXiv Astrophysics e-prints

Porciani C., Dekel A., Hoffman Y., 2002, MNRAS, 332, 325

Power C., Navarro J. F., Jenkins A., Frenk C. S., White S. D. M., Springel V., Stadel J., Quinn T., 2003, MNRAS, 338, 14

Pozzetti L., Cimatti A., Zamorani G., Daddi E., Menci N., Fontana A., Renzini A., Mignoli M., et. al 2003, A&A, 402, 837

Press W. H., Schechter P., 1974, ApJ, 187, 425

Raig A., González-Casado G., Salvador-Solé E., 1998, ApJ, 508, L129

Reed D. S., Bower R., Frenk C. S., Jenkins A., Theuns T., 2007, MNRAS, 374, 2

Rees M. J., Ostriker J. P., 1977, MNRAS, 179, 541

Rodrigues D. D. C., Thomas P. A., 1996, MNRAS, 282, 631

Salvador-Sole E., Solanes J. M., Manrique A., 1998, ApJ, 499, 542

Saracco P., Fiano A., Chincarini G., Vanzella E., Longhetti M., Cristiani S., Fontana A., Giallongo E., Nonino M., 2006, MNRAS, 367, 349

Schmidt M., 1959, ApJ, 129, 243

Schombert J. M., 1988, ApJ, 328, 475

Schuecker P., Böhringer H., Collins C. A., Guzzo L., 2003, A&A, 398, 867

Seljak U., Zaldarriaga M., 1996, ApJ, 469, 437

Sheth R. K., Mo H. J., Tormen G., 2001, MNRAS, 323, 1

Smoot G., Bennett C., Weber R., Maruschak J., Ratliff R., Janssen M., Chitwood J., Hilliard L., et al. 1990, ApJ, 360, 685

Somerville R. S., Kolatt T. S., 1999, MNRAS, 305, 1

Somerville R. S., Primack J. R., 1999, MNRAS, 310, 1087

Spergel D. N., Bean R., Doré O., Nolta M. R., Bennett C. L., Dunkley J., Hinshaw G., Jarosik N., et al. 2007, ApJS, 170, 377

Spergel D. N., Verde L., Peiris H. V., Komatsu E., Nolta M. R., Bennett C. L., Halpern M., Hinshaw G., et. al 2003, ApJS, 148, 175

Springel V., 2005, MNRAS, 364, 1105

Springel V., Hernquist L., 2003, MNRAS, 339, 312

Springel V., White S. D. M., Jenkins A., Frenk C. S., Yoshida N., Gao L., Navarro J., Thacker R., Croton D., Helly J., Peacock J. A., Cole S., Thomas P., Couchman H., Evrard A., Colberg J., Pearce F., 2005, Nature, 435, 629

Springel V., White S. D. M., Tormen G., Kauffmann G., 2001, MNRAS, 328, 726

Springel V., Yoshida N., White S. D. M., 2001, New Astronomy, 6, 79

Stoehr F., White S. D. M., Tormen G., Springel V., 2002, MNRAS, 335, L84

Subramanian K., Cen R., Ostriker J. P., 2000, ApJ, 538, 528

Syer D., White S. D. M., 1998, MNRAS, 293, 337

Taylor J. E., Navarro J. F., 2001, ApJ, 563, 483

Tinker J. L., Weinberg D. H., Zheng Z., 2006, MNRAS, 368, 85

Tinker J. L., Weinberg D. H., Zheng Z., Zehavi I., 2005, ApJ, 631, 41

van den Bosch F. C., Abel T., Croft R. A. C., Hernquist L., White S. D. M., 2002, ApJ, 576, 21

van den Bosch F. C., Mo H. J., Yang X., 2003, MNRAS, 345, 923

van den Bosch F. C., Yang X., Mo H. J., Weinmann S. M., Macciò A. V., More S., Cacciato M., Skibba R., Kang X., 2007, MNRAS, 376, 841

Viel M., Lesgourgues J., Haehnelt M. G., Matarrese S., Riotto A., 2006, Physical Review Letters, 97, 071301

Villumsen J. V., 1989, ApJS, 71, 407

Vitvitska M., Klypin A. A., Kravtsov A. V., Wechsler R. H., Primack J. R., Bullock J. S., 2002, ApJ, 581, 799

Wang J., De Lucia G., Kitzbichler M. G., White S. D. M., 2008, MNRAS, 384, 1301

Wang J., White S. D. M., 2007, MNRAS, 380, 93

Wang L., Li C., Kauffmann G., De Lucia G., 2006, MNRAS, 371, 537

Warren M. S., Quinn P. J., Salmon J. K., Zurek W. H., 1992, ApJ, 399, 405

Wechsler R. H., Bullock J. S., Primack J. R., Kravtsov A. V., Dekel A., 2002, ApJ, 568, 52

Weinmann S. M., van den Bosch F. C., Yang X., Mo H. J., Croton D. J., Moore B., 2006, MNRAS, 372, 1161

White S. D. M., 1984, ApJ, 286, 38

White S. D. M., 1996, in Schaeffer R., Silk J., Spiro M., Zinn-Justin J., eds, Cosmology and Large Scale Structure Formation and Evolution of Galaxies. pp 349–+

White S. D. M., Efstathiou G., Frenk C. S., 1993, MNRAS, 262, 1023

White S. D. M., Frenk C. S., 1991, ApJ, 379, 52

White S. D. M., Frenk C. S., Davis M., 1983, ApJ, 274, L1

White S. D. M., Frenk C. S., Davis M., Efstathiou G., 1987, ApJ, 313, 505

White S. D. M., Rees M. J., 1978, MNRAS, 183, 341

Xu G., 1995, ApJS, 98, 355

Yang X., Mo H. J., Jing Y. P., van den Bosch F. C., Chu Y., 2004, MNRAS, 350, 1153

Zel'dovich Y. B., 1970, A&A, 5, 84

Zhao D. H., Mo H. J., Jing Y. P., Börner G., 2003, MNRAS, 339, 12

Zibetti S., White S. D. M., Schneider D. P., Brinkmann J., 2005, MNRAS, 358, 949